TECHNISCHE UNIVERSITÄT MÜNCHEN

Lehrstuhl für Technische Chemie II

Hydrogenation of tetralin over oxide supported Pt and Pt-Pd catalysts

Benjamin Fonfé

Vollständiger Abdruck der von der Fakultät für Chemie der Technischen Universität München zur Erlangung des akademischen Grades eines

Doktors der Naturwissenschaften

genehmigten Dissertation.

Vorsitzender:		Univ.-Prof. Dr. Kai-Olaf Hinrichsen
Prüfer der Dissertation:		
	1.	Univ.-Prof. Dr. Johannes A. Lercher
	2.	Univ.-Prof. Dr. Klaus Köhler

Die Dissertation wurde am 27.08.2008 bei der Technischen Universität München eingereicht und durch die Fakultät für Chemie am 17.11.2008 angenommen.

Acknowledgements

During the last four years working at TC 2 I have met many interesting people from all over the world. Although I cannot acknowledge everyone here in person I would like to thank all of you as every single person has contributed in some way on my climb to the top of the mountain called PhD thesis.

Johannes, thank you for having given me the opportunity to experience science in an ambitious and challenging, but also pleasant environment. I was always pleased to get your opinion on the deeper understanding of catalysis and on the question how to combine data sets to a fascinating story. It was fun to walk with you through Amsterdam discussing about sulfur tolerance and stroopwafels. Moreover I greatly appreciate that you provided me the contacts to Enrique Iglesia and Katia Fajerwerg during my undergraduate studies. Besides Garching, Berkeley and Paris were the most interesting periods of my life. There, I did not only get perfect scientific access to catalysis and an insight into the American and French culture. I also made a lot of friends worldwide, who still play an important role in my life today.

Rob van Veen was the most friendly project partner I could imagine. Thanks for the productive discussions and the generous financial support of Shell R.T.C. Amsterdam.

Florencia, you are a special person for me and I will never forget your Argentinean temper. Thank you for your guidance during the first year. We were a really cool team!

Although the EXAFS trips to Hamburg were very exhausting it was always a special atmosphere at Hasylab and a lot fun to work in the team during day and night. Thank you Andy for introducing me into the topic and helping me in the particle modeling.

Thanks Marianne for showing me the art of taking TEM pictures in focus. Thanks Xaver and Andreas for all your help in building the set-up and solving technical problems whenever it was necessary. Martin, thank you for the BET and AAS measurements.

Many students did a great job and contributed to the present work. I would like to point out especially Yanzhe and Mahdi, who spent a lot of time operating the trickle bed reactor set-up and analyzing the data. Thank you!

Virginia and Ella, thanks for your deep friendship! I could not imagine better office mates and I hope that we will keep close contact in the future even when separated by the Atlantic Ocean.

Finally, I would like to mention my family and friends for invaluable support. Thank you forever for your love and all the things you did for me!

Contents

Chapter 1

General introduction

Chapter 2

Characterization of ASA-supported platinum and platinum-palladium catalysts by ^{27}Al (3Q) MAS NMR, IR, TEM, EXAFS and XANES

Chapter 3

Hydrogenation of tetralin by silica-alumina supported Pt catalysts I -Mechanistic aspects in the presence of sulfur and nitrogen containing poisons

Chapter 4

Hydrogenation of tetralin by amorphous silica-alumina supported Pt and Pt-Pd catalysts II – Influence of the metal alloy formation, support composition and reaction temperature on the sulfur and nitrogen poison tolerance

Chapter 5

Summary

Chapter 1

General introduction

The continuously growing demand of diesel fuel worldwide combined with the need to lower diesel emissions led to the development of advanced diesel engine and aftertreatment technology in the recent decades. The improvement of diesel fuel quality by lowering the concentration of aromatic and sulfur compounds enhances the efficiency of modern motor and pipe exhaust gas cleaning systems and thus strongly decreases diesel exhaust emissions such as particulate matter. Ultra clean diesel fuel meeting the strict requirements of international legislation are produced by catalytic hydrotreating processes in modern refineries. For the hydrogenation of aromatics noble metal catalysts possess excellent activity, but they are unfortunately swiftly poisoned by small amounts of sulfur and nitrogen containing molecules. The current knowledge of aromatics hydrogenation over oxide supported Pt and Pt-Pd catalysts is reviewed, especially addressing the role of acidic carriers and bimetallic alloy formation on the properties of small metal clusters, their catalytic performance and their resistance towards catalyst poisons. At the end of this chapter the milestones of the work in the subsequent chapters are highlighted.

1 Background and motivation

1.1 Growing diesel fuel demand worldwide

Over the last 20 years demand for diesel fuel has been growing faster than gasoline demand worldwide. Especially the nations of the European Union prefer diesel over gasoline, which was initially mainly policy driven, i.e. lower tax rates to promote diesel over gasoline consumption (Figure 1) [1]. Also in the U.S. the importance of diesel fuel is growing, but diesel market penetration in America is still far behind compared to the diesel preference in Europe (Figure 1).

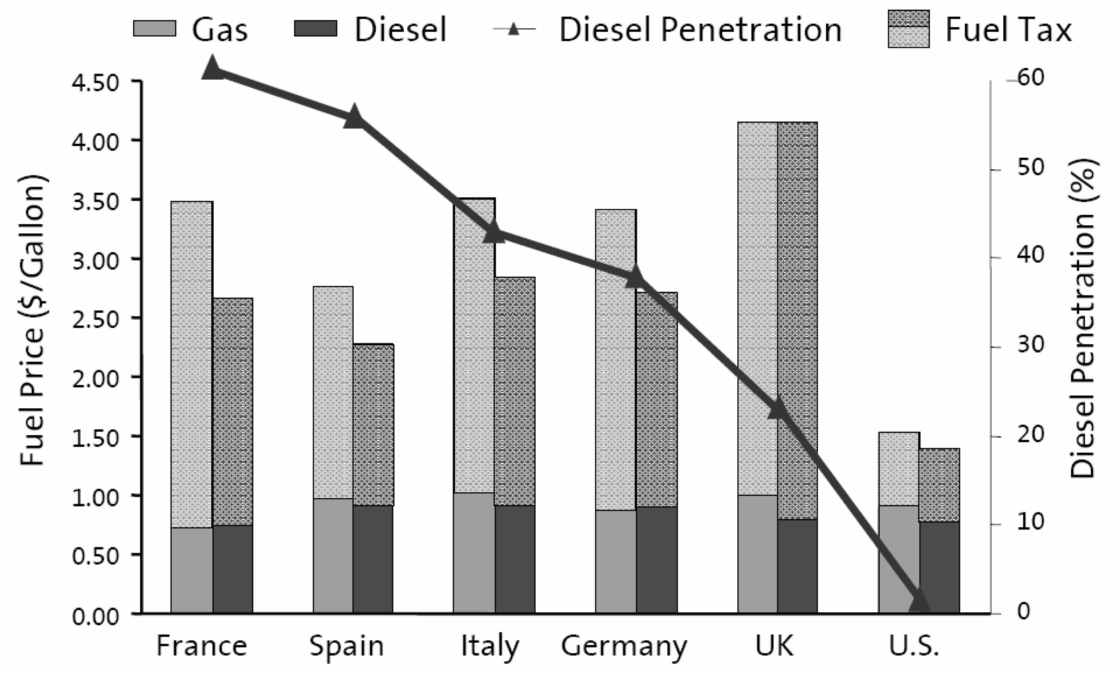

Figure 1. Comparison between the U.S. and Europe: Diesel penetration and Fuel price composition [2].

European consumers have more good reasons choosing diesel powered vehicles. They are taking up advanced diesel technology to get better fuel efficiency, more power and more durability, as well as quiet, clean, premium vehicles that were previously the domain of petrol cars. Over 50 % of new passenger cars in Europe have diesel engines compared to less than 20% 15 years ago. It is likely that consumer preference for power and comfort is now the significant factor that drives the diesel uptake in Europe. In France, Austria and Belgium, well over 60% of new passenger cars, and over 80% of luxury cars, are diesels [3]

More than 140 million tons of diesel fuel was consumed in the European Union in 2007 and is expected to rise to 170 million tons by 2020. In contrary reduced gasoline consumption in Europe could be observed in the recent years and is predicted to further decrease in the future. Thus, since 2002, diesel fuel consumption in Europe is even higher compared to gasoline usage (Figure 2).

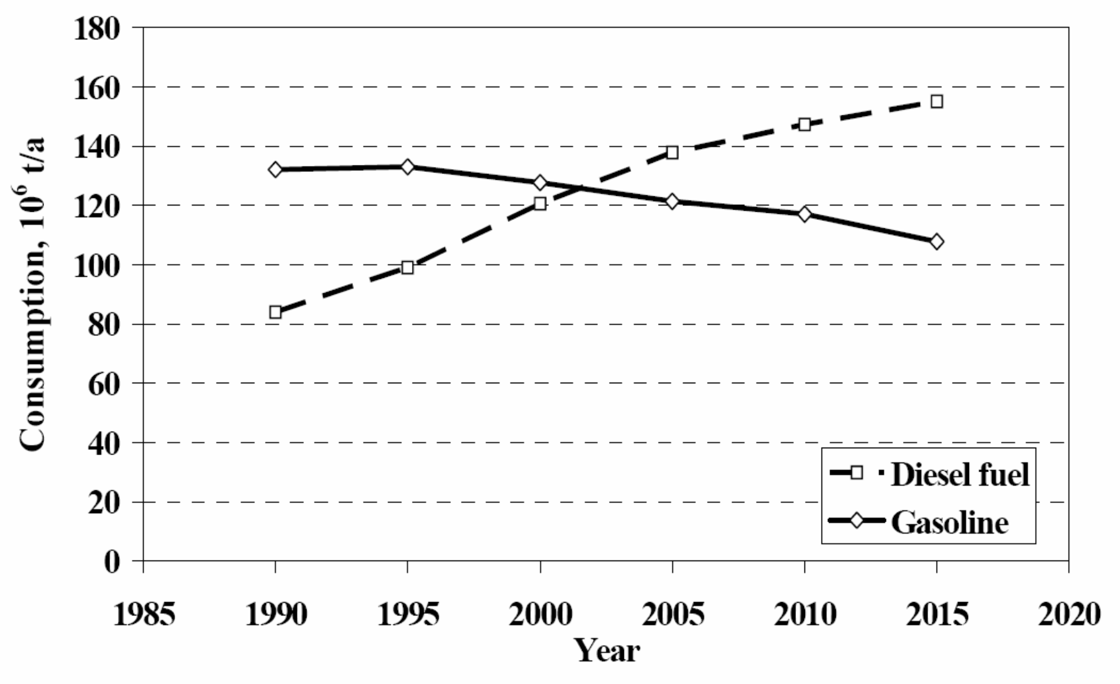

Figure 2. Trends of diesel fuels and gasoline demands in EU [4] [5]

While gasoline may be still the fuel of choice for passenger cars in the U.S., diesel distillates power jet airplanes, trucks and railway locomotives. Therefore, diesel demand in America is actually also growing more rapidly than the demand for gasoline [6].

Furthermore, developing countries with a strong economic growth like China and India contribute to the growing diesel fuel demand to a large extent. Entering the global markets over the last 10 to 15 years much more freight is being moved around the world, very often by diesel powered trucks or trains. Increasing level of demand is not only caused by the growing consumption of diesel fuels used for transportation purpose. Unreliable electricity grids in these nations force the use of backup power supply by diesel generators [7].

Gasoil as a feedstock for steam cracking is a further spreading application, which is primarily the result of the growing demand on light olefins. The world's steam cracking capacity is going to increase being the most cost-effective technology for the production of light olefins [8]. In several regions like the European Union where the availability of light hydrocarbons is limited, the required amount of light olefins can be produced not only from naphtha but also through the pyrolysis of heavier hydrocarbon fractions like kerosene and gasoils.

1.2 Pollution caused by diesel engines and their effects

Rudolph Diesel (1858-1913) filed the first patent for the 'economical heat motor' in 1892. Diesel engines are the power source of choice when it comes to heavy-duty trucks, buses, trains, large ships, power generators, engines for non-road equipment such as excavators, cranes and agricultural equipment. It is advantageous that diesel engines require less maintenance and generate energy more efficiently and with less carbon dioxide emissions than equivalent ignition-based gasoline engines. Whereas the gaseous hydrocarbons (HC) and CO emissions of diesel engines are in the same order as those of gasoline engines, the relatively high emissions of particulate matter (PM) and nitrogen oxides (NO_X) is a major drawback of diesel engines.

PM is a mixture of solid particles and liquid droplets in the air consisting of carbon, inorganic oxides and hydrocarbons, including some highly toxic polyaromatic hydrocarbons. Particulate matter emissions are mainly the result of the heterogeneous nature of incomplete diesel combustion. These high temperature cracking reactions (pyrolysis) lead to the formation of carbonaceous soot particles. Unburned or partially burned fuel can condense on these particles, increasing their size and mass. Size and composition are influenced in detail by the motor, fuel, additives, as well as the history during motion in the exhaust pipe. These particles can agglomerate and create visible smoke [9].

A model of diluted and cooled diesel PM consisting of two types of particles is presented in Figure 3: (a) fractal-like agglomerates of primary particles 15–30 nm in diameter, composed of carbon and traces of metallic ash, and coated with condensed heavier end organic compounds and sulfate; (b) nucleation particles composed of condensed hydrocarbons and sulfate. [10]

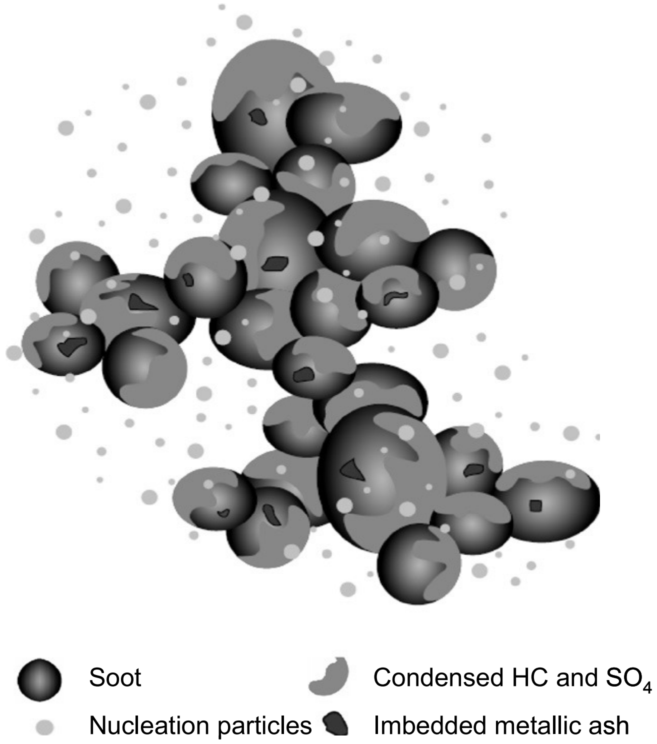

Figure 3. Model of diesel particulate matter [10].

Due to its small size, fine particulate matter can be deposited deep in the lungs where it can cause health problems. Studies have shown an association between particulate matter and premature mortality from respiratory and cardiovascular disease and increased incidence of respiratory illness particularly in children and the elderly. For adults with heart or lung conditions, exposure to fine particulate matter can cause more illness and in some cases premature death. More than 90% of the particulates found in diesel exhaust are fine particles [11].

Nitrogen oxides contribute to the formation of ground level ozone. Health effects include respiratory problems such as coughing, shortness of breath, and decreased lung function [11]. While other ozone precursors (volatile organic compounds and carbon monoxide) have decreased over the past 20 years, emissions of NOx, including those from on-road vehicles, have increased. [12].

1.3 Reduction of diesel engine emissions

Since 2008 the Euro 5 emission standard of passenger cars powered by diesel engines is effective in the European Union (Table 1.) [13].

Table 1. Emission standard of passenger cars powered by diesel engines (EU)

Emission standard	Year	Emission (g/kg)			
		HC + NO_X	NO_X	CO	PM
Euro 1	1992	0.97	-	2.72	0.140
Euro 2 - IDI	1996	0.70	-	1.00	0.080
Euro 2 - DI	1999	0.90	-	1.00	0.100
Euro 3	2000	0.56	0.50	0.64	0.050
Euro 4	2005	0.30	0.25	0.50	0.025
Euro 5	2008	0.25	0.20	0.50	0.005

To meet this strict regulation there are generally three possible basic solutions: (a) enhancement of the diesel motor technology, (b) diesel exhaust aftertreatment and (c) improvement of the diesel fuel quality.

Diesel PM can be reduced by better combustion (higher temperatures and excess of oxygen) in the motor, but then NO_X are raised (so-called PM-NO_X tradeoff). Diesel engine modifications like higher injection pressures, turbo-charging and combustion chamber optimization are highly productive to reduce emissions, especially to decrease PM production [14]. Nevertheless, in order to meet the legislations for both, PM and NO_X emissions, efficient pipe exhaust cleaning is essential.

A modern diesel exhaust aftertreatment system consists of three sections. The first function consists of an oxidation catalytic converter, which reduces carbon monoxide and gaseous hydrocarbons in diesel exhaust. It also affects particulate mass emissions by reducing the organic fraction of the particles. The influence mechanism of an oxidation catalyst on the particle-bound organics is poorly understood, but direct interaction between the particles and catalyst is considered to be unlikely. Instead, the catalyst is assumed to reduce the amount of organics in the gas phase at the catalyst temperature, which results in smaller mass transfer onto the particles when the exhaust cools [15, 16].

The application of a diesel particulate filter (DPF) to remove particulates is the next function in a diesel exhaust cleaning system. Long year's development of DPF has shown that ceramic materials are well-suited candidates to fulfill the harsh requirements of exhaust after treatment. The introduction of DPF in passenger cars in Europe in 2000 was a real breakthrough from a scientific and a commercial point of view. Different systems and filter materials can be used as DPF; however, at the moment silicon carbide wall flow filters seem to be at advantage. There is a continual demand for cost-effective and reliable materials and systems forced by increasing legal emission standards [9].

The strict exhaust emission standards also require highly-efficient NO_X aftertreatment systems in addition to the DPF technology and the oxidation catalyst in the third section of the diesel exhaust cleaning. Primarily, NO_X Adsorber Catalyst (NAC) and Selective Catalytic Reduction (SCR) technology can fulfill the demands for the required NO_X reduction efficiencies that are required for most applications. SCR technology, well known for power plants, was introduced in series for application in commercial vehicles in Europe in 2005 on to comply with the emission standards EURO 4 (2005) and EURO 5 (2008) [9].

The third principle option to reduce diesel engine emissions is the enhancement of the diesel fuel properties. In the next paragraph the possible effects on emissions of individual diesel fuel compounds and properties will be addressed followed by the resulting legislations for automotive diesel fuel composition.

1.4 Diesel fuel properties and their effect on emissions

Diesel fuel is a complex mixture of hydrocarbons composed primarily of paraffin and aromatics, with olefin contents amounting to only a few percent by volume. Although a large number of studies of the impact of diesel on emissions have been performed, it has been difficult to identify which fuel properties can be manipulated to reduce emissions because different engines of the same or similar design can and have been observed to react differently to specific changes in fuel properties. Another factor is that, in many studies, individual fuel properties are frequently correlated with other fuel properties, thus, making it difficult to determine whether it is one fuel property or another or some combination of both, that is important with respect to diesel engine emissions.

1.4.1 Physical properties

Diesel engine emissions are known to be affected by the diesel fuel volatility, density and viscosity.

Diesel volatility influences particulate matter emissions, which is probably caused to a large extent by differences in the sulfur and aromatics contents. In general, relatively high boiling points are considered to be associated with higher PM and lower hydrocarbon emissions [17, 18].

Regarding the emission problems diesel fuel density is considered to be a more important fuel property regarding the emission problems. Fewer emissions are produced when engines are running on light diesel fuel [19]. Variations in fuel density (and viscosity) result in variations in engine power and, consequently, in engine emissions and fuel consumption. As viscosity is affected by ambient temperature, it is important to minimize the range between minimum and maximum viscosity limits to allow optimum engine performance. [20].

The density of diesel fuel can be correlated with its aromatic content, the higher the density, the higher the amount of aromatic compounds in the fuel [21]. Therefore, the aromatics concentration can explain density values and is, thus, actually the more important fuel property.

1.4.2 Cetane number

In the domain of diesel engines the cetane number (CN) is the prime indicator of diesel fuel quality and is a measurement of the combustion quality of diesel fuel during compression ignition. Most diesel engines run well with a CN of 40-55. Fuels with higher cetane number which have shorter ignition delays provide more time for the fuel combustion process to be completed. Hence, higher speed diesels operate more effectively with higher cetane number fuels. CN is conceptionally similar to the octane number used for gasoline. Generally, a compound that has high octane number tends to have a low CN and vice versa.

The cetane number of 100 was assigned to the long straight-chain hydrocarbon, hexadecane (trivial name cetane), while alpha-methyl napthalene was assigned a cetane number of 0. All other hydrocarbons in diesel fuel are indexed to cetane as to how well they ignite under compression. The two reference compounds show that CN decreases with decreasing chain length and increasing branching. Aromatic compounds that are present in significant fractions in conventional diesel fuel have comparably low cetane numbers, but increasing sizes of n-alkyl side chains lead to an increase of CNs [22, 23].

Gaseous emissions such as NO_X, HC and CO and particulate emissions of diesel engines can be reduced by increasing the CN [18, 21]. Figure 4 shows a correlation between PM emissions and cetane number.

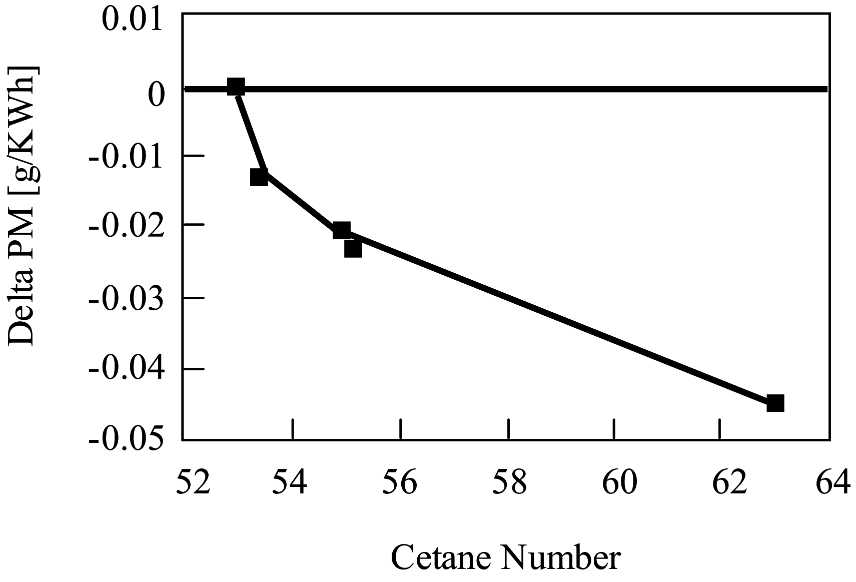

Figure 4. Particulate matter emissions decrease with higher cetane numbers [24].

1.4.3 Sulfur compounds

Diesel fuel sulfur contributes significantly to PM emissions through the formation of sulfates, both in the exhaust stream and later in the atmosphere. Lowering the sulfur content in the fuel lowers the SO_X fraction of PM thus lowering the overall mass of PM emitted [25].

Sulfur can also lead to corrosion and wear of engine systems. Furthermore the efficiency of some exhaust aftertreatment systems is reduced as fuel sulfur content increases, while others are rendered permanently ineffective through sulfur poisoning. Therefore, lower sulfur levels will allow the use of advanced technology in new vehicles in addition to decreased emissions from existing vehicles [26].

1.4.4 Aromatic compounds

Aromatic hydrocarbons contain one or more "benzene-like" ring structures. Compared to paraffins and naphtenes in diesel fuel, aromatic hydrocarbons are denser, have poorer self-ignition qualities and produce more soot in burning. Figure 5 shows that in general high aromatics content results in low cetane numbers.

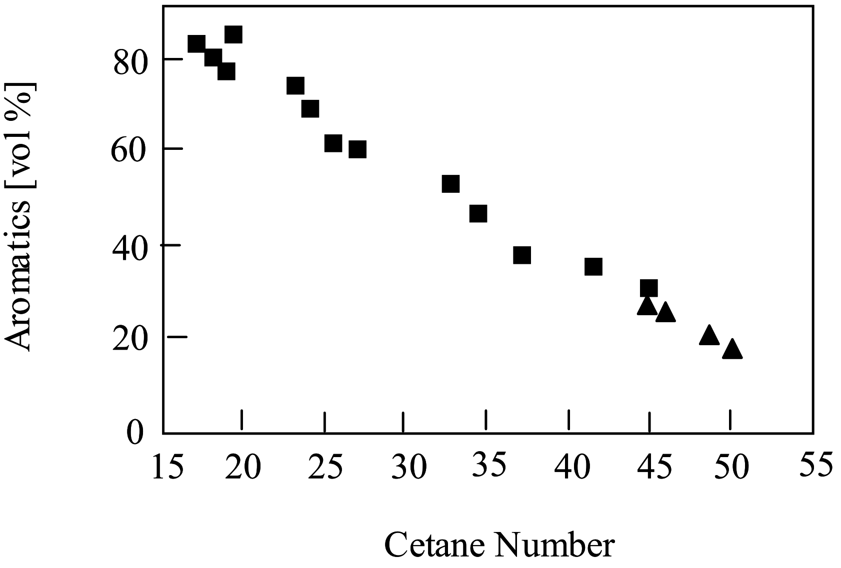

Figure 5. Cetane number vs. aromatic content: (■) Light cycle oil (LCO) and straight run (SR) distillate; (▲) Diesel fuel [27].

This produces more difficulty in cold starting and increased combustion noise, resulting in HC and NO_X emissions that are produced due to the increased ignition delay. Aromatics content was also reported to be an important fuel property affecting PM production [25]. Especially polycyclic aromatic hydrocarbons (PAH) are included in the great number of compounds present in the group of unregulated pollutants emitted from vehicles [28]. Catalytic cracking of residual oil to increase gasoline and diesel production results in increased aromatic contents. A typical straight run diesel might contain 20 to 25% aromatics by volume, while a diesel blended from catalytically cracked stocks could have 40-50% aromatics. Typical cetane values for straight run (SR) diesel are in the range of 50-55; those for highly aromatic diesel fuels are typically 40 to 45, and may be even lower. Ordinarily, straight run diesel fuel produced by simple distillation of crude oil is fairly low in aromatic hydrocarbons.

1.5 Legislation for diesel fuel composition

In the previous sections it was demonstrated how diesel fuel components and properties influence diesel engine exhaust emissions.

Therefore, mandatory environmental fuel specifications are introduced by EU Directives. The following legislations are the most important steps in the evolution of EU diesel fuel specifications [20, 29]:

In 1994 a maximum sulfur level of 2000 ppm was introduced in Europe for all gas oils, including diesel fuel. The minimum cetane number was assigned to 49. The maximum S level in diesel fuel was further decreased in 1996 and 2000 to 500 ppm and 350 ppm, respectively. Furthermore, in the year 2000 the maximum polyaromatics level of 11 % and a minimum cetane number of 51 started to become effective. Since 2005 the maximum diesel fuel sulfur level in the EU is 50 ppm and even 10 ppm sulfur diesel fuel must be available for highway vehicles. 2009 will be the starting year for “sulfur-free” (10 ppm) diesel for highway and nonroad vehicles with a polyaromatics content of 8 % and a maximum density of 840 kg/m^3.

In the US the “Clean Diesel Act of 2003” [30] established standards for motor vehicle diesel fuel produced or imported by any refiner or importer beginning on January 1, 2011. This legislation will require a sulfur content of 10 ppm at the pump (15 ppm since 2006 [31]), a minimum cetane number of 55 and a maximum aromatics content of 15 %.

2 Ultra clean diesel fuel production by catalytic hydrotreating

The recent environmental legislations of diesel fuels focus on sulfur content, aromatic content (mainly polynuclear aromatics) and cetane number. Tightening fuel requirements and higher demand prompted the petroleum companies to proceed with research and development, mainly in the field of heterogeneous catalytic hydrodesulfurization (HDS), hydrodenitrogenation (HDN) and hydrodearomatization (HDA) [32]. In the following paragraphs these catalyting hydrotreating reactions and their common industrial process solutions will be introduced.

2.1 Hydrodesulfurization (HDS)

HDS is a major refining process in order to minimize the sulfur content of naphta reformer feedstock and also from heavier fractions such as gasoil. Commonly commercially used HDS catalysts are MoS_2 or WS_2 promoted with nickel or cobalt. These metal phases are generally supported on large surface oxides as for example γ-alumina. The sulfurized catalysts are stable under typical operation conditions, meaning temperatures of 250-430°C and H_2 partial pressures in the order of 0.5-20 MPa [33]. As the stringent diesel fuel legislations worldwide require the removal of the least reactive organosulfur compounds, research in HDS has been directed at the chemistry of thiophenic compounds, because these are the least reactive organosulfur compounds in fossil fuels [34]. At industrial reaction conditions HDS of organosulfur compounds is exothermic and basically irreversible. In a classical HDS process only the more reactive sulfur molecules are desulfurized (thiols > sulfides > disulfides > thiophenes > benzothiophenes). The most refractory molecules among the sulfur containing compounds in diesel fuel are in general dibenzothiophene (DBT) and especially its alkylated derivates 4-methylbenzothiophene (4-MDBT) and 4,6-dimethybenzothiophene (4,6-DMDBT) [35]. The alkyl groups around the sulfur atom lead to a sterically hindered cleavage of the C-S bonds. In order to reach 10 ppm S in diesel fuel 2009 as demanded by the EU directives also those compounds need to be desulfurized.

DBT is widely used as a model compound for testing the activity and selectivity of HDS catalysts. The 2-pathway reaction mechanism proposed by Houalla et al. [36] is shown in Figure 6.

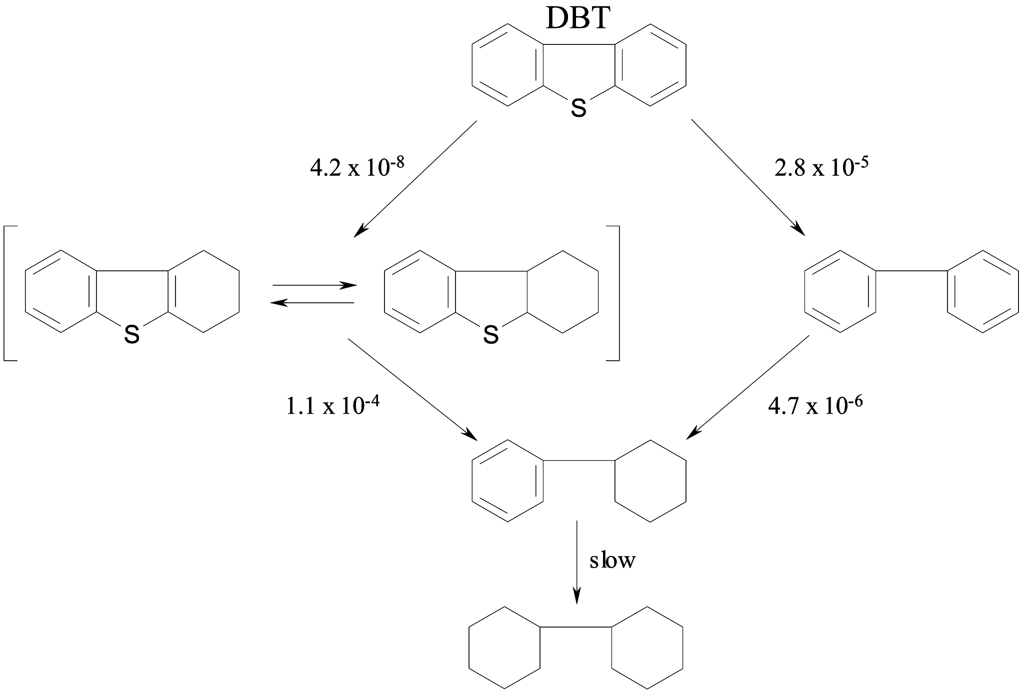

Figure 6. Reaction mechanism of DBT hydrodesulfurization with pseudo-first-order rate constants in L/(g of catalyst s) at 573K [36].

The two parallel reaction pathways for the transformation of DBT are the direct desulfurization pathway (DDS) and the hydrogenation pathway (HYD). DDS forms directly biphenyl (BiP) that is slowly hydrogenated to cyclohexylbenzene (CHB). Following the DDS pathway, DBT is hydrogenated first to 1,2,3,4-tetrahydrodibenzothiophene (THDBT) or to 1,2,3,4,10,11-hexahydrodibenzothiophene (HHDBT) that are subsequently desulfurized to CHB. Under certain operation conditions cyclohexylbenzene can be hydrogenated to dicyclohexane (DCH), but this reaction is very slow compared to the other reaction steps [37].

2.2 Hydrodenitrogenation (HDN)

A great variety of nitrogen compounds have been identified in liquid fossil fuels. They are responsible for imparting instability and color degradation to final products and for poisoning acidic and metal catalysts in refinery processes.

Nitrogen in diesel feedstocks is present predominantly in heterocyclic aromatic compounds [38]. Nonheterocyclic organonitrogen compounds such as aliphatic amines and nitriles are also present, but in considerably smaller amounts, and they are denitrogenated much more rapidly than the heterocyclic compounds [38]. Consequently, nonheterocyclic organonitrogen compounds are less important for purposes of elucidating the nitrogen-removal chemistry occurring in the hydroprocessing of heavy feeds. Nitrogen heterocyclic compounds are classed as basic and nonbasic. In the latter (e.g., indole and carbazole), the lone-pair electrons on the nitrogen atom are delocalized around the aromatic ring and are unavailable for donation to a Lewis acid [39]. The opposite is true for basic heterocyclic compounds such as quinoline and acridine.

The HDN of heterocyclic nitrogen compounds generally involves the following reactions: (i) hydrogenation of the nitrogen heterorings, (ii) hydrogenation of the aromatic rings, and (iii) C–N bond cleavage [40].

Preferentially Mo or W sulfides promoted by Ni sulfide are utilized as HDN catalysts [41]. Hydrogenation of the heteroring is required to reduce the relatively large energy of the carbon-nitrogen bonds in such rings and thus permit more facile carbon-nitrogen bond scission. The energies of carbon-nitrogen double bonds and single bonds are 147 and 73 kcal/mol, respectively [39]. If the carbon-nitrogen bond energy in a typical heterocyclic compound is close to that of a carbon-nitrogen double bond, a reaction breaking the carbon-nitrogen bond is expected to have high activation energy.

The requirement that ring hydrogenation occurs before nitrogen removal also implies that the position of the equilibrium of the hydrogenation reactions can affect nitrogen-removal rates if the rates of the hydrogenolysis reactions are significantly lower than the rates of hydrogenation. An unfavorable hydrogenation equilibrium would result in low concentrations of hydrogenated nitrogen compounds undergoing hydrogenolysis. HDN rates, at least at low surface coverages of organonitrogen compounds, could thus be lowered. High hydrogen partial pressures can be used to increase the equilibrium concentrations of saturated heteroring compounds to obtain larger HDN rates.

As nitrogen heterocyclic compounds must first be hydrogenated before nitrogen is removed, there are numerous intermediate products that contain nitrogen. Therefore, the conversion of a nitrogen containing compound must be distinguished from its HDN conversion (i.e., leading to hydrocarbon products and ammonia).

The complex reaction network of quinoline is representative for higher molecular weight organonitrogen compounds found in heavier hydroprocessing feeds (Figure 7).

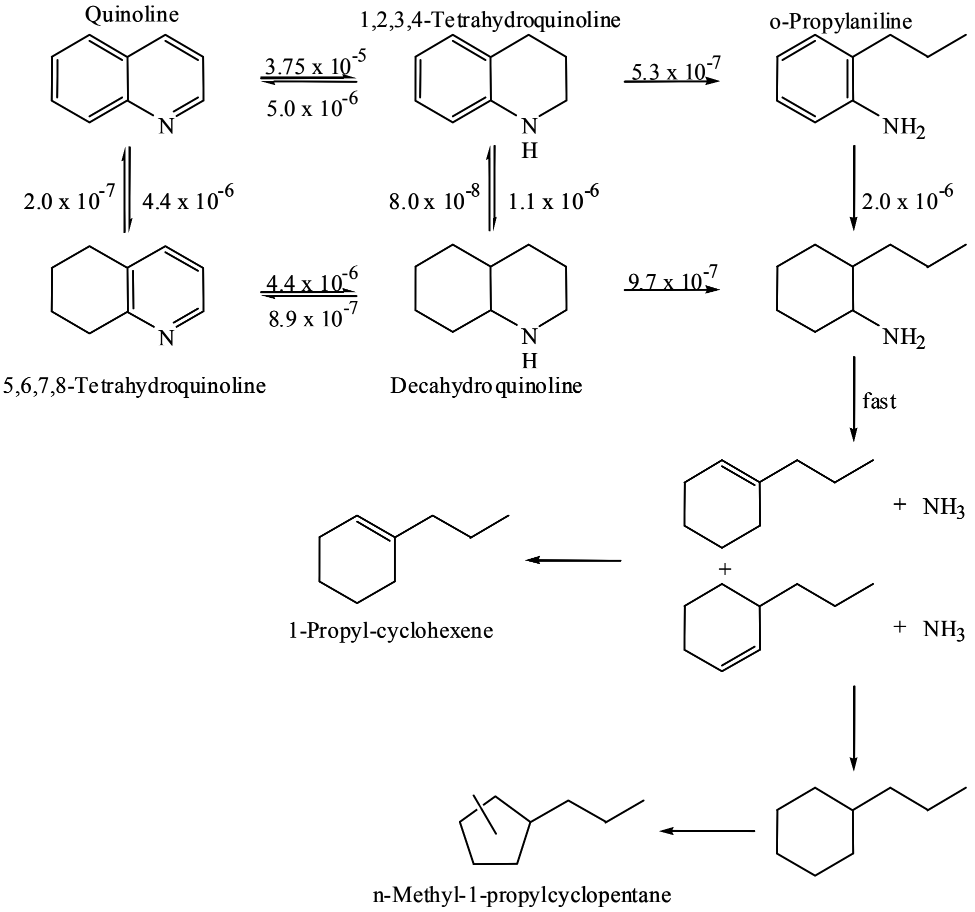

Figure 7. Reaction network for quinoline HDN proposed by Satterfield and Yang [42] including pseudo-rate constants at 648K in mol/(g_{cat}·s).

Quinoline HDN requires the prior hydrogenation of one or both rings. Quinoline hydrogenation to give 1,2,3,4-tetrahydroquinoline is much more rapid than that giving 5,6,7,8-tetrahydroquinoline and approaches equilibrium at lower quinoline conversions. The rapidity of 1,2,3,4-tetrahydroquinoline formation is associated with the higher-electron density of the quinoline heteroring. Hydrogenolysis of 1,2,3,4-tetrahydroquinoline to give o-propylaniline is slower than its hydrogenation to give decahydroquinoline. The slow hydrogenolysis of 1,2,3,4-tetrahydroquinoline could be due to the resonance interaction between the benzenoid ring and the nitrogen-lone-pair electrons. This interaction "ties up" the lone-pair electrons that may be involved in adsorption of 1,2,3,4-tetrahydroquinoline [43]. Most of the nitrogen removal therefore proceeds via decahydroquinoline, with the pathway through 5,6,7,8-tetrahydroquinoline dominating. The path of high hydrogen consumption is thus favored kinetically.

2.3 Hydrodearomatization (HDA)

A number of aromatic model compounds that represent components in industrial feeds have been extensively studied on several catalysts. These include both, unsupported and oxide supported hydrogenation catalysts, using the conventional Co-Mo, Ni-Mo, Ni-W and highly active platinum group metals (including ruthenium, rhodium, palladium and platinum). On all catalysts, the rate of hydrogenation generally increases with the number of aromatic rings present, i.e. a low rate of hydrogenation is observed for monoaromatic rings such as benzene [44]. The greater reactivity for hydrogenation with higher fused ring systems, such as naphthalene and anthracene, is due to the fact that the resonance energy of the second ring of these multiple compounds is less than for benzene [45].

The hydrogenation of aromatics is an exothermic and reversible reaction with heats of reaction ranging in the order between 63 and 71 kJ/mol H_2 [46, 47]. Therefore, high reaction temperatures commonly applied in industrial hydrotreating (> 350° C) forces the equilibrium towards the aromatic compound and complete conversion becomes impossible. The maximum equilibrium conversion occurs at temperatures close to or even below the temperatures needed for the hydrodearomatization rate to be of industrial interest and this is clearly seen in Figure 8.

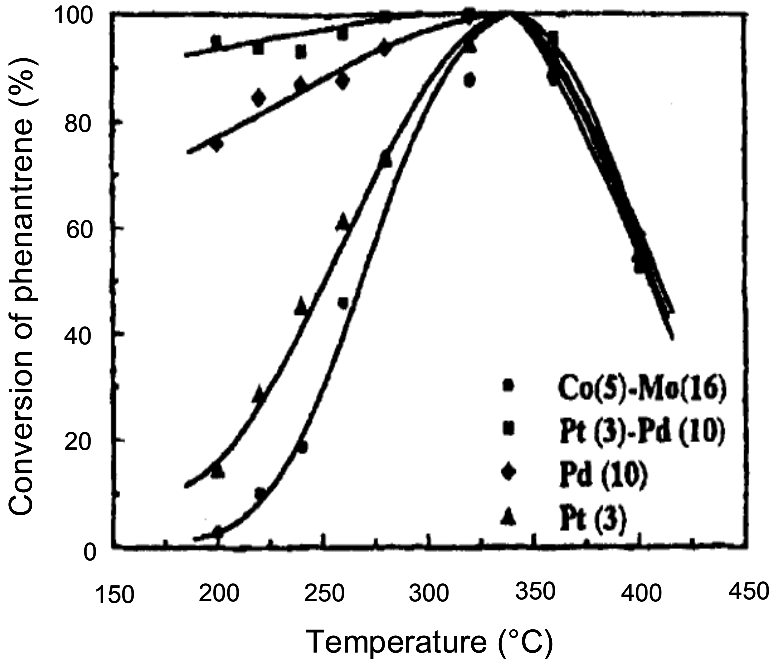

Figure 8. Conversion of phenantrene hydrogenation as a function of temperature on several catalysts [48]

To the right of the maximum of the curves the equilibrium rate is limiting the hydrogenation process and to the left, the hydrogenation rate is kinetically limited by the temperature. This is why catalysts from the platinum group with a high activity are preferred over less active sulfided catalysts. High hydrogen pressures on the other hand favor a low equilibrium concentration of the aromatic compounds.

Many reaction mechanisms have been proposed for naphthalene hydrogenation with a first order dependence in the aromatic reactant [49]. Therefore the true activation energy can be calculated from the observed apparent activation energy by subtracting the sum of adsorption energies of the aromatic molecule and hydrogen. The adsorption energies provide the major contribution to the true activation energy. Adsorption energies for aromatic compounds are in the range of 100-140 kJ/mol [50]. The hydrogenation is sequential, with the rate of tetralin hydrogenation being an order of magnitude less than that of naphthalene hydrogenation. Tetralin is a typical molecule targeted in deep hydrotreating (DHT) [51-54]. Under typical reaction conditions (p_{H2} = 50 bar, T = 320°

C), the formation of the hydrogenated products (i.e., *cis*- and *trans*-decalin) is thermodynamically strongly favored [55] with trans-decalin as the thermodynamically preferred compound. The thermodynamic equilibrium between naphthalene, tetralin, *cis*- and *trans*-decalin between 150 and 500°C at 50 bar is shown in Figure 9.

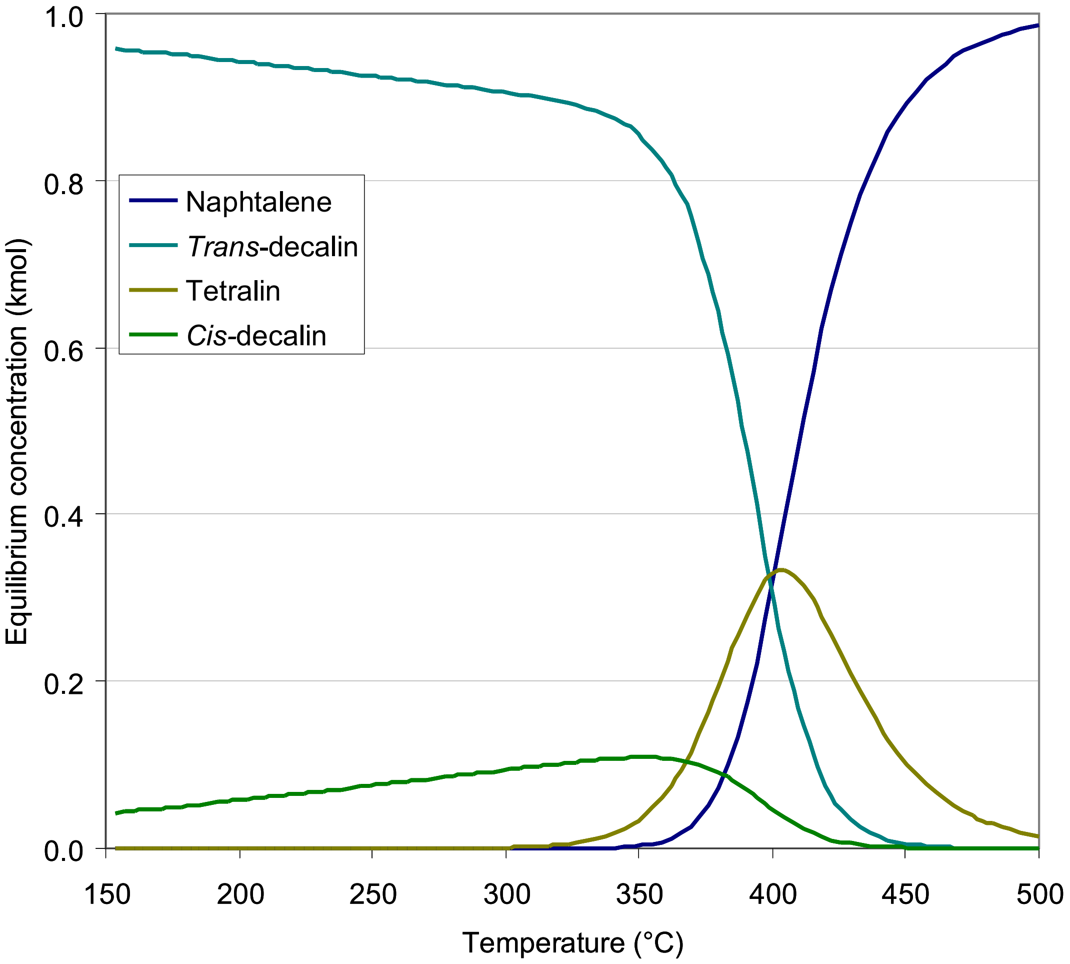

Figure 9. Thermodynamic equilibrium between naphthalene, tetralin, *cis*- and *trans*-decalin between 150 and 500°C at 50 bar [55].

Hydrogenation of C=C double bonds on metals should be intrinsically *cis* in character [56], however, the formation of *trans*- decalin is always observable [57]. According to Weitkamp [58], this depends on the consecutive desorption and re-adsorption of the partially hydrogenated intermediate, $\Delta^{1,9}$ – octalin, as shown in Figure 10.

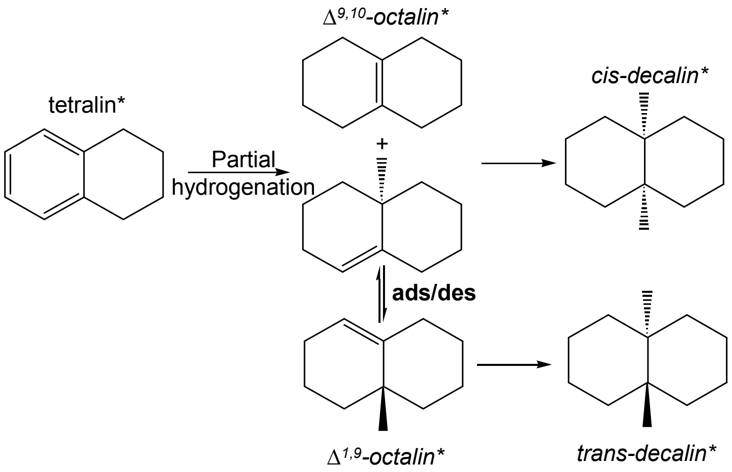

Figure 10. Step-hydrogenation of an adsorbed tetralin molecule to *cis*- and *trans*-decalin [54].

Any factors that reduce the strength of interaction of the olefinic intermediate with the surface will also favor the selectivity to the *trans* isomer. Therefore, the *cis* to *trans* selectivity can be considered as an indication of electronic state of metal hydrogenation catalysts [59, 60].

2.4 Industrial process options for deep hydrotreatment

New requirements in fuel specifications have been the dominant force for the development and introduction of new catalysts and processes for hydrotreating. The application of single stage processes, which have been designed for bulk HDS and that could be modified at relatively low costs, used to be an attractive option. As highlighted above, thermodynamic considerations limit the use of higher reaction temperatures in deep hydrogenation of aromatics. Therefore, when the sulfur content has to be reduced below 150 ppm and HDA is a prerequisite, single stage processes are not a realistic option, especially when refractory feeds have to be treated.

In current commercial deep hydrotreating processes a second stage with a highly active noble metal catalyst offers the best solution for achieving the required aromatics reduction at moderate hydrogen partial pressures. In the first stage Ni-Mo or Co-Mo catalysts are widely used to reduce sulfur and nitrogen containing compounds that are known to be strongly poisoning to noble metals in addition to some aromatics saturation. Sulfur and nitrogen removal allows the use of a noble metal catalyst at low reaction temperatures in the second stage after an intermediate gas separation and stripping in between the two stages [61]. Examples of licensors of this two stage process are Shell [62], Lummus-Criterion and IFP (Institute Français du Pétrole) [63]. Haldor Topsøe [64] was one of the pioneers to design units for hydrodearomatization of diesel using noble metal catalysts. The Topsøe two-stage HDS/HDA process is illustrated below in Figure 11.

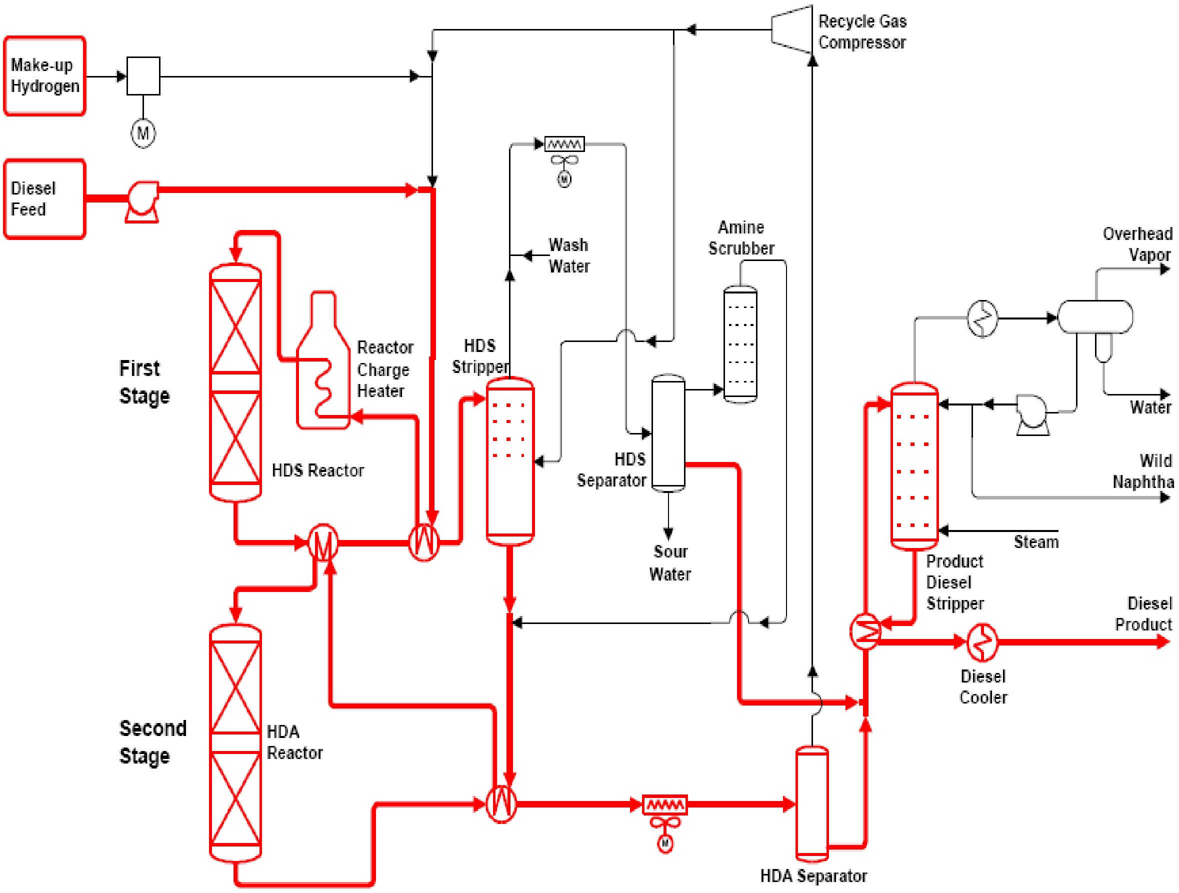

Figure 11. Diesel Upgrading – Topsøe’s Two-stage Process [65]

The first stage is a conventional hydrotreating step performed at typically 370° C and 70 bar over a base-metal catalyst to reduce the feed sulfur and nitrogen contents to sufficiently low levels. In this step sulfur is representatively reduced from 6515 to 9 wt ppm, nitrogen from 775 to 3 wt ppm and the total aromatics concentration from 33 to 24 wt% [65]. This allows the second stage noble-metal catalyst to perform the required degree of dearomatization at a high LHSV. Following this first stage hydrotreating, the diesel leaving the separator contains a significant quantity of dissolved hydrogen sulfide and ammonia, which is removed in an intermediate stripper column, using recycle hydrogen as the stripping medium. The hydrogen sulfide and ammonia containing off-gas is then purified in an amine scrubber. The stripped diesel and scrubbed hydrogen are then fed to the second stage, hydrodearomatization reactor. The catalyst used for dearomatization is a noble metal catalyst. After the second dearomatization stage (T = 287°C, p = 70 bar), the diesel is steam stripped to remove small amounts of H_2S present in the oil and to adjust the front-end distillation temperature to meet flash point requirements for the product diesel. The final product contains only 1 wt ppm S and N, respectively, with a total aromatics concentration of 3.5 wt% [65].

A big advantage of the two-stage diesel HDS/HDA process is that it uses conventional hydrotreater technology at moderate pressure, which enables the potential maximum reuse of equipment during the revamp of existing units.

2.5 Catalysts and nature of catalytic sites for deep hydrodearomatization

Noble metals are known to be the most active catalysts in the deep saturation of aromatics. Besides monometallic catalysts several bimetallic catalysts that consist of combinations of Pt, Pd, Rh, Ru and Re have been widely studied.

Thus, some studies have been devoted to the nature of the active phase on supported monometallic catalysts such as ruthenium or rhodium in hydrodearomatization [66, 67]. The ruthenium or rhodium sulfide phase was identified as the active phase for aromatics hydrogenation.

Especially Pt-Pd has attracted a lot of attention being the catalyst most commonly used in the second stage for aromatics saturation in a two-stage diesel HDS/HDA process.

Moreover conventional hydrotreating catalysts promoted by a noble metal can be found in the literature.

Unfortunately noble metal hydrogenation catalysts are swiftly poisoned by small amounts of sulfur and nitrogen organic compounds present in the feed. However, because in industrial feeds several heteroaromatic compounds are present, considerable attention has been paid recently to developing catalysts with high hydrogenation activity while maintaining strong resistance to poisoning by small amounts of sulfur and nitrogen containing compounds in the feed stream. Several attempts have been made to minimize the poisoning effects of heteroatoms.

The resistance to poisoning by heteroatoms can be influenced by adding a second noble metal to Pt, changing the particle size, or changing the acid-base properties of the carrier.

2.5.1 Role of the acidity for the activity and sulfur resistance of noble metals

Acidic supports have been shown to have a significant influence on the sulfur sensitivity of noble metals. Noble metal catalysts loaded on zeolites or other acidic supports reveal a higher hydrogenation activity and better sulfur resistance than Al_2O_3 or TiO_2 supports [68]. That trend was observed for aromatics hydrogenation over microporous zeolites [60] and mesoporous aluminosilicate molecular sieves [69].

The main drawback of these strongly acidic supports is that they cause excessive coke formation and hydrocracking of the feedstock leading to a decrease in the middle distillate yields. The hypothesis that the deactivation effect is related to acidic supports was proven by using less acidic carriers. In these studies, the zeolite was replaced by less acidic amorphous silica-alumina (ASA) in order to minimize the effect of the cracking activity, which accelerates the catalytic deactivation by coke and results in enhanced yields of naphtha and gas [70, 71]. Therefore, ASA carriers are a promising alternative for HDA, being also able to generate a moderate sulfur resistance [68, 72-76]. The studies performed by Vannice et al. [77-79] found that the activity of Pt and Pd catalysts for benzene and toluene hydrogenation was much higher when loaded on ASA compared with an $A1_2O_3$ supported catalyst. The enhancement of the activity was explained by the more acidic nature of ASA as a support. Corma et al. found that the sulfur resistance and saturation activity of aromatics hydrogenation catalysts was improved by using MCM-41 materials as a support for noble metal catalysts [80]. The higher saturation activity of naphthalene on Pt/MCM-41, in comparison to Pt/Al_2O_3, was again attributed to the medium strong acidity of the MCM-41 support and its higher metal dispersion [81]. It has been furthermore reported in the literature [73, 82] that the high sulfur tolerance and higher activity of zeolite supported Pt or Pd catalysts arises from the formation of electron deficient metal particles, Pt $^{\delta+}$ or Pd $^{\delta+}$ upon the hydrogenation of the aromatic compounds. The close contact between the strong acidic support and the small cluster of Pt or Pd atoms makes it possible for the electrons to be withdrawn from the noble metal thereby creating electron deficient metal clusters [83, 84]. Moreover, a lower electron densitiy on the metal weakens the metal–sulfur bond strength. As a result a significant increase in the activity of the hydrogenation reaction can be observed [73, 85-87].

The activity enhancement has been also explained by the presence of additional hydrogenation sites in the metal-acid interfacial region that contribute to the overall rate of hydrogenation. In addition to the conventional metal catalyzed aromatic hydrogenation, Wang et al. [88] suggested a second pathway for benzene hydrogenation involving acid sites of the support close to the metal particles and proposed a spillover of activated hydrogen from the Pt particles. In this mechanism carbenium ions adsorbed on acid sites could react with hydrogen that is delivered through interparticle migration from the metal phase.

2.5.2 Active phase and sulfur tolerance of bimetallic Pt-Pd catalysts

In order to increase the sulfur tolerance of noble metal catalysts, the main approach has been to increase the electron deficiency of noble metals by using acidic supports. However, this approach appears to be confined to hydrotreating feedstocks containing basic nitrogen containing compounds. Another approach to improve the sulfur resistance of a noble metal catalyst is to alloy the active component with another metal. The differences in the properties of bimetallic Pt–Pd systems compared to monometallic Pt or Pd have been generally attributed to alloying effects, i.e., electronic and ensemble effects. One possible explanation of the electronic effect is the formation of electron deficient Pt resulting from bimetallic Pt–Pd interactions [71]. However, it is not clear whether the Pt–Pd bimetallic interactions occur locally on the surface (isolated Pt cluster on the Pd surface) of Pt–Pd particles, or in Pt core – Pd shell structures where surface Pd atoms are becoming electron deficient. Albertazzi et al. [89] reported that Pt–Pd catalysts supported on basic mixed oxides of Mg–Al(O) showed high sulfur tolerance in the vapor-phase hydrogenation of naphthalene, although there was no contribution from acid sites of the supports. IR spectroscopy analyses of adsorbed CO in Pt–Pd metal particles indicated that the surface is significantly Pd rich but that Pd and Pt coexist at the surface. It was suggested that surface Pd contributes to the hydrogenation, but surface Pt was responsible for the hydrogenolysis/ring-opening reaction without acidic contributions of the support as well as for the sulfur tolerance. This is in agreement with the role of Pt reported by Navarro *et al* [71]. Guillon et al. [90] prepared two Pt–Pd/Al_2O_3 catalysts with Pd/Pt ratios of 1/1 and 4/1, respectively. These catalysts revealed alloy formation confirmed by EXAFS and also showed Pd surface segregation to the cluster surface, which was proven by low energy ion spectroscopy and IR spectroscopy analyses of adsorbed CO. During the hydrogenation reaction in the presence of sulfur, they observed that Pt and S modify the electronic properties of Pd atoms (electron transfer from Pt to Pd to increase the Pd–S bond strength) in the Pd–S shell and Pt core (sulfur free) systems. It remained unclear whether the electronic effect becomes dominant only after Pt–Pd alloy formation of highly dispersed particles smaller than 2 nm in diameter.

The local structure of bimetallic Pt–Pd particles, irrespective of the presence or absence of their electronic effects after bimetallic formation, is also important in retarding the sintering of the bimetallic Pt–Pd particles under sulfiding and hydrotreating conditions. In the case of zeolite supported bimetallic Pt-Pd catalysts, it is favorable that the molar ratio of Pt-Pd is not greater than unity. Sulfur tolerance of the bimetallic Pd–Pt particles surface was maximized at a Pd/Pt atomic ratio of 4/1 over USY zeolites (SiO_2/Al_2O_3 molar ratio of 15–40) [91].

3 Scope of the thesis

Oxide supported Pt catalysts possess excellent activity for aromatics hydrogenation, but are unfortunately swiftly poisoned by small amounts of sulfur and nitrogen containing compounds. It has been reported that the use of acidic supports and bimetallic Pt-Pd alloy formation can increase the catalyst's resistance towards sulfur poisons. However, the function of different kinds of acid sites, their optimal concentration and the different properties of supported monometallic small Pt clusters compared to Pt-Pd on the catalyst performance is still ambiguous. In the present work, which was a close collaboration with Shell International Chemicals B.V., these questions were addressed studying the hydrogenation of tetralin by oxide supported Pt and Pt-Pd catalysts in the absence and presence of sulfur (as dibenzothiphene) and nitrogen poison (as quinoline). The proposal of a detailed reaction mechanism by correlating catalyst acidic and metallic properties with the kinetic results of this reaction is the basis for tailoring highly active aromatics hydrogenation catalysts operating at industrial conditions, where always sulfur and nitrogen containing compounds are present in the feedstock.

In Chapter 2 a detailed characterization study of the silica, alumina and amorphous silica-alumina (ASA 5/95, 20/80 and 55/45 containing 5, 20 and 55% of alumina in silica, respectively) supported Pt and Pt-Pd catalysts is presented. Multinuclear Nuclear Magnetic Resonance (^{27}Al (3Q) MAS NMR) allows determining the concentration of pure alumina domains and quantifying the aluminosilicate phase in the amorphous carriers, where aluminum tetrahedral species are separated by silica ones. Brønsted (BAS) and Lewis acid site (LAS) concentrations on the catalyst surface are determined by pyridine adsorption followed by IR spectroscopy. Transmission Electron Microscopy (TEM), X-ray Absorption Spectroscopy (EXAFS) and X-ray absorption near-edge structure (XANES) are used to investigate the average particle sizes, the morphology and the electronic properties of the Pt and Pt-Pd nano-clusters anchored by incipient wetness impregnation. Combining the results obtained from these characterization techniques leads to a clear picture of the oxide supported noble metal catalysts, which is necessary to understand differences in their catalytic behavior.

The catalytic activities of the well characterized Pt/ASA catalysts in the hydrogenation of tetralin at 160 – 190°C in the presence of quinoline and dibenzothiophene (DBT) are presented in Chapter 3. DBT was chosen as the model compound for sulfur poisoning, because it is one of the typical sulfur compounds present in diesel fuel with a well explored catalytic chemistry. For the same reasons quinoline was selected as typical nitrogen containing heteropolyaromatic compound. The mechanistic aspects of the residual aromatics hydrogenation performance are discussed based on the kinetic results and characterization of the used Pt catalysts by TEM, CO/pyridine adsorption IR, EXAFS and XANES. A new model for the hydrogenation of tetralin in the presence of poisons is proposed.

In industrial processes aromatics hydrogenation is carried out at higher temperatures as applied in the kinetic study in Chapter 3. Moreover Pt-Pd catalysts are widely used due to their good sulfur tolerance. Therefore tetralin hydrogenation in the absence and presence of DBT and quinoline is also studied in an industrial relevant temperature range (280 – 320°C) using SiO_2, Al_2O_3 and ASA supported Pt and Pt-Pd catalysts. The discussion focuses on the role of BAS and the influence of bimetallic alloy formation on the catalysts tetralin hydrogenation performance and poison tolerance. Analysis of the spent catalyst samples by TEM and CO/pyridine adsorption IR is carried out in order to confirm the reaction mechanism suggested in Chapter 3 and to explain the always observed continuous catalytic deactivation.

In Chapter 5 the main results and conclusions of this thesis are summarized.

Acknowledgment

Shell International Chemicals B.V. is gratefully thanked for the generous financial support through the experimental phase of the project.

4 References

1. State of Washington, Department of Community, Trade & Economic Development (CTED).
2. J. G. Smith, *Presentation for the California Air Pollution Control Officers Association 2004, Diesel - What the future holds*. 2004.
3. P. D. Tony Pytte, Sasol Chevron Australian Gas to Liquids Project, *Global Trends in Transport Fuels and the Role of Natural Gas*. 2003, Extract from presentation to AIE Perth Branch, 16 October 2003.
4. B. Tippe, Oil & Gas Journal, 2005. 103(46) 18.
5. E. Benazzi, *The Evolving Worldwide Diesel Market & Composition*, in *7th Annual European Fuels Conference*. 2006 Paris.
6. E. H. Gue, The Energy Letter, 2006.
7. State of Washington, Department of Community, Trade & Economic Development (CTED)
8. C. P. Haelsig and J. Turner, Hydrocarbon Processing, 2006. 85(2) 41.
9. J. Adler, Int. J. Appl. Ceram. Technol., 2005. 2(6) 426.
10. M. Matti Maricq, Journal of Aerosol Science, 2007. 38(11) 1079.
11. Indiana, Department of environmental management, *Health Effects of Diesel Emissions*.
12. EPA, *National Air Quality and Emissions Trends Report*. 2000. p. 11, 27, 122
13. G. Nagy, H. Jenő, V. Zoltán, P. György, and K. Dénes, Petroleum & Coal, 2007. 49(1) 24.
14. D. J. Ball and R. G. Stack, *Catalysis and automotive pollution control II. (A. Crucq, Ed.)*. 1991, Amsterdam: Elsevier Science Publishers. 337.
15. J. H. Johnson, S. T. Bagley, L. D. Gratz, and D. G. Leddy, SAE Tech. Pap. Ser., 1994. 940233.
16. H. Klein, E. Lox; T. Kreuzer, M. Kawanami, M.; T. Ried and K. Bachmann, SAE Tech. Pap. Ser., 1998. 980196.
17. V. Beckhoven, 1991. SAE Paper 910608.

18. M. Booth, J. M. Marriott and K. J. Rivers, 2nd IMechE Int. Sem. on the Fuels for Automative and Industrial Diesel Engines, 1993 45.
19. K.E. Egebäck, G. Mason, U. Rannug and R. Westerholm, *Catalysis and automative pollution control II (A. Crucq, Ed.)*. 1991, Amsterdam: Elsevier Science Publishers. 75.
20. Official Journal of the European Union, Volume 0058
21. F. Anisits, O. Hiemesch, W. Dabelstein, J. Cooke, and M. Mariott, Motortechnische Zeitschrift, 1991. 52(5) 242.
22. P. Q. E. Clothier, A. Mosie and H. O. Pritchard, Chem Soc. Rev., 1993. 22 101.
23. B. Freedman and M. O. Bagby, J. Am. Oil Chem. soc., 1990. 67 565.
24. M. Gairing, W. W. Lange, A. Le Jeune, D. Naber, A. Reglitzky, and A. Schäfer, Motortechnische Z., 1994. 55 8.
25. J. C. Wall and S. K. Hoekman, SAE paper 1984 841364.
26. Environmental Protection Agency, Control of Diesel Fuel Quality; Advance Notice of Proposed Rulemaking.64 Federal Register 26142-261581999.
27. G. H. Unzelman, NPRA Annual Meeting, 1987.
28. C. Bertoli, N. Del Giacomo, B. Iorio, and M. V. Prati, SAE paper 1993. 932733.
29. Official Journal of the European Union. L 076 22/03/2003 0010.
30. *http://energycommerce.house.gov/cleandiesel/secbysec.shtml*.
31. D. B. Kittelson, W. F. Watts, J. P. Johnson, C. Rowntree, M. Payne, S. Goodier, C. Warrens, H. Preston, U. Zink, M. Ortiz, C. Goersmann, M. V. Twigg, A. P. Walker and R. Caldow, Journal of Aerosol Science, 2006. 37(9) 1140.
32. R. C. Santana, P. T. Do, M. Santikunaporn, W. E. Alvarez, J. D. Taylor, E. L. Sughrue, and D. E. Resasco, Fuel, 2006. 85(5-6) 643.
33. S. Eijsbouts, Appl. Catal. A, 1997. 158 53.
34. B. C. Gates, Katzer J.R., Schuit G.C.A., *Chemistry of catalytic processes*. 1979, New York: McGraw-Hill.
35. C. Song and X. Ma, Appl. Catal. B: Env., 2003. 41(1-2) 207.
36. M. Houalla, N. K. Nag, A. V. Sapre, D. H. Broderick and B. C. Gates, AIChE Journal, 1978. 24(6) 1015.

37. J. Mijoin, V. Thevenin, N. Garcia Aguirre, H. Yuze, J. Wang, W. Z. Li, G. Perot, and J. L. Lemberton, Appl. Catal. A: General, 1999. 180(1-2) 95.
38. J. R. Katzer and R. Sivasubramian, Catal. Rev.-Sci. Eng., 1979. 20 155.
39. A. Streitwieser and C. H. Heathcock, *Introduction to Organic Chemistry*. 1976, New York: Macmillan.
40. G. Perot, Catalysis Today, 1991. 10 447.
41. E. Furimsky and F. E. Massoth, Catal. Rev.-Sci. Eng., 2005. 47 297.
42. C.N. Satterfield and S.H. Yang, Ind. Eng. Chem. Process Des. Dev., 1984. 23 11.
43. S. S. Shih, K. N. Mathur, J. R. Katzer, H. Kwart and A. B. Stiles, Am. Chem. Soc., Div. Pet. Chem., 1977. 22 919.
44. H. Topsoe, B. S. Clausen and F. E. Massoth, *Hydrotreating Catalysis*. 1996, Berlin: Springer.
45. C. Moreau and P. Geneste, *Factor affecting the reactivity of organic model compounds, in Hydrotreating Reactions, Theoretical Aspects of Heterogeneous Catalysts* 1990, New York: van Nostrand Reinhold 256.
46. S. B. Jaffe, Ind. Eng. Chem. Process Des. Dev., 1974. 13 34.
47. R. C. Reid, J. M. Pruasnitz and T. K. Sherwood, *The Properties of Gases and Liquids*. 1977, New York: McGraw-Hill.
48. W. Qian, Y. Yoda, Y. Hirai, A. Ishihara and T. Kabe, Appl. Catal. A, 1999. 184 81.
49. A. V. Sapre and B. C. Gates, Ind. Eng. Chem. Process Des. Dev., 1981. 20 68.
50. M. A. Keane, J. Catal., 1997. 166(2) 347.
51. C.C. Costa Augusto, J.L. Zotin and A. Da Costa Faro, Catal. Lett., 2001. 75 1.
52. L. Le Bihan and Y. Yoshimura, Fuel, 2002. 81 491.
53. J. L. Rousset, L. Stievano, F. J. Cadete Santos Aires, C. Geantet, A.J. Renouprez, and M. Pellarin, J. Catal, 2001. 202 163.
54. M. F. Williams, B. Fonfé, C. Woltz, A. Jentys, J. A. R. van Veen and J. A. Lercher, J. Catal., 2007. 251(2) 497.
55. *HSC Chemistry for Windows*, Outokumpu Research Oy: P.O. Box 60, FIN – 28101 Pori, Finland.
56. K. Schrage and R.L. Burwell, J. Am. Chem. Soc., 1966. 88 4555.

57. E. P. Martins, D. A. G. Aranda, F. L. P. Pessoa, J. L. Zotin, and Braz, J. Chem. Eng., 2000. 17 1603.
58. A. W. Weitkamp, Adv. Catal., 1968. 18 1.
59. L. Fisher, V. Harlé and S. Kasztelan, Hydrotreatment and Hydrocracking of oil fractions, 1996. 31 261.
60. A. D. Schmitz, G. Bowers and C. Song, Catal. Today, 1996. 31 45.
61. W. H. J. Stork, Hydrotreat. Hydrocrack. Oil Fractions, 1997 106 49.
62. J. K. Minderhoud and J. Lucien. 1988: Eur. Patent.
63. N. Marchal, S. Kasztelan and S. Mignard, *Chemical Industry*, ed. M. Dekker. 1994, New York. 315.
64. B. H. Cooper and A. Stanislaus, Catal. Rev. -Sci. Eng., 1994. 36(1) 75.
65. F. E. Bingham and P. Christensen. *Revamping HDS Units to Meet High Quality Diesel Specifications*. in *Asian Pacific Refining Technology Conference*. 2000. Kuala Lumpur, Malaysia.
66. M. Breysse, M. Catteno, V. Kougionas, J. C. Lavalley, F. Mauge, J. L. Portefaix, and J. L. Zotin, J. Catal., 1997. 168 143.
67. B. Moraweck, G. Bergeret, M. Catteno, V. Kougionas, C. Geantet, J. L. Zotin, J. L. Portefaix and M. Breysse, J. Catal., 1997. 165 45.
68. C. Song, Chemtech, 1999 26.
69. K. M. Reddy and C. Song, Mat. Res. Soc. Sym. Proc. Ser., 1997. 454 125.
70. T. Fujikawa, K. Idei, T. Ebihara, H. Mizuguchi and K. Usui, Appl. Catal. A: Gen., 2000. 192(2) 253.
71. R. M. Navarro, B. Pawelec, J. M. Trejo, R. Mariscal and J. L. G. Fierro, Journal of Catalysis, 2000. 189(1) 184.
72. B. H. Cooper and B. B. L. Donnis, Appl. Catal. A Gen., 1996. 137(2) 203.
73. P. Gallezot, *Catalysis by Zeolites*, ed. B. Imelik, et al. Vol. 5. 1980, Amsterdam: Elsevier Science. 227.
74. M. J. Girgis and B. C. Gates, Ind. Eng. Chem. Res., 1991. 30(9) 2021.
75. H. Yosuda and Y. Yoshimura, Catal. Lett., 1997. 46 43.
76. H. Yasuda, T. Sato and Y. Yoshimura, Am. Chem. Soc. Div. Petrol. Chem. Prepr., 1997. 42 580.

77. S. D. Lin and M. A. Vannice, Journal Of Catalysis, 1993. 143(2) 563.
78. S. D. Lin and M. A. Vannice, J. Catal., 1993. 143 539.
79. D. Poondi and M. A. Vannice, J. Catal., 1996. 161 742.
80. A. Corma, A. Martínez and V. Martínez-Soria, J. Catal., 1997. 169(2) 480.
81. Y. W. Chen and C. P. Li, J. Chin. Inst. Chem. Eng., 1997. 28 375.
82. S. T. Homeyer, Z. Karpinski and W. M. H. Schatler, J. Catal., 1990. 123 60.
83. R. A. Dalla Betta and M. Boudart. in *Proc. 5th Int. Congr. on Catalysis*. 1973. North Holland.
84. R. A. Dalla Betta, M. Boudart, P. Gallezot and R. S. Weber, J. Catal., 1981. 69 514.
85. M. T. Tri, J. Massardier, P. Gallezot and B. Imelik, *Metal-support and Metal Additives Effects in Catalysis*, ed. B. Imelik, et al. Vol. 11. 1982, Amsterdam: Elsevier. 141.
86. F. Figueras, R. Gomez and M. Primet, Advances in Chemistry Series, 1973(121) 480.
87. T. T. Phuong, J. Massardier and P. Gallezot, J. Catal., 1986. 102(2) 456.
88. J. Wang, Q. Li and J. Yao, Appl. Catal. A: General, 1998. 175 191.
89. S. Albertazzi, G. Busca, E. Finocchio, R. Glockler and A. Vaccari, J. Catal., 2004. 223 372.
90. E. Guillon, J. Lynch, D. Uzio, and B. Didillon, Catalysis Today, 2001. 65(2-4) 201.
91. Y. Yoshimura, M. Toba, T. Matsui, M. Harada, Y. Ichihashi, K. K. Bando, H. Yasuda, H. Ishihara, Y. Morita, and T. Kameoka, Appl. Catal. A: Gen., 2007. 322 152.

Chapter 2

Characterization of ASA-supported platinum and platinum-palladium catalysts by ^{27}Al (3Q) MAS NMR, IR, TEM, EXAFS and XANES

A series of well-defined catalysts based on platinum and bimetallic platinum-palladium nanoparticles supported on amorphous silica-alumina (ASA) with varying composition was prepared by incipient wetness impregnation. The concentration of Lewis and Brønsted acid sites determined by pyridine adsorption was adjusted by varying the amount of aluminosilicate domains, which were quantitavely characterized by ^{27}Al (MQ) MAS. The preparation method led to small and uniform Pt (0.7 - 0.9 nm) and Pt-Pd (1.4-1.8 nm) particles on all aluminum containing supports. X-ray Absorption Spectroscopy (EXAFS) confirmed the particle sizes determined by Transmission Electron Microscopy (TEM) and clearly showed that Pt-Pd alloys were formed. The bimetallic Pt-Pd alloy exhibited a different electronic band structure compared to monometallic Pt according to X-ray absorption near-edge structure (XANES). Ionic $Pt^{x\delta+}$ - $xPd^{\delta-}$ bonds are formed leading to very electron deficient Pt atoms. CO adsorption was monitored by infrared spectroscopy (IR). From that a structural model for the Pt-Pd alloys is proposed with both Pt and mainly Pd at the surface of the nanoparticles.

1 Introduction

The interest in the acidic properties of amorphous silica-alumina (ASA) originates in their use in large scale industrial catalytic processes [1, 2]. ASAs have been used as catalysts or catalyst supports for reactions such as isomerization, alkylation of aromatic molecules, oligomerization of olefins and cracking. Similarly to zeolites, ASAs increase the resistance of a supported metal against sulfur poisoning in deep hydrotreating of diesel fuels [3, 4]. Due to their larger pores, ASA based materials allow, however, the conversion of significantly larger molecules than zeolite catalysts. The former materials have also a higher concentration of moderately strong Brønsted acid sites, but a lower concentration of strong ones compared to zeolites. In this context, it should be noted that strongly acidic supports can lead to excessive coking and overcracking.

The resistance to poisoning by heteroatoms can be further influenced by adding a second noble metal to the very active hydrogenation catalyst Pt. Especially Pt-Pd has attracted a lot of attention being the catalyst most commonly used in the second stage for aromatics saturation in a two stage diesel HDS/HDA process

It has been reported that the properties of the support (i.e., the chemical composition, as well as the type, strength and concentration of acid sites) influence the catalytic activity of noble metal catalysts. However, the physicochemical properties of the catalysts studied varied in a wide range and no systematic study of Pt/ASA and Pt-Pd/ASA catalysts has been performed exhibiting: (i) small Pt particles within a narrow size distribution in comparison to Pt-Pd clusters with the same total metal content and (ii) a gradual change in the acidic composition of the ASA supports. This is necessary to correlate acidity, metal-support interactions and alloy formation with the catalytic activity in the hydrogenation of aromatics in the presence and absence of sulfur and nitrogen poisons.

Here, a comprehensive characterization of alumina, ASA and silica supported Pt and Pt-Pd catalysts is reported with a view to elucidating the structural origin of the acid sites in amorphous ASA supports. To directly probe the local configuration of the metal cations, a solid-state magic angle spinning (MAS) NMR study was performed. For aluminosilicates (ASA, zeolites, etc.), ^{27}Al NMR provides useful information on the Al-O environments, since chemical shifts strongly depend on the coordination number of aluminum [5-7]. Pyridine adsorption infrared spectroscopy was applied in order to quantify the amount of Lewis and Brønsted acid sites.

Moreover, the size and properties of the Pt and Pt-Pd particles were explored in detail using transmission electron microscopy (TEM), extended X-ray absorption fine structure (EXAFS) spectroscopy, X-ray absorption near-edge structure (XANES) and CO adsorption infrared spectroscopy.

2 Experimental

2.1 Preparation and chemical composition of oxide supported Pt and Pt-Pd-catalysts

A series of Pt and Pt-Pd based catalysts supported on silica-alumina (ASA 5/95, 20/80 and 55/45 containing 5, 20 and 55% of alumina in silica, respectively), as well as on pure alumina and silica, were prepared by incipient wetness impregnation. The ASA supports were produced from a gel formed at pH = 7.5 by mixing (i) acetic acid with $AlCl_3 \bullet 6H_2O$ in distilled water (pH = 1.5) and (ii) sodium silicate with NH_4OH (pH = 12). The gel was washed with a diluted solution of ammonium acetate to eliminate Na^+ cations. Subsequently, it was dried at 400 K and calcined at 783 and 949 K for 2 hours, respectively. The supports were impregnated with an aqueous solution of $Pt(NH_3)_4(NO_3)_2$ for the Pt catalysts or with $Pt(NH_3)_4(NO_3)_2$ and $Pd(NO_3)_2 \cdot xH_2O$ for the Pt-Pd samples. Subsequently, the catalysts were dried for 2 hours on a rolling bank and calcined at 453 K (10 min) and 563 K (6 min) in a rotating tube oven. Finally the samples were reduced at 623 K in a flow of hydrogen (2 h).

2.2 Atomic absorption spectroscopy

The chemical compositions of the carriers and the supported catalysts were determined by atomic absorption spectroscopy (AAS) using a UNICAM 939 spectrometer.

2.3 Specific surface area and porosity

The surface areas and pore diameters were calculated from nitrogen adsorption measurements carried out at 77.4 K using a PMI automated BET sorptometer. Prior to the measurements, the samples were outgassed at 523 K for 20 hours. The surface areas as well as the micro- and mesopore distributions were calculated applying the BET and BJH theories.

2.4 Nuclear magnetic resonance spectroscopy

For the ^{27}Al (MQ) MAS NMR experiments, the catalyst samples were packed at ambient conditions into 4 mm ZrO_2 rotors. The spectra were obtained by a Bruker Avance AMX 400 NMR spectrometer operating at 104.263 MHz for aluminium. Magic angle spinning was carried out at a rotation rate of 12 kHz. The chemical shifts were referenced to solid $(NH_4)Al(SO_4)_2$ (δ_{Al} = - 0.59 ppm). For the MQ MAS NMR experiments, a three-pulse sequence, including z-filtering and the states acquisition method, was applied [8]. After Fourier transformation, the 2D spectra were sheared [9], so that the orthogonal projection on the isotropic axis gives the 1D spectrum free of any anisotropic broadening. The quantification of different ^{27}Al species was performed by fitting the corresponding MAS spectra using the parameters determined in the 3Q MAS experiments [10]. For the fitting, a program developed by the group of Prof. Kentgens, University of Nijmegen, was used. This program uses Gaussian distributions for the quadrupolar coupling constant and for the isotropic shift $\delta_{\iota so}$.

2.5 Infrared spectroscopy

2.5.1 Pyridine adsorption

A Perkin Elmer 2000 spectrometer operating at a resolution of 4 cm^{-1} was used in the IR studies. Prior to the IR investigation, the catalyst samples were activated in vacuum ($p = 10^{-6}$ mbar) at 673 K for 1 h. The activated catalyst samples were exposed to pyridine ($p_{(Py)} = 10^{-2}$ mbar) at 423 K for 0.5 h. After outgassing at 423 K for 1 h, the spectrum was recorded. Subsequently, the temperature was raised to 673 K and maintained at this temperature for 1 h. Then the sample was cooled to 423 K before recording the spectrum. The procedure of a complete pyridine adsorption IR experiment is summarized in Figure 1.

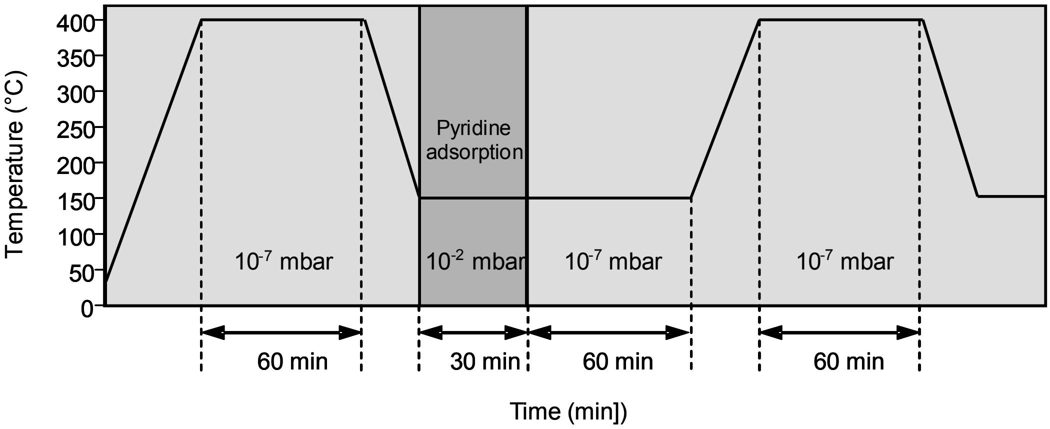

Figure 1. Procedure of a pyridine adsorption IR spectroscopy experiment.

The concentration of pyridine molecules retained on Brønsted and Lewis acid sites after outgassing at 673 K was defined as the concentration of strong acid sites. The difference between the concentrations of acid sites after outgassing at 423 K and 673 K is defined as the concentration of weak acid sites. The molar extinction coefficients published by Emeis were used for the quantification of Lewis (LAS) and Brønsted (BAS) acid sites [11].

2.5.2 CO adsorption

In the CO adsorption IR spectroscopy experiments, using a Bruker ISF88 spectrometer, the catalyst was activated in H_2 at 623K for 1 hour followed by 1 hour at the same temperature in vacuum ($p = 10^{-6}$ mbar) to remove hydrogen. Then, the catalyst was cooled to 313 K. Carbon monoxide was adsorbed at 0.005, 0.05 and 0.5 mbar until no more change in the IR spectrum was observed. At the end of the experiment, the sample was evacuated for 15 minutes at 10^{-6} mbar and an additional spectrum was recorded. The procedure of a complete CO adsorption IR experiment is summarized in Figure 2.

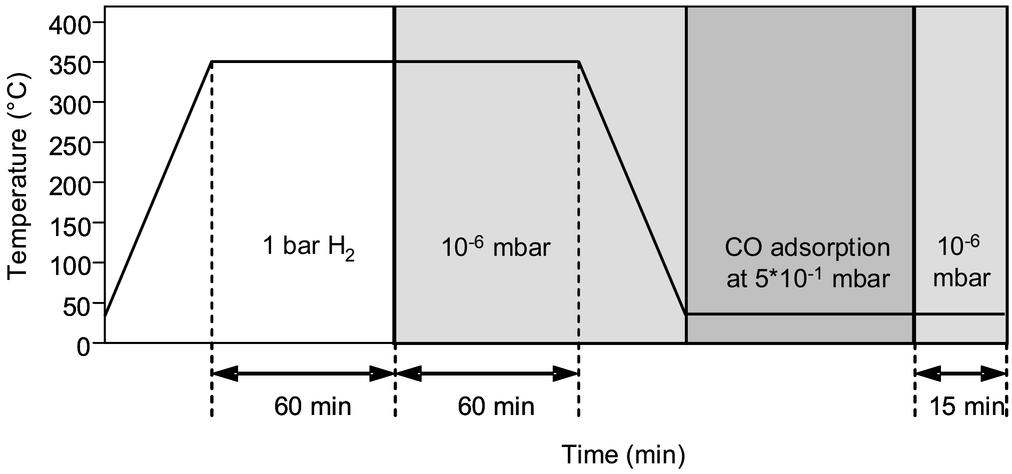

Figure 2. Procedure of a CO adsorption IR spectroscopy experiment.

2.6 Transmission electron microscopy (TEM)

The pre-reduced catalysts samples, stored under air, were grinded, suspended in ethanol and ultrasonically dispersed. Drops of the dispersions were applied on a copper grid-supported carbon film. A JEM-2010 Jeol transmission electron microscope operating at 120 kV was used.

2.7 Extended X-ray absorption fine structure

X-ray absorption spectra were collected at the beamlines X1 and C, HASYLAB, DESY, Hamburg, Germany. The storage ring was operated at 4.5 GeV and an average current of 100 mA. The Si (311) double crystal monochromator was detuned to 60% of the maximum intensity to minimize the intensity of higher harmonics in the X-ray beam. The fresh catalysts prepared as self supporting wafers were reduced in situ (H_2, T = 588 K for 2 h) followed by He treatment at 588 K for 1 h to remove adsorbed H_2. The X-ray absorption spectra were collected at the Pt L_{III} edge (11564 eV) or the Pd K edge (24365 eV) at 77K (EXAFS), 323 K and 588K (XANES). For the EXAFS and XANES analysis, the scattering background was subtracted using a polynomial function and all spectra were normalized to unity. The position of the edge was calibrated using the spectra of a simultaneously measured Pt or Pd foil. The VIPER and XANDA software were used for analyzing the datasets [12].

For EXAFS analysis the oscillations were weighted with k^2 and Fourier transformed within the limits $k = 3.0 – 14.0$ Å $^{-1}$. The local environment of the Pt and Pd atoms was determined from the EXAFS using the phase-shift and amplitude function for Pt-Pt, Pd-Pd, Pt-O and Pd-O calculated assuming multiple scattering processes (FEFF Version 8.30) [13, 14].

3 Results

3.1 Chemical composition and textural properties of the oxide supported Pt and Pt-Pd catalysts

The chemical compositions of the Pt and Pt-Pd catalysts obtained in the AAS measurements are compiled in Table 1. The concentration of residual sodium cations was smaller than 33 μmol•g^{-1} for all ASA supports. The platinum content was approximately 0.8 wt. % for all Pt catalysts. The alumina containing catalysts had specific surface areas between 274 and 464 m^2•g^{-1}, i.e., higher than that of pure silica support (185 and 167 m^2•g^{-1} for Pt and Pt-Pd, respectively).

Table 1.Chemical composition and textural properties of the calcined catalysts. The chemical composition refers to water free catalysts.

	Concentration (wt %)				BET Surface area (m^2·g^{-1})	Ø Pore diameter (nm)
Catalyst	Pt	Pd	SiO_2	Al_2O_3		
Pt/Al_2O_3	0.83	-	0.0	99.2	312	8.4
Pt/ASA (55/45)	0.78	-	44.0	55.2	274	4.2
Pt/ASA (20/80)	0.82	-	79.0	20.2	322	14.3
Pt/ASA (5/95)	0.80	-	93.8	5.4	464	6.0
Pt/SiO_2	0.78	-	99.2	0.0	185	22.5
Pt-Pd/ASA (55/45)	0.30	0.55	55.2	44.0	313	4.0
Pt-Pd/ASA (20/80)	0.30	0.52	79.0	20.2	308	13.9
Pt-Pd/ASA (5/95)	0.29	0.50	5.4	93.8	452	6.1
Pt-Pd/SiO_2	0.30	0.52	99.2	0.0	167	24.8

3.2 Characterization of the aluminum species

^{27}Al 3Q MAS NMR spectroscopy was used to probe the chemical environment of aluminum nuclei in the catalysts and to determine the coordination flexibility of aluminum species in the noble metal catalysts on alumina containing carriers. Quantitative analysis of the computed 1D ^{27}Al MAS NMR spectra was performed to obtain the concentrations of 4-, 5- and 6-fold coordinated Al atoms using the quadrupolar and isotropic parameters derived from the 3Q MAS NMR spectra. Additional information was obtained from treating the catalysts with ammonia prior to the NMR measurements. Van Bokhoven et al. demonstrated that this treatment transforms some octahedrally coordinated aluminum species into tetrahedrally ones providing additional information on the state of octahedral Al species [15-17].

The results were presented in a recent publication [18] and are summarized in Table 2.

Table 2. Concentrations of different types of structural aluminum in alumina and in ASA supported Pt catalysts (in mol %) [18].

	Tetrahedral (T-Al)		Pentahedral (P-Al)		Octahedral (O-Al)	
Catalyst	Parent	NH_3 treated	Parent	NH_3 treated	Parent	NH_3 treated
Pt/Al_2O_3	30	33	0	0	70	67
Pt/ASA (55/45)	25	34	26	26	49	40
Pt/ASA (20/80)	46	60	24	29	30	11
Pt/ASA (5/95)	69	87	0	0	31	13

As the catalysts used in the present work originated from new synthesis batches ^{27}Al 3Q MAS NMR and 1D ^{27}Al MAS NMR were applied in order to confirm the chemical environment of the aluminum species and, thus, the equal properties of the Al containing supports compared to the previous batches. Moreover, 1D ^{27}Al MAS NMR was also used for Pt-Pd/ASA (20/80) and Pt-Pd/ASA (55/45) to see a possible influence on the Al surroundings by the bimetal. The results are presented in Figure 3.

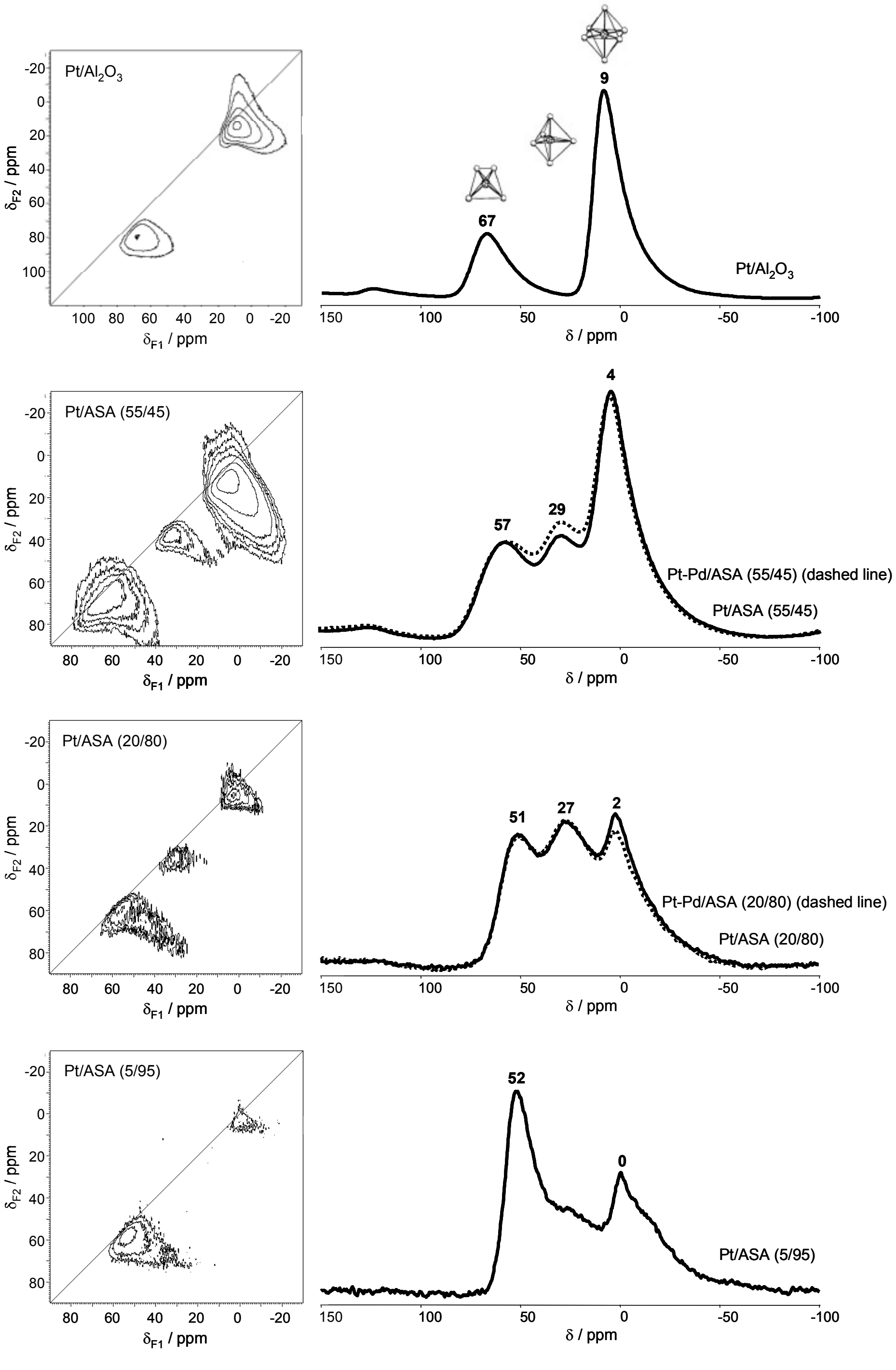

Figure 3. ^{27}Al (MQ) MAS NMR study of Pt and Pt-Pd catalysts supported on alumina and ASA carriers. Left side: ^{27}Al 3Q MAS NMR spectra recorded at 104.263 MHz using a spinning rate of 12 kHz. Right side: Corresponding 1D ^{27}Al MAS NMR.

The ^{27}Al 3Q MAS NMR spectrum of Pt/Al_2O_3 showed signals at 66 and 9 ppm arising from tetrahedral (T) and octahedral (O) aluminum, respectively [19]. Both peaks consist of a sharp component and a rather broad signal. The narrow resonance of T-Al is centered close to the diagonal. This indicates that the corresponding aluminum species experiences a relatively small quadrupolar interaction (i.e., $\delta_{iso} \cong \delta_{F2}$), pointing to a rather symmetric environment. The signal attributed to O-Al, stretched in F_1 and F_2 dimension, results from a large distribution in isotropic chemical shifts and quadrupolar interactions. This indicates a broad distribution of the electron density and the degree of distortion among the aluminum-oxygen tetrahedra. The fractions of T and O aluminum were approximately 30 and 70 %, respectively. The resonance of T-Al was much stronger in the ^{27}Al 3Q MAS NMR spectrum of Pt/ASA (55/45) than in Pt/Al_2O_3. However, the signal was less resolved and its center shifted upfield to about 57 ppm. A new resonance at approximately 29 ppm was observed. In the literature, peaks at this position have been assigned to strongly distorted tetrahedral [20, 21] or pentavalent aluminum species [22-25]. In the present case, the MQMAS spectrum contained a contribution at δ_{F2} = 43 ppm, which allows the unambiguous assignment of this resonance to five-fold coordinated aluminum [16]. The aluminum species in octahedral environment were observed at 4 ppm. All peaks in the MQMAS spectrum of Pt/ASA (55/45) were broadened in the isotropic (F_2) and anisotropic (F_1) dimensions. This suggests that the topological distribution of aluminum atoms in the amorphous sample and the bond angles are not well defined. The NMR spectra of Pt/ASA (20/80) showed a remarkable upfield shift of the peak attributed to T-Al to 51 ppm. This upfield shift is assigned to a significant dilution of aluminum in the neighborhood of a central Al atom. Some geometric factors (e.g., disordered Al-O-Si angles [26]) and the composition of the further coordination shells could also influence the resonance of T-Al [27]. The other aluminum species were found in six- and five-fold coordination states (resonance signals at 2 and 27 ppm, respectively).

The NMR spectra of Pt/ASA (5/95) showed a substantial contribution of the four-fold coordinated aluminum (at 52 ppm) and only minor resonance signals of five- and six-fold coordinated aluminum indicating that the majority of the aluminum atoms adopted tetrahedral coordination.

3.3 Acidic properties of the noble metal catalysts

The acidic properties of the noble metal catalysts were characterized by pyridine adsorption/desorption followed by IR spectroscopy. The resulting spectra of the Pt catalysts are presented in Figure 4. The results of the Pt-Pd samples are not shown and discussed as they showed almost identical concentrations of Lewis and Brønsted acid sites as the Pt catalysts.

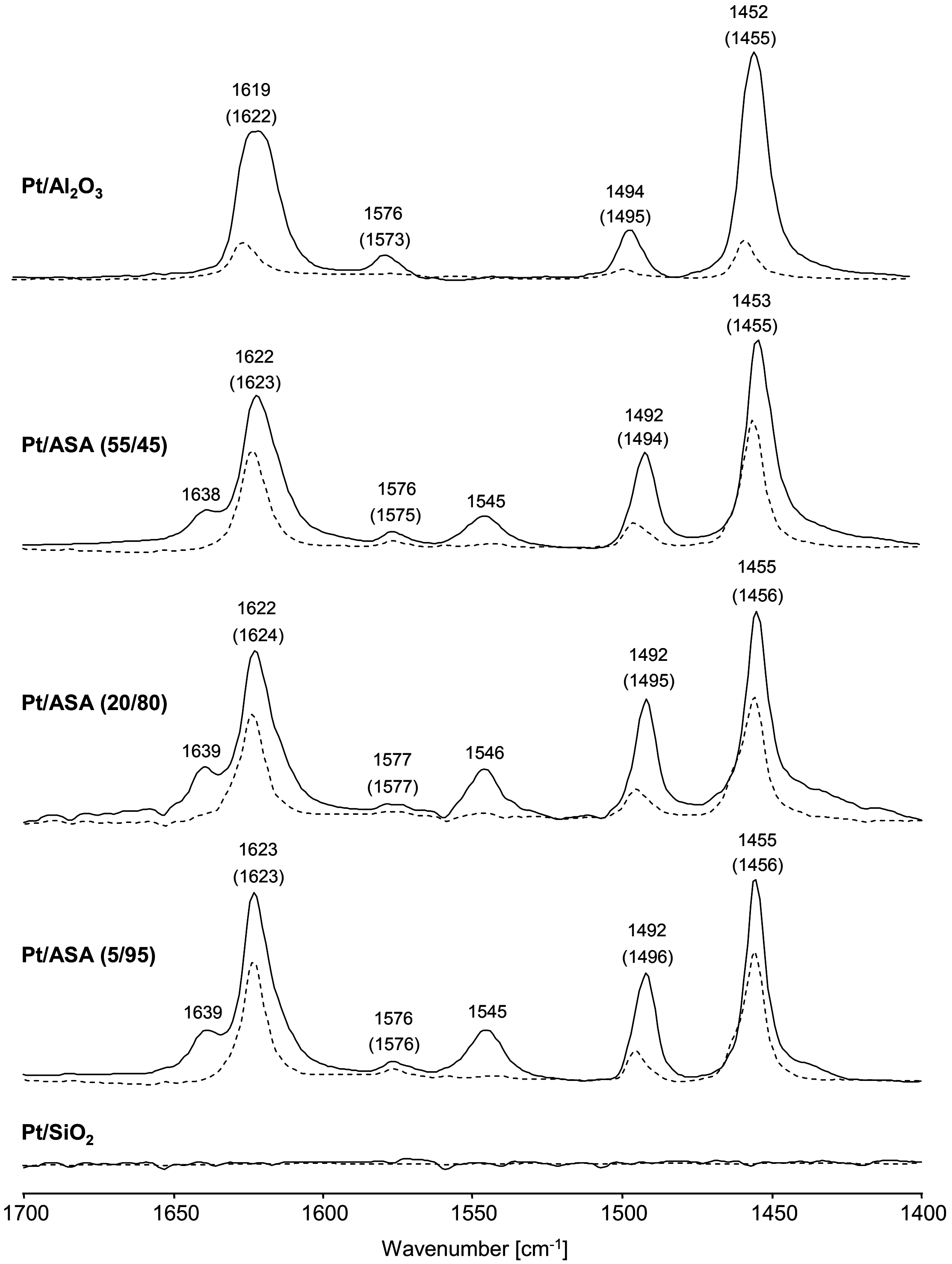

Figure 4. IR spectra of pyridine adsorbed on alumina, ASA and silica supported Pt catalysts at T = 423 K, p(Py) = 2· 10^{-2} mbar (continuous lines). Spectra recorded upon temperature treatment (i.e., after outgassing at 673 K for 1 h) are also included (dashed lines, band values in brackets).

With Pt/Al_2O_3, the IR spectrum of adsorbed pyridine (after evacuation at 423 K) showed bands at 1452, 1494, 1576 and 1619 cm^{-1}. The bands show that pyridine is solely coordinated to Lewis acid sites. After evacuation at 673 K, bands were still observed at 1455, 1494 and 1622 cm^{-1}. In particular, the wavenumber of the first band indicates that alumina has very strong Lewis acid sites next to weaker ones characterized by the band at 1452 cm^{-1}.

In the spectra of Pt/ASA samples, nearly identical bands were detected indicating the presence of pyridine adsorbed on Lewis acid sites (PyL species). Moreover, an additional band at 1545 - 1546 cm^{-1} and a broad shoulder at 1638 - 1639 cm^{-1} appeared. Both are characteristic for pyridinium ions indicating chemisorption of pyridine on Brønsted acid sites. After the evacuation at 673 K the intensity of all bands decreased. The peak at 1545 and the shoulder at 1638 cm^{-1} disappeared almost completely showing that the Brønsted acid sites are relatively weak.

With Pt/SiO_2 no peaks were found after pyridine adsorption and outgassing at 423 K indicating that the support was totally neutral.

Table 3 summarizes the quantification of the Lewis (LAS) and Brønsted (BAS) acid sites arising from the pyridine adsorption studies.

Table 3. Concentration of BAS and LAS calculated from pyridine adsorption IR spectroscopy.

Catalyst	Acid site concentration (µmol/g)	
	BAS	LAS
Pt/Al_2O_3	0	143
Pt/ASA (55/45)	23	121
Pt/ASA (20/80)	42	103
Pt/ASA (5/95)	35	90
Pt/SiO_2	0	0

The concentration of Lewis acid sites was highest for the Pt/Al$_2$O$_3$ catalyst and decreased when the concentration of alumina decreased in the Pt/ASA samples. In contrast, Brønsted acidity was not observed for the Pt/Al$_2$O$_3$ catalyst and passed through the maximum concentration of 42 μmol·g^{-1} at 20 % concentration of alumina in the ASA supported catalyst.

3.4 Characterization of the noble metal nanoclusters

The supported Pt and Pt-Pd metal particles were characterized by EXAFS, XANES, TEM and CO adsorption IR spectroscopy.

3.4.1 Platinum particles

Figure 5 shows the Fourier Transforms of the experimental EXAFS data and the Pt-O fitted contributions of Pt/SiO$_2$, Pt/Al$_2$O$_3$ and the Pt/ASAs after calcination and before H$_2$ reduction.

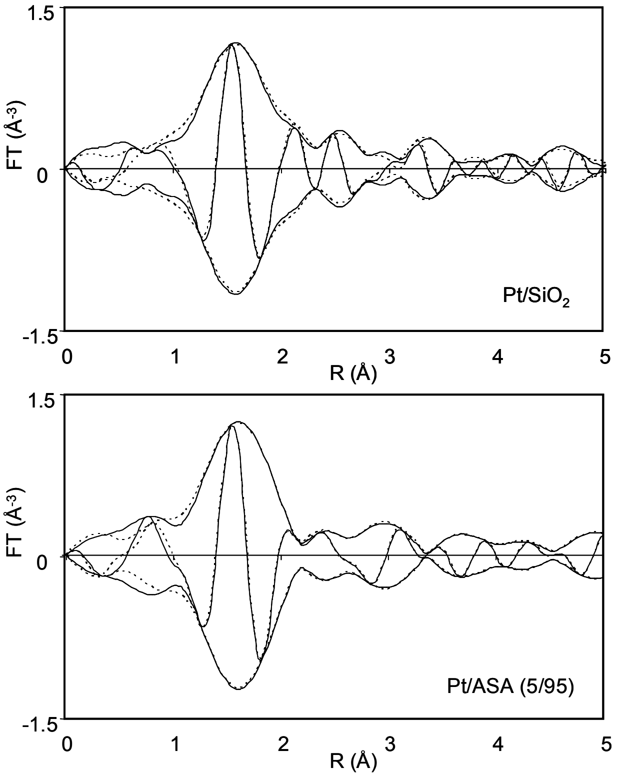

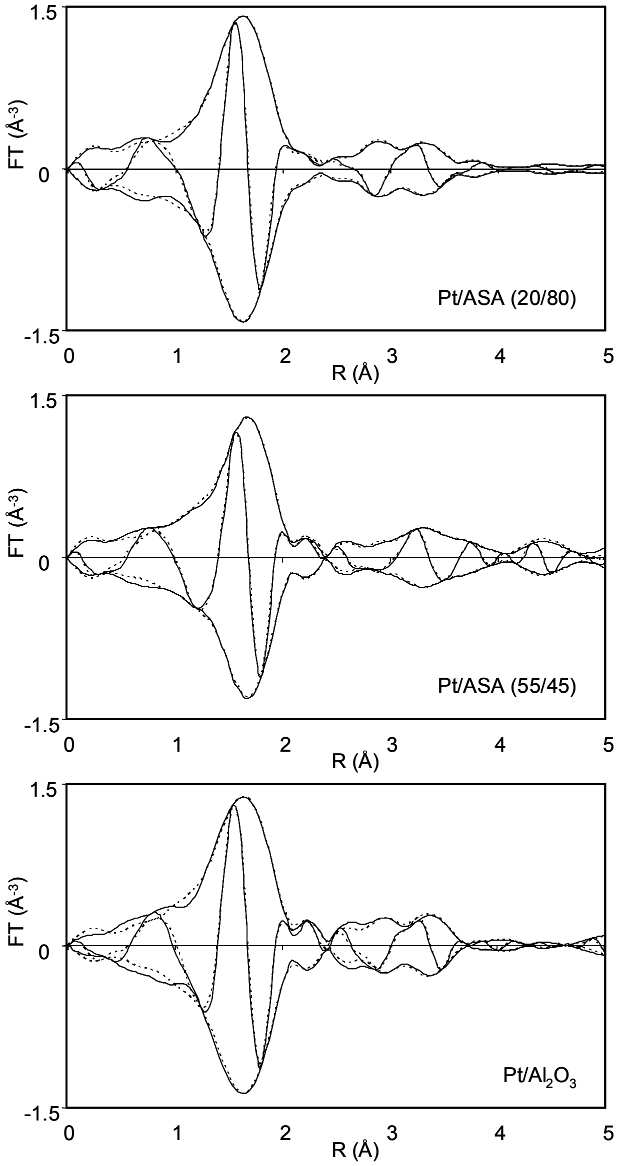

Figure 5. Fourier transforms (k^2 –weighted, Δk 3.0-12 Å^{-1}) of the Pt/ASAs, Pt/Al$_2$O$_3$ and Pt/SiO$_2$ (solid lines) and their Pt-O fitted contributions (dotted lines) before H$_2$ reduction.

Both amplitude and imaginary part of the model are in good agreement with the experimental data and Pt-O contributions are clearly observed at somewhat below 2Å for all oxide supported Pt catalysts showing the formation of platinum oxide particles The peaks visible at distances larger than 2Å are due to first and higher shell Pt-Pt scattering that are insignificant as the Pt-Pt coordination numbers are only somewhat above 0. The results of the Pt-O fitted contributions are summarized in Table 4.

Table 4. Results of the EXAFS analysis of the Pt catalysts before reduction.

Catalyst	N_{Pt-O}	r_{Pt-O} (Å)	$10^3 \cdot \Delta\sigma^2$ (Å^2)	ΔE_0 (eV)
Pt/Al_2O_3	4.6	2.00	7.9	13.0
Pt/ASA (55/45)	4.0	2.03	6.7	15.8
Pt/ASA (20/80)	4.6	2.01	7.1	13.7
Pt/ASA (5/95)	4.0	2.03	4.5	16.3
Pt/SiO_2	4.7	2.01	10.7	13.3
Pt oxide	6	2.05	-	-

The small Pt particle sizes of all Pt catalyst are quantitatively visible from the Pt-O coordination numbers between 4.0 and 4.7 that are significantly lower compared to bulk platinum oxide. Pt/Al_2O_3, Pt/ASA (55/45), Pt/ASA (20/80), Pt/ASA (5/95) and Pt/SiO_2 showed interatomic Pt-O distances of 2.00 -2.03 Å agreeing very well with the theoretical distance of 2.05 Å between Pt and O in bulk platinum oxide The analysis of Pt-Pt coordinations did not lead to significant backscattering and were, thus, not included in the fits presented.

After H_2 reduction at 623K for two hours the Pt catalysts were characterized by TEM and again by XAFS spectroscopy.

Representative TEM pictures of all silica containing Pt catalysts are shown in Figure 6.

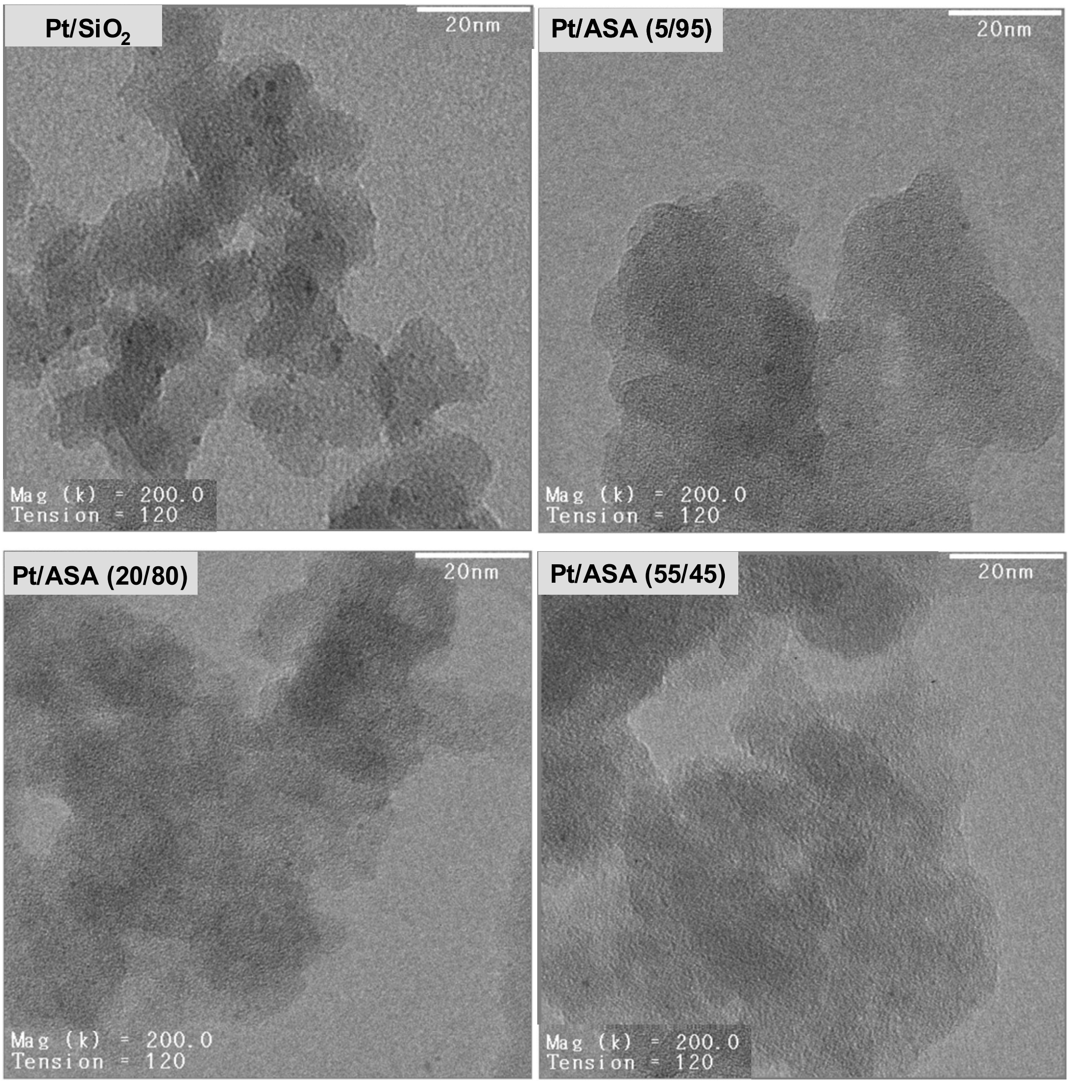

Figure 6. TEM micrographs of Pt/SiO_2, Pt/ASA (5/95), Pt/ASA (20/80) and Pt/ASA (55/45).

The darker grey areas in the TEM pictures represent particles of the amorphous oxidic supports. The thicker the support particle the darker the grey tone becomes. The well distributed small black dots represent the Pt particles.

The size histograms corresponding to about 300 analyzed Pt particles per catalyst were derived from the TEM micrographs of the alumina, ASA, and silica supported Pt catalysts and are compiled in Figure 7.

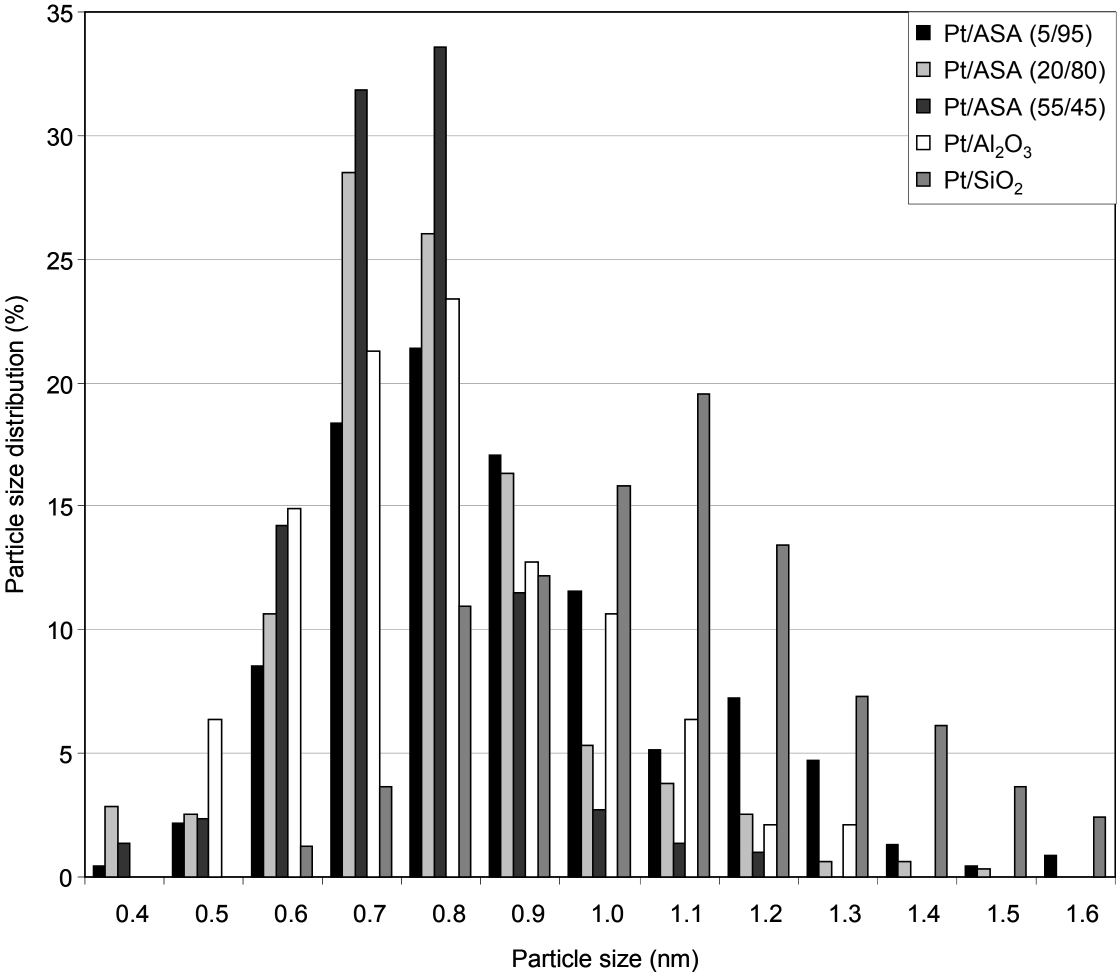

Figure 7. Size histograms of alumina, ASA, and silica supported Pt catalysts.

For Pt on alumina and the ASAs the mean cluster size determined by TEM was about 0.8 nm with a narrow metal cluster size distribution. On the other hand, Pt/SiO_2 catalysts exhibited bigger metal particles (1.1 nm) with a somewhat broader Pt particle size distribution (see Table 5 and Figure 7).

As a second method to determine the average particle size after reduction, EXAFS was used in combination with modeling the particle size using a cuboctahedral shape (see Figure 8 and Figure 9) [28]. The results of the EXAFS analysis of the reduced samples are compiled in Table 5.

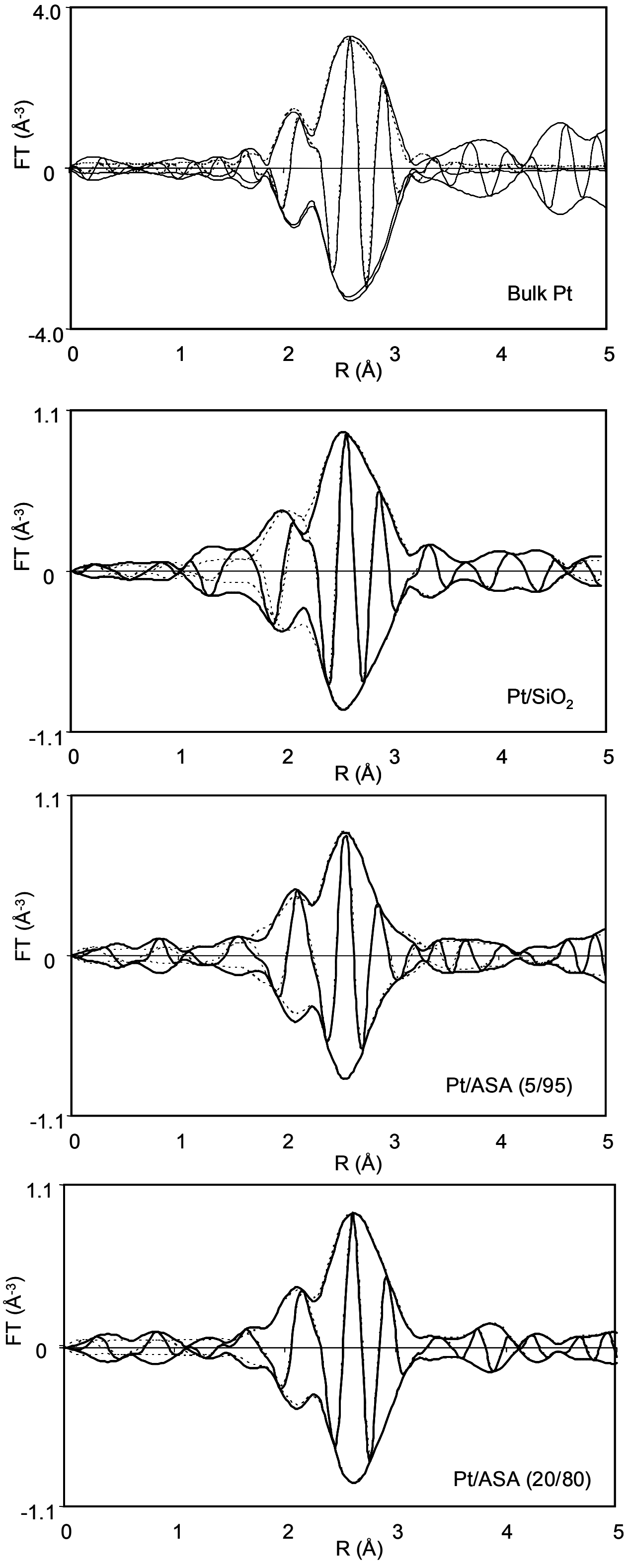
4.0
FT (Å-3)
0
-4.0
0
1
2
3
4
5
R (Å)
Bulk Pt
1.1
FT (Å-3)
0
-1.1
0
1
2
3
4
5
R (Å)
Pt/SiO2
1.1
FT (Å-3)
0
-1.1
0
1
2
3
4
5
R (Å)
Pt/ASA (5/95)
1.1
FT (Å-3)
0
-1.1
0
1
2
3
4
5
R (Å)
Pt/ASA (20/80)

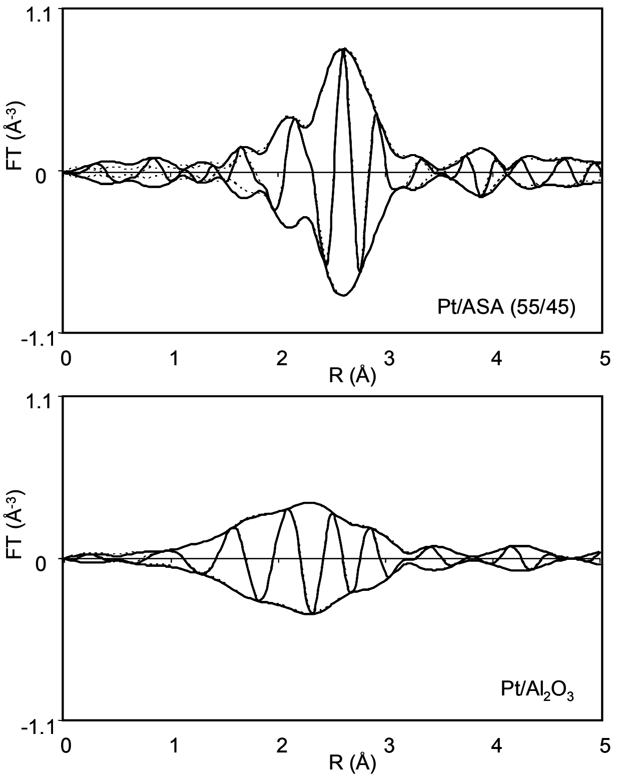

Figure 8. Fourier transforms (k^2 –weighted, Δk 3.5-14 $Å^{-1}$) of the Pt/ASAs and Pt foil (solid lines) and their Pt-Pt fitted contributions (dotted lines) after in situ H_2 reduction at 588 K.

The small particle sizes of the Pt/ASAs are qualitatively visible from the low heights of the Pt-Pt first shell (N_1) contributions at 2.75 Å compared to bulk Pt. Scattering from larger Pt-Pt shells at larger shells are visible at distances larger than 3.0 Å, but these peaks are too small and, thus, lead to useless fittings. The results of the EXAFS analysis of the Pt-Pt first shell contributions are compiled in Table 5.

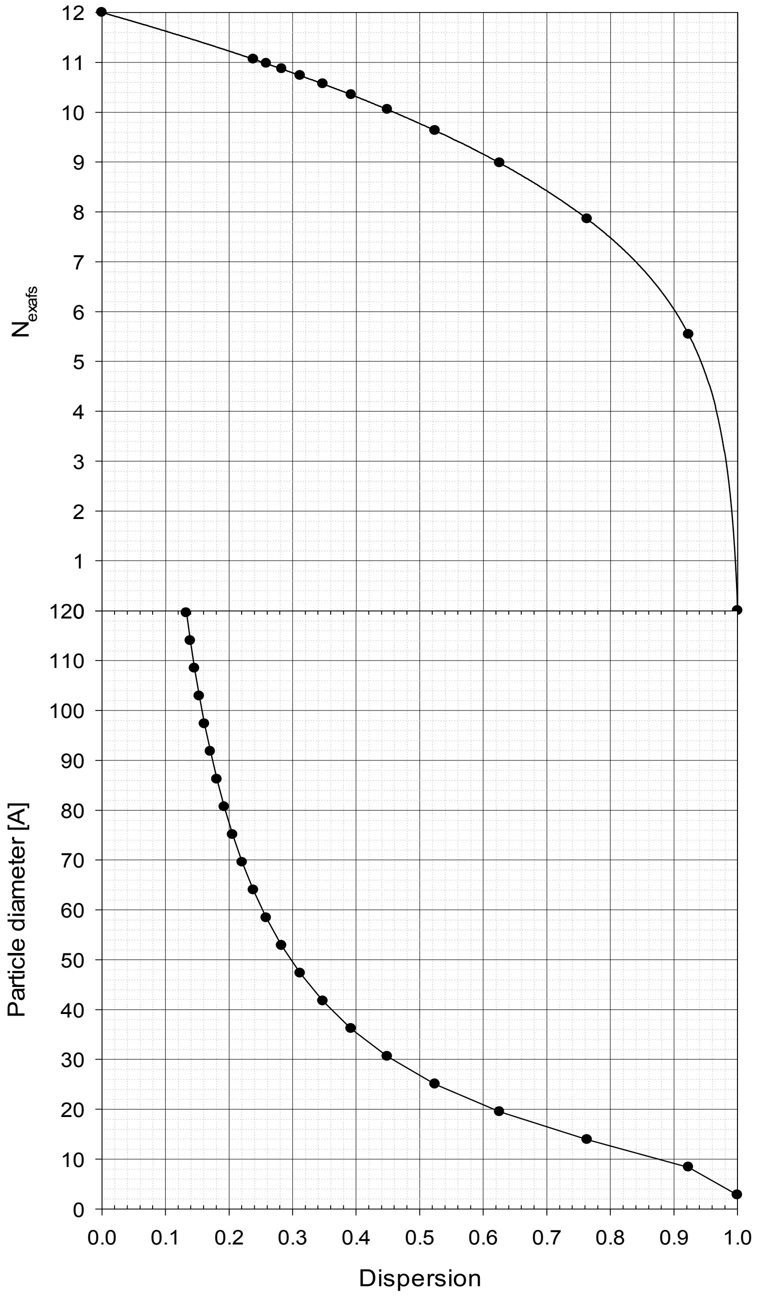

Figure 9.Determination of the platinum particle size based on cubooctahedral morphology.

Table 5. Results of the TEM and EXAFS analysis of the reduced Pt catalysts.

Catalyst	Particle size[1] (nm)	Particle size[2] (nm)	N_{Pt-Pt}	r_{Pt-Pt} (Å)	$10^3 \cdot \Delta\sigma^2$ (Å^2)	ΔE_0 (eV)
Pt/Al_2O_3	0.8	0.7	5.3	2.66	10.9	10.7
Pt/ASA (55/45)	0.8	0.8	5.7	2.75	6.9	10.4
Pt/ASA (20/80)	0.8	0.9	6.3	2.76	6.8	14.8
Pt/ASA (5/95)	0.9	0.8	5.7	2.76	6.1	10.5
Pt/SiO_2	1.1	1.1	7.0	2.74	7.6	12.8
Pt foil		-	12.0	2.76	3.4	11.1

[1] determined by TEM measurement

[2] determined by particle modeling

All Pt catalysts showed contributions from the Pt-Pt coordinations at similar distances compared to bulk Pt and the coordination numbers for the Pt contributions in the first shell were between 5.3 and 7.0 (see Table 5). Assuming a cuboctahedral shape for the Pt particles, the average coordination number, the metal dispersion and the particle size were estimated from the generic relations derived from models of the Pt particles (for details see ref. [28] and Figure 9). The Pt particle sizes derived with this method are 0.7, 0.8, 0.9, 0.8 and 1.1 nm for Pt/Al_2O_3, Pt/ASA (55/45), Pt/ASA (20/80), Pt/ASA (5/95) and Pt/SiO_2, respectively. The analysis of Pt-O and Pt-Al coordinations did not lead to significant backscattering and were, thus, not included in the fits presented.

The chemisorption of CO on oxide supported noble metal catalysts has been extensively studied by infrared spectroscopy. CO adsorbs mainly as a linear species on supported Pt to give a single intense infrared band centered at 2000 – 2100 cm^{-1} [29-32].

Figure 10 displays the IR spectra of adsorbed CO at 0.5 mbar and 40°C on the hydrogen activated oxide supported Pt catalysts. Spectra after evacuation for 15 min at 10^{-6} mbar are also presented.

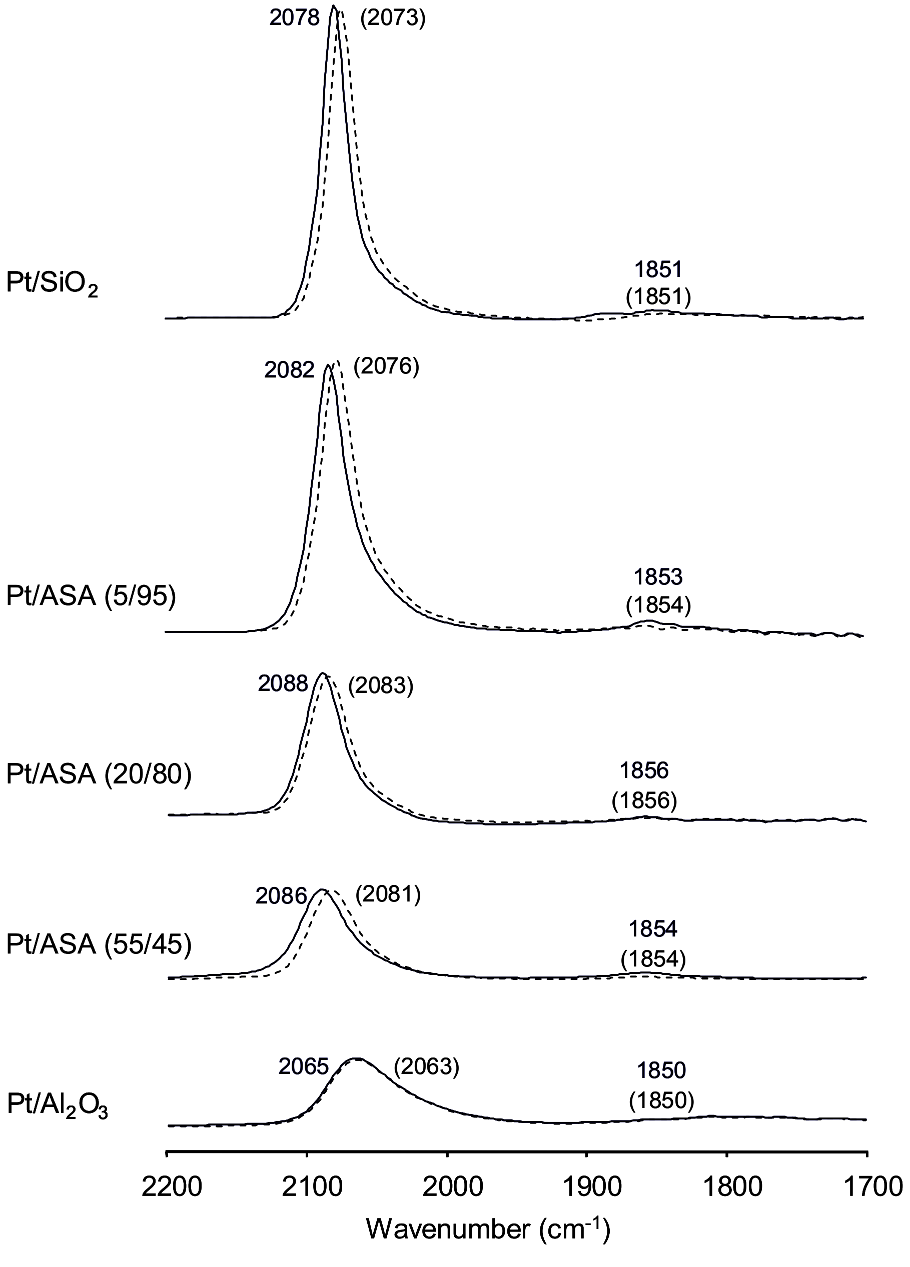

Figure 10. Infrared spectroscopy study of CO adsorbed on SiO_2, ASA and Al_2O_3 supported Pt catalysts at T = 40 ºC, $p_{(CO)} = 5\cdot10^{-1}$ mbar (continuous lines). Spectra recorded after evacuation for 15 min are also included (dashed lines, band values in brackets).

CO adsorption led to IR spectra consisting of a strong absorption band at 2078, 2082, 2088, 2086 and 2065 cm^{-1} and a very weak absorption at 1851, 1853, 1856, 1854 and 1850 cm^{-1} for Pt/SiO_2, Pt/ASA (5/95), Pt/ASA (20/80), Pt/ASA (55/45) and Pt/Al_2O_3, respectively. The larger peak corresponds to CO molecules adsorbed on metallic Pt in linear form (2065-2088 cm^{-1}). Coordination in bridged position weakened the C-O bond by п-electron back donation of the metal resulting in the small stretching frequency at lower wavenumbers (1850-1856 cm^{-1}) [29-32]. Apparently, CO adsorption in bridged position was insignificant on the Pt catalysts of this study. Evacuation at 10^{-6} mbar of the IR cell for 15 minutes did not decrease the band intensities showing the strong adsorption of CO on all Pt catalysts. Interestingly a small shift of 2-6 cm^{-1} to lower wavenumbers of the band from CO adsorbed linearly on Pt was observed upon this treatment. This phenomenon was also observed in other studies [31, 32], where it was assigned to lower CO surface coverage. Furthermore it can be seen that a higher Si/Al ratio of the supports led to higher band intensities (see also Table 6). Neutral Pt/SiO_2 and Pt/Al_2O_3 that do not reveal Brønsted acidity (see Figure 4 and Table 3) exhibit IR bands at lower wavenumbers compared to the Pt/ASAs.

3.4.2 Bimetallic platinum-palladium particles

After H_2 reduction at 623K for two hours the bimetallic Pt-Pd catalysts were also characterized by TEM and by XAFS spectroscopy.

Representative TEM pictures of all silica containing Pt-Pd catalysts are shown in Figure 11.

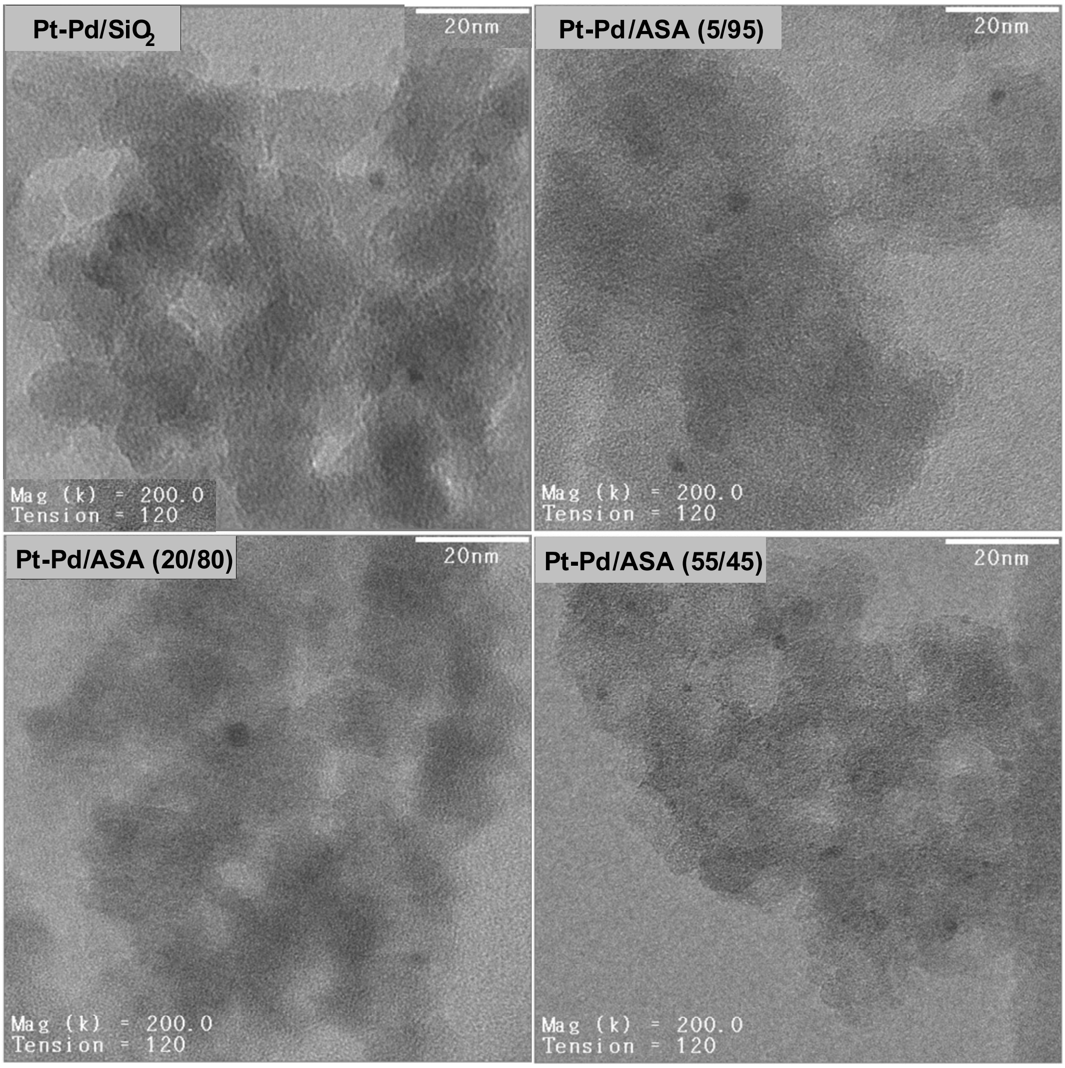

Figure 11. TEM micrographs of Pt-Pd/SiO_2, Pt-Pd/ASA (5/95), Pt-Pd/ASA (20/80) and Pt-Pd/ASA (55/45).

Equivalent to the Pt catalysts the darker grey areas in the TEM pictures represent particles of the amorphous oxidic supports. The thicker the support particle the darker the grey tone becomes. The well distributed small black dots represent the Pt-Pd particles.

The size histograms corresponding to about 300 analyzed Pt-Pd particles per catalyst were derived from the TEM micrographs of the ASA and silica supported Pt-Pd catalysts and are compiled in Figure 12.

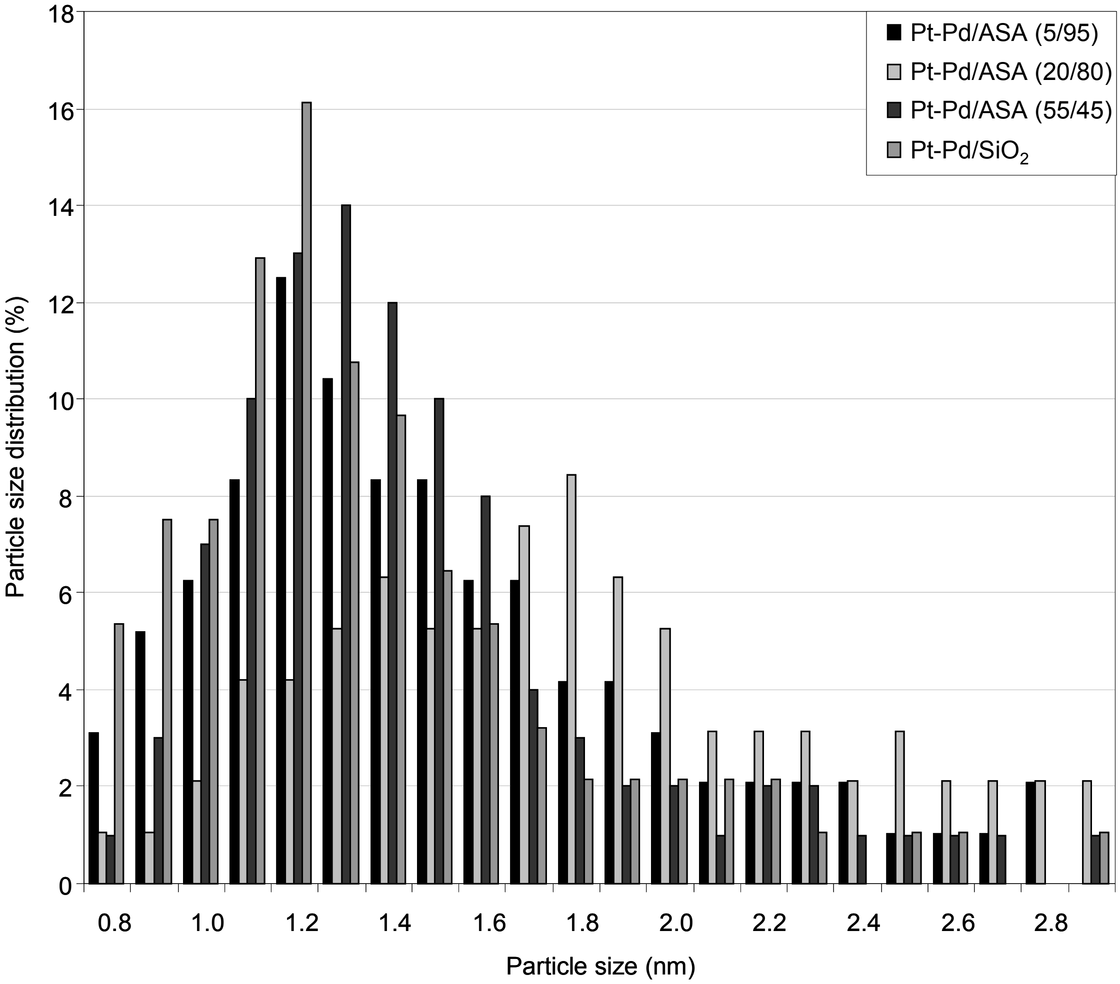

Figure 12. Size histograms of ASA and silica supported Pt-Pd catalysts.

For Pt-Pd/SiO$_2$, Pt-Pd/ASA (5/95), Pt-Pd/ASA (20/80) and Pt-Pd/ASA (55/45) the mean cluster sizes determined by TEM were 1.4, 1.6, 1.8 and 1.4 nm with a relatively large metal cluster size distribution between 0.8 and 3.0 nm (Figure 7).

EXAFS was used in order to characterize the morphology of the reduced bimetallic Pt-Pd clusters. The Fourier transforms of the EXAFS at the Pt L_{III} edge of all silica containing Pt-Pd catalysts are presented in Figure 13.

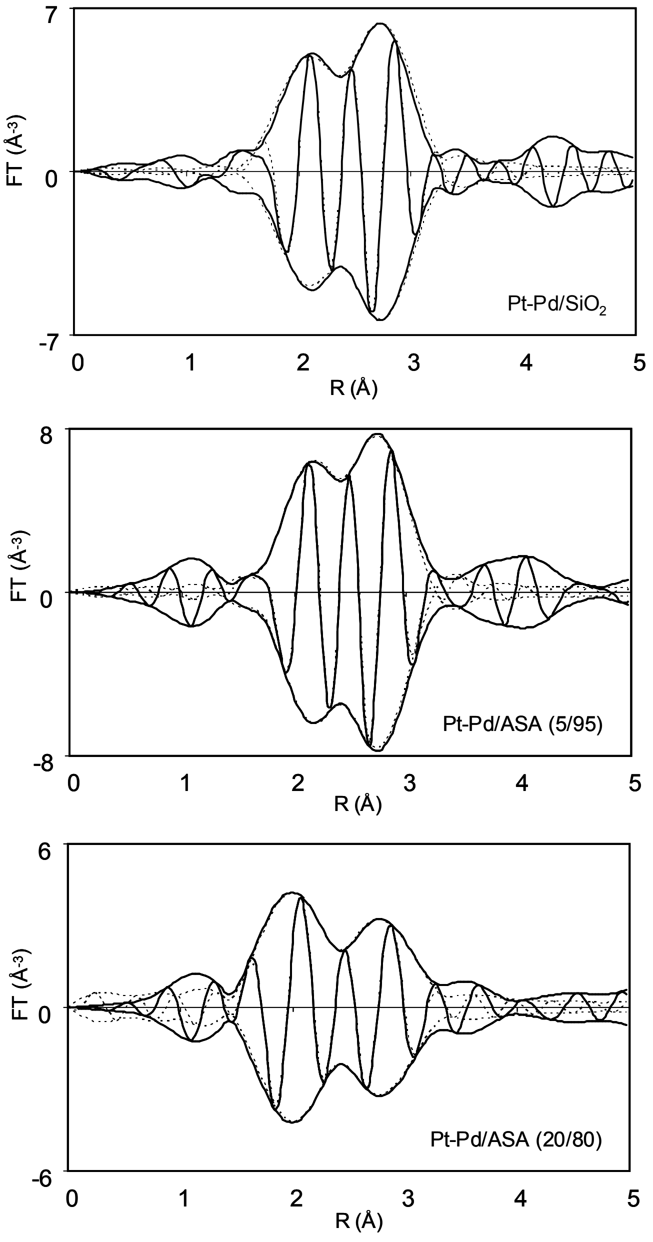

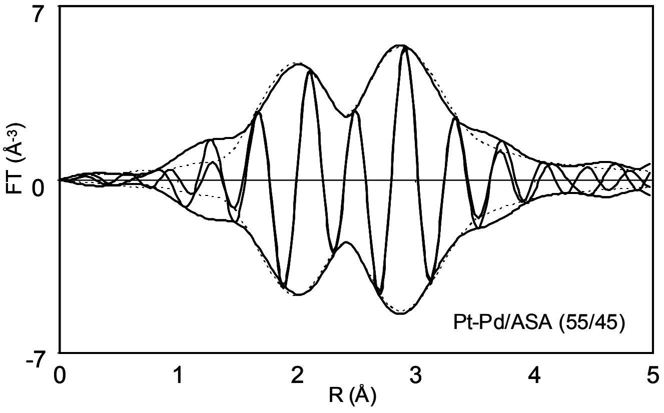

Figure 13. Fourier transforms (k^2 –weighted, Δk 2.8-11 $Å^{-1}$) of Pt-Pd/ASAs and Pt-Pd/SiO_2 (solid lines) at the Pt L_{III} edge (11564 eV). The Pt-Pt and Pt-Pd fitted contributions (dotted lines) after in situ H_2 reduction at 588 K are also included.

The shapes of the Fourier transforms of the bimetallic Pt-Pd samples (Figure 13) differ significantly from those of the monometallic Pt catalysts (see Figure 8). Two peaks are clearly separated between 2 and 3 Å. The presence of Pd as an additional scatterer in the Pt-Pd catalysts led to a very strong intensity increase of the first metallic coordination shell contribution attributed to Pt-Pd and a little shift of the main maximum (Pt-Pt) to higher R-values [33-36]. It was proposed that the shortening of the Pt-Pd bond distance results from the formation of $Pt^{x\delta+}$ - $xPd^{\delta-}$ ionic bonds [33, 37]. Nevertheless, the peak spacings do not necessarily represent the real difference between the Pt-Pd and the Pt-Pt bond distances due to phase interference effects on the Fourier transformed radial structure function of the two shell model of Pt-Pt and Pt-Pd [35].

The transformation of the Pt structure in bimetallic Pt-Pd and with varying support composition was visible from the normalized X-ray absorption near edge structure (XANES) spectra at the Pt L_{III} edge in Figure 14 and Figure 15.

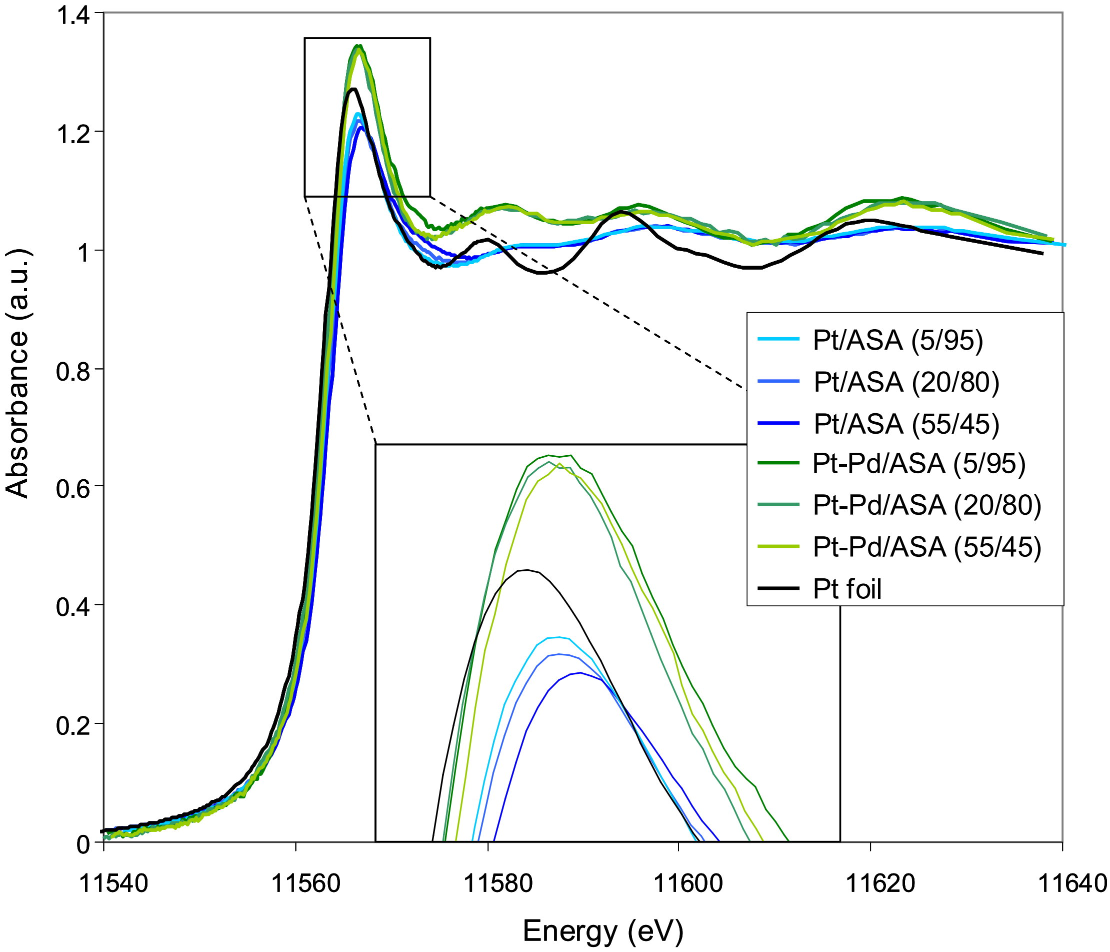

Figure 14. Normalized XANES spectra at the Pt L_{III} edge in He at 588 K of Pt foil, Pt/ASAs and Pd-Pd/ASAs after H_2 reduction at 588K.

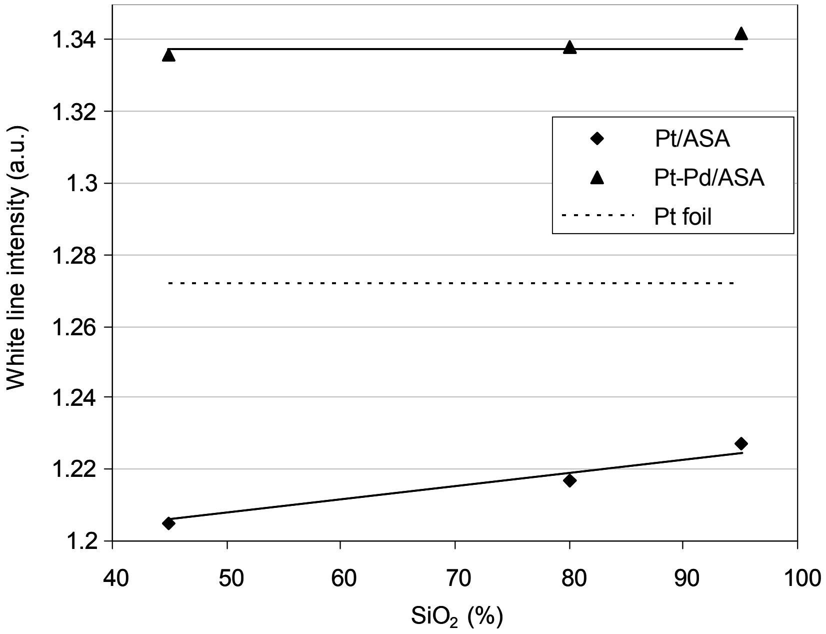

Figure 15. White line intensity as a function of the support silica content of the Pt/ASAs and the Pt-Pd/ASAs.

The intensity of the peak above the L_{III} edge in the XANES of the Pt/ASA catalysts varied for the different ASA carriers. This decrease in the intensity of the peak above the X-Ray absorption edge indicated increasing changes in the electron density of the particles with increasing electronegativity of the support. As the particles on the ASA support are small and of similar size, as confirmed by the analysis of the EXAFS and TEM (Table 5), particle size effects as reasons for the variations in the XANES are excluded [38]. It needs to be mentioned that for all Pt particles on the ASA support, the peak intensity above the absorption edge was smaller compared to the XANES of a Pt foil. This could indicate a higher overall electron density on the metal nanoclusters compared to the bulk material or more probable a particle size effect. Alternatively, residual hydrogen remaining on the surface after the reduction could lead to a smaller intensity, but the difference spectra between the XANES of the supported particles and of the Pt foil (data not shown) confirmed the successful removal of H_2 before the experiments. Additionally, Ichikuni et al. [39] observed that the effect of hydrogen on the XANES of small platinum particles (< 1.5 nm) is small.

The Whiteline intensity in the XANES of the Pt-Pd bimetallic nanoparticles at the Pt L_{III} edge increased as shown in Figure 14 and Figure 15 compared to the monometallic Pt catalysts implying an increase of the electron deficiency of the Pt atom d band. Since both $2p_{3/2}$ to $5d_{3/2}$ and $2p_{3/2}$ to $5d_{5/2}$ electronic transitions are allowed at the Pt L_{III} edge, the hole density in the $5d_{5/2}$ and $5d_{3/2}$ state becomes proportional to the Whiteline intensity, which is more sensitive to the change of the electronic structure than that at the Pd K edge. The increase of the Whiteline intensity in the XANES of the Pt-Pd particles suggests a lower electron density resulting from the formation of Pt-Pd bimetallic alloys [40].

The Fourier transforms of the EXAFS at the Pd K edge of all silica containing Pt-Pd catalysts are presented in Figure 16.

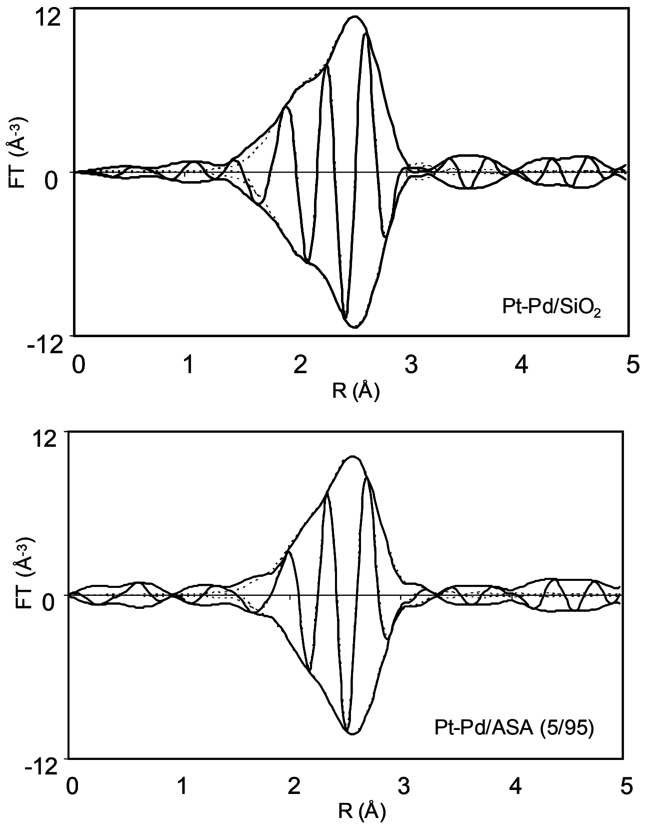

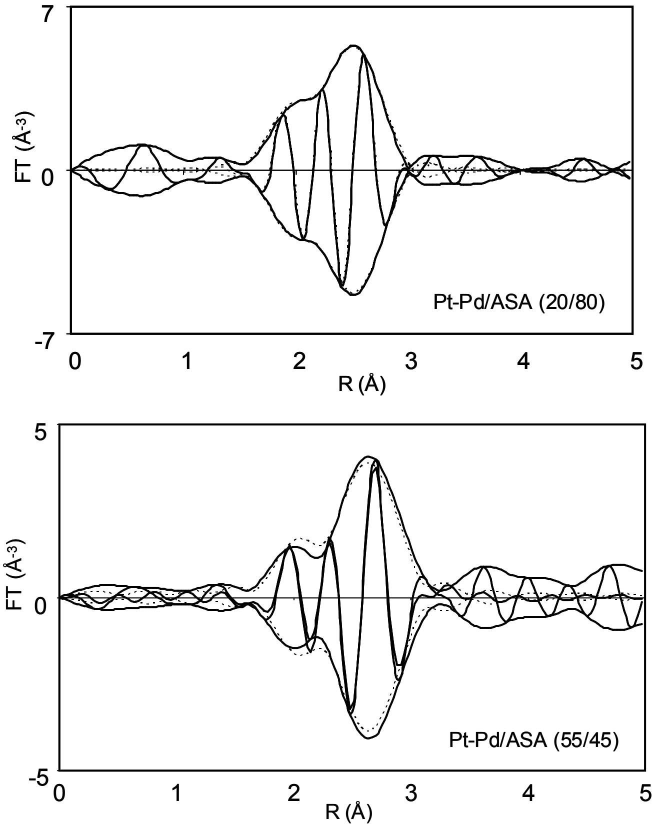

Figure 16. Fourier transforms (k^2 –weighted, Δk 2.8-13 Å^{-1}) of Pt-Pd/ASAs and Pt-Pd/SiO$_2$ (solid lines) at the Pd K edge (24365 eV). The Pd-Pd and Pd-Pt fitted contributions (dotted lines) after in situ H_2 reduction at 588 K are also included.

In the Fourier transforms resulting from the EXAFS at the Pd K edge of the bimetallic Pt-Pd samples (Figure 13) two peaks could be observed between 2.0 and 2.7 Å. In contrast to the Fourier transforms at the Pt L_{III} edge the Pd-Pd and the Pd-Pt contributions were not that clearly separated. The first metallic coordination shell contribution at around 2.0 Å was smaller then the second peak at 2.5-2.7 Å. This observation was previously reported before for Pt-Pd alloys by Toshima et al. and Rades et al. [36, 41].

Figure 17 displays the IR spectra of adsorbed CO at 0.5 mbar and 40°C on the hydrogen activated oxide supported Pt-Pd catalysts. Spectra after evacuation for 15 min at 10^{-6} mbar are also presented.

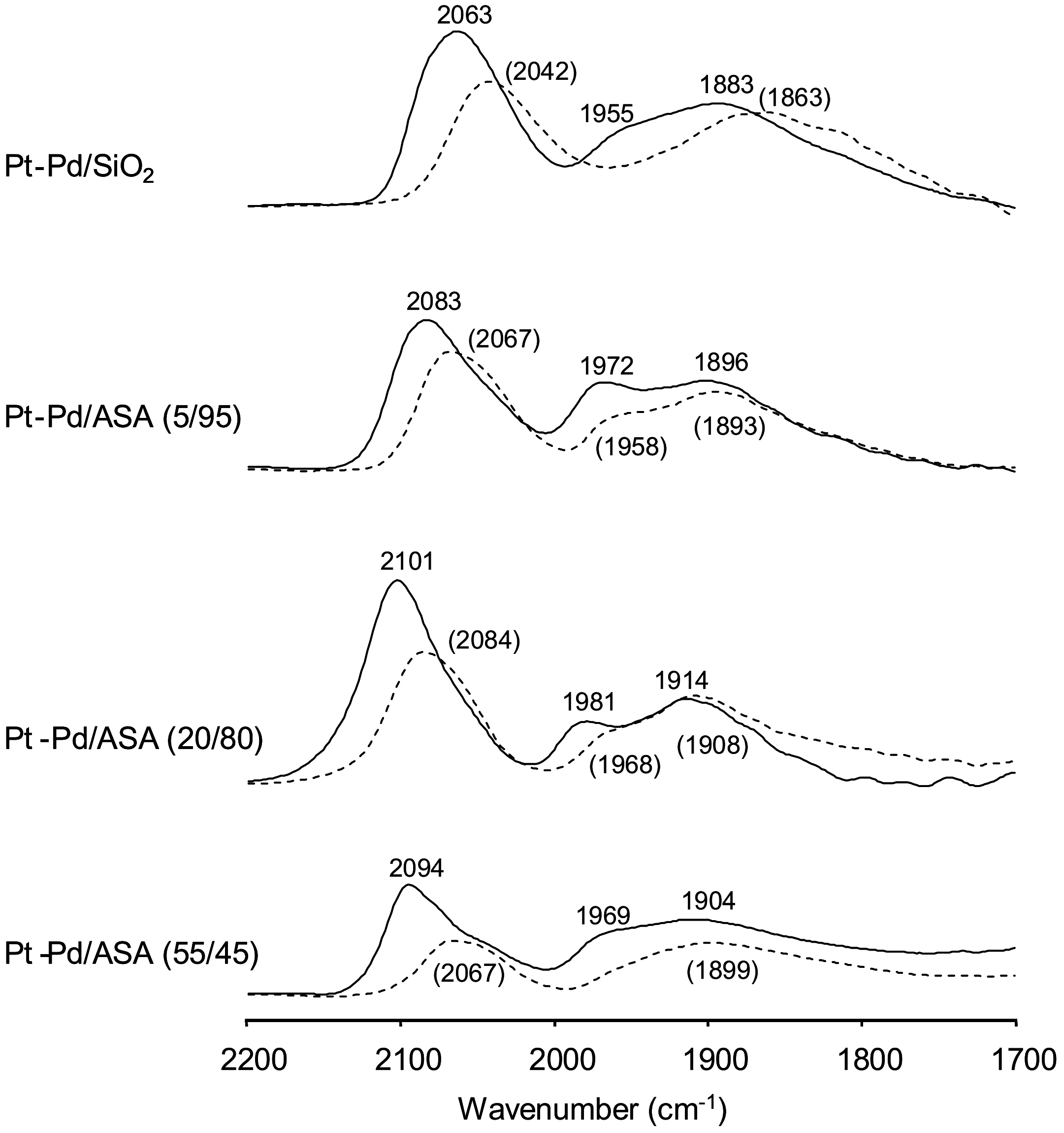

Figure 17. Infrared spectroscopy study of CO adsorbed on SiO$_2$ and ASA supported Pt-Pd catalysts at T = 40 °C, $p_{(CO)} = 5 \cdot 10^{-1}$ mbar (continuous lines). Spectra recorded after evacuation for 15 min are also included (dashed lines, band values in brackets).

It is known from the literature that CO-Pd bridge bonding leads to bands below 2000 cm^{-1} and that the peaks visible above 2000 cm^{-1} originate from CO linearly adsorbed on Pt and Pd [30, 32]. Low frequency peaks at 1880 – 1920 cm^{-1} are assigned to isolated Pd$_2$-CO complexes and the peaks at higher wavenumbers between 1950 and 1990 cm^{-1} stem from dimeric [Pd$_2$-CO]$_2$ species.

In the present study linear CO adsorption at 0.5 mbar led to the bands at 2063, 2083, 2101 and 2094 cm^{-1} for Pt-Pd/SiO$_2$, Pt-Pd/ASA (5/95), Pt-Pd/ASA (20/80) and Pt-Pd/ASA (55/45), respectively. In the same catalyst order isolated Pd$_2$-CO complexes resulted in the peaks at 1955, 1972, 1981 and 1969 cm^{-1}, whereas the dimeric [Pd$_2$-CO]$_2$ species led to the bands at 1883, 1896, 1914 and 1904 cm^{-1}.

The bands of linear CO bands on Pt overlap those on Pd, but the Pd-CO bond is extremely weak compared to Pt-CO [30]. Therefore, the band intensity of linear Pt-CO bonding hardly decreased upon evacuation at 10^{-6} mbar for 15 minutes for the monometallic Pt catalysts (see Figure 10). In order to confirm the weak linear Pd-CO bonding a test CO adsorption IR spectroscopy experiment was carried out on a Pd/ASA sample. Indeed it was found that the same stepwise CO adsorption desorption treatment as described before led to a total disappearance of linear adsorbed CO on Pd. In consequence, the decrease of the band intensity of CO linearly adsorbed on Pt-Pd upon evacuation could be assigned to the disappearance of weak linear Pd-CO bonds. The observed shift to lower wavenumbers (2042, 2067, 2084, and 2067 cm^{-1} for Pt-Pd/SiO$_2$, Pt-Pd/ASA (5/95), Pt-Pd/ASA (20/80) and Pt-Pd/ASA (55/45), respectively) could be due to a decrease of linear CO surface coverage [31].

The higher frequency peak in the bridged CO region (1955-1981 cm^{-1}) is more pronounced in Pt-Pd/ASA (5/95) and Pt-Pd/ASA (20/80) compared to Pt-Pd/SiO$_2$ and Pt-Pd/ASA (55/45). Dimeric [Pd$_2$-CO]$_2$ complexes can be only present when there are at least four adjacent Pd atoms at the metal surface. Therefore, Pt-Pd/ASA (5/95) and Pt-Pd/ASA (20/80) must be especially surface enriched with Pd. It was observed by TEM before that these two catalysts reveal also bigger average noble metal clusters (1.6 and 1.8 nm) compared to Pt-Pd/SiO$_2$ and Pt-Pd/ASA (55/45) (both 1.4nm, see Figure 12).

Upon evacuation at 10^{-6} mbar for 15 min mainly the higher frequency peak in the bridged CO region decreased or even disappeared with Pt-Pd/SiO$_2$ and Pt-Pd/ASA (55/45). The low frequency band (1883-1914 cm^{-1}) remained almost unchanged, which is probably due to the simultaneous conversion of [Pd$_2$-CO]$_2$ to isolated Pd$_2$-CO and CO desorption.

In order to compare the CO adsorption properties of the oxide supported monometallic Pt clusters with the bimetallic Pt-Pd particles the normalized integrated peak areas of linearly and bridged adsorbed CO at 0.5 mbar and after evacuation for 15 minutes at $5 \cdot 10^{-6}$ mbar are summarized in Table 6.

Table 6. Summary of the weight normalized integrated peak areas of linearly and bridged adsorbed CO on the oxide supported Pt and Pt-Pd catalysts at 0.5 mbar and after evacuation for 15 minutes $5 \cdot 10^{-6}$ mbar.

Catalyst	Normalized peak area of linearly adsorbed CO (2060-2110 cm^{-1})	Normalized peak area of bridged adsorbed CO (1840-1990 cm^{-1})	Ratio of linearly to bridged adsorbed CO
Pt/SiO_2	2623 (2598)	127 (101)	20.7 (23.0)
Pt/ASA (5/95)	2564 (2547)	62 (60)	41.4 (42.6)
Pt/ASA (20/80)	1434 (1418)	36 (32)	39.8 (45.0)
Pt/ASA (55/45)	1063 (1056)	68 (41)	15.6 (26.1)
Pt/Al_2O_3	1006 (980)	29 (19)	34.7 (47.9)
Pt-Pd/ SiO_2	623 (393)	608 (566)	1.0 (0.7)
Pt-Pd/ASA (5/95)	508 (410)	606 (545)	0.8 (0.8)
Pt-Pd/ASA (20/80)	578 (426)	540 (495)	1.1 (0.9)
Pt-Pd/ASA (55/45)	331 (168)	348 (285)	0.9 (0.6)

Table 6 clearly shows that Pt on the surface leads to strong CO adsorption as the normalized peak area of linearly adsorbed CO almost did not change after evacuation for 15 minutes. The presence of a large fraction of Pd surface atoms in the Pt-Pd catalysts is apparent from the formation of a large fraction of bridged adsorbed CO on Pd and the decrease of the normalized peak area of linearly adsorbed CO upon evacuation due to the desorption of weakly bonded linear Pd-CO species. It should be noted that the molar extinction coefficient for bridged bonded CO species is two to three times lower than that of the linear species [42, 43].

The normalized peak area of linearly adsorbed CO upon evacuation in Pt-Pd can be assigned to linear Pt-CO. The smaller values of this area compared to monometallic Pt is evident due to the bigger Pt-Pd cluster sizes (1.4-1.8 nm vs. 0.8-1.1 nm) and the lower Pt metal concentration (0.3 wt % vs. 0.8 wt % equal to a molar ratio of Pt to Pd of 1/3).

4 Discussion

4.1 Domains in amorphous silica alumina and their implications on the acid site distribution

Conceptually, the ASA material may have three domains, i.e., silica, alumina and a mixed oxide phase, in which the aluminum cations substitute silicon cations in tetrahedral positions. The silica parts of ASA support are relatively uniform terminating with hydroxyl groups that are at best mildly acidic. In addition to the hydroxyl groups, the alumina domains exhibit also Lewis acid sites resulting from coordinatively unsaturated aluminum cations in octahedral and tetrahedral position of alumina. In the mixed oxide phase (i.e., the aluminosilicate phase) also Brønsted acid sites are formed by the isomorphous substitution of Si^{4+} by Al^{3+} ions. This leads to a negative charge on the aluminum-oxygen tetrahedron, requiring neutralization by cations. The relative fraction of the three phases depends on the chemical composition and the preparation procedure of the silica alumina material.

As the material is amorphous, the separation into the domains has to be done via speciation of aluminum cations using ^{27}Al MAS NMR. In the first step, the aluminum species of the alumina phase are qualitatively and quantitatively characterized. In transition aluminas the aluminum cations occur in tetrahedral and octahedral coordination with oxygen. Within the restrictions imposed by the spinel lattice and the Al_2O_3 stoichiometry, the fraction of aluminum in tetrahedral coordination is between 25 to 37 %. In the present case, quantitative 1D ^{27}Al MAS NMR showed that four-coordinated (tetrahedral) aluminum accounted for 30 % of the total aluminum cations. The rest is assigned to six-fold coordinated (octahedral) aluminum cations. Treatment with ammonia does not transform octahedrally coordinated aluminum (O-Al) atoms into tetrahedrally coordinated (T-Al). Thus, the alumina phase does not contain a significant fraction of cations that can be reorganized by such treatment. Assuming that the alumina preserves the ratio of T-Al to O-Al, this allows determining the relative fraction of the alumina domains if all the other aluminum is reinserted into the mixed silica-alumina phase. In consequence, the aluminum in octahedral positions that can be reinserted and the pentacoordinated Al constitute the aluminum that is associated with the silica-alumina phase. Tetrahedral aluminum in the silica-alumina phase is determined by the difference between the total concentration of the tetrahedral aluminum and 3/7 of the concentration of the octahedral aluminum that cannot be reinserted by the ammonia treatment.

The lower the aluminum concentration in the ASAs, the lower is the probability of formation of alumina domains. In parallel, insertion of alumina tetrahedra separated and surrounded by four silica tetrahedra is promoted (aluminosilicate phase). Using the chemical shift of four-fold coordinated aluminum in the ^{27}Al MAS NMR spectra, it is concluded that most of the tetrahedral aluminum does not interact with neighboring Al atoms at about 20 % concentration of Al_2O_3 in ASA. Note that in the silica-alumina phase the signal appears at 51 ppm, compared with the chemical shift of T-Al in pure alumina at 67 ppm. The octahedrally coordinated aluminum in ASA (20/80) can be almost completely converted to tetrahedral aluminum upon exposure to ammonia. Omegna et al. demonstrated that these aluminum nuclei must be present in the alumino-silicate phase, so that they can be reintegrated into the tetrahedral coordination [16]. In contrast, aluminum species, which are not affected by this treatment, form a separate alumina phase. Therefore, this approach allows differentiating between alumino-silicate phases and pure alumina phases. Consequently, we conclude that in ASA (20/80) only a very small fraction of an alumina phase exists. Note that this contrasts strongly with results for ASA (55/45) samples. In that case only a small fraction of the octahedrally coordinated aluminum is converted to tetrahedrally coordinated aluminum after ammonia treatment. With ASA (5/95) changes and incorporation in the O-Al were observed as well.

Several possible structures have been suggested for octahedrally coordinated aluminum species in zeolites that can be transformed into tetrahedrally coordinated ones. These suggestions include coordination to water molecules after partial hydrolysis of the framework [44] and a hydronium ion to a framework Al atom with a distorted tetrahedral coordination [15, 17]. In the present case, the second scenario is rather improbable, as a considerable concentration of flexible aluminum and no indications for the presence of hydronium ions were found. Therefore, we conclude that partial hydrolysis in silica-alumina phases plays a major role in the formation of flexible aluminum. Due to the amorphous structure of ASA it is not surprising that the concentration of flexible aluminum in this material exceeds that in zeolites [16].

Thus, the results show unequivocally that in the precipitation process a perfect amorphous mixture of alumina and silica tetrahedra on the atomic scale is not formed [45]. Using the algorithm described above the contribution of alumina and silica-alumina domains can be estimated (see Table 7).

Table 7. Distribution of the aluminum species in the Pt/ASA catalysts (in $mmol \cdot g^{-1}$, values in brackets in %).

	Alumina patches		Amorphous silica-alumina phase			
Catalyst	O-Al	T-Al	P-Al	O-Al	T-Al	Total
Pt/ASA (55/45)	4.84 (47)	2.25 (22)	2.66 (26)	0.29 (3)	0.35 (3)	10.39
Pt/ASA (20/80)	0.44 (11)	0.20 (5)	0.96 (24)	0.76 (19)	1.64 (41)	4.00
Pt/ASA (5/95)	0.11 (13)	0.05 (6)	0.00 (0)	0.15 (18)	0.53 (63)	0.84

The MQMAS spectra show that pentavalent Al is present in Pt/ASA (20/80) and Pt/ASA (55/45). While the observation of pentavalent Al has been discussed in various publications [20-25], most studies are focused on proving or disproving its existence. Probably, the most detailed discussion has been given by De Witte et al. suggesting that pentacoordinated aluminum is present as a highly disordered interface that connects an alumina domain with a silica or silica-alumina domain [23]. Our measurements here support this model. The concentration of pentavalent aluminum is only significant in aluminum rich materials and it does not vary with ammonia treatment. This suggests that the species is affiliated with the alumina phase. As it is an interface phenomenon, the concentration of the species depends upon the size and the concentration of the alumina domains.

The silica-alumina domains contain two types of aluminum cations: (i) surface-exposed O-Al with flexible coordination environment and (ii) T-Al potentially generating

Brønsted acid sites. For all investigated ASA samples the concentration of Brønsted acid sites determined by IR spectroscopy of adsorbed pyridine was much lower than the concentration of T-Al. This suggests that a major fraction of the octahedrally coordinated aluminum in the ASA phase is used to compensate the negative charges of the oxygen aluminum tetrahedra in the silica-alumina phase. The concentration of tetrahedrally coordinated alumina in silica-alumina phases (T-Al_{SA}) can be correlated with the concentration of Brønsted acid sites and the concentration of Lewis acid sited is increased with higher alumina content in the support [18].

4.2 Characterization of the Pt phase in the ASA supported platinum catalysts

For very small Pt nanoclusters, the coordinatively unsaturated atoms from edges, corners and surfaces represent a significant fraction of the Pt atoms and consequently their average coordination number is smaller than in the bulk metal. TEM is needed to determine the size distribution of metal clusters [46]. Additionally, EXAFS analysis is used in order to study the very small metal particles in more detail. Pt-Pt coordination numbers were determined and detailed information about the Pt cluster morphology becomes available by additionally examining the Pt-O and Pt-Al contributions. Furthermore the conversion of platinum oxide to metallic platinum upon hydrogen reduction is clearly shown by the transformation of Pt-O to Pt-Pt contributions in the EXAFS Fourier transforms.

There is a very good correlation between metal particle sizes derived from TEM and EXAFS data. Thus, overall, the metal particles are well distributed and uniform in size for all alumina containing supports, providing a solid basis for evaluating the role of the support on the catalytic properties of Pt. Moreover, particle size effects as reasons for the differences of the White line intensities in the XANES analysis can be excluded [38]. In general, the intensity of the peak above the L_{III} edge can be related to the density of unoccupied d-states of Pt [47, 48]. An interaction with an electron withdrawing sorbate [49-51] and/or an electronegative support [52] will lead to polarization of the electrons in the metal and to a change (decrease) in the electron density in the Pt particles. For the Pt L_{III} edge, the transition from a $p_{3/2}$ ground-state to partially unoccupied orbitals with $5d_{5/2}$

character in the final state is observed. In addition, also the transition to final states with $5d_{3/2}$ character are allowed at the L_{III} edge, however these contributions could be excluded from the XANES measured at the L_{II} edge [53]. For Pt, the d-orbitals are close to the Fermi level and only partially occupied. Thus, during catalytic reactions on the Pt surface electrons from these orbitals are directly involved in the electronic interaction with the reactant molecules.

Thus, the changes in the intensity of the peak above the X-Ray absorption edge are attributed to the variations in the electron density of the Pt particles induced from the interaction with the acidic support. The direct proportionality between the intensity of the peak above the L_{III} edge and the composition of the ASA support (see Figure 15) indicates that the electron density of the Pt surface atoms decreases with increasing electronegativity of the support and that the most electron rich Pt particles are present on ASA (5/95), the support with the highest intermediate electronegativity.

According to the generally accepted Blyholder model [54], electrons are donated from CO through a sigma bond into the metal d-orbitals. Electron backdonation from filled metal d-orbitals into empty $2\pi^*$ orbitals of CO leads to a lower bond strength between C and O and consequently the IR absorption band shifts to lower wavenumbers compared to gas phase CO (2143 cm^{-1}). High electron densities in metals at binding energies close to the CO $2\pi^*$ orbital lead to an enhanced degree of backdonation and, thus, electron density distributions on metal surface atoms can be explored by CO adsorption onto metal surfaces. Strong CO coordination on all oxide supported Pt catalysts in this study is almost exclusively observed in linear position at 2060 – 2090 cm^{-1}, whereas (multiple) bridged bonded CO at 1840 – 1990 cm^{-1} is hardly observed [29-32]. As a low degree of electron backdonation by the metal inhibits the formation of bridged bonded CO [55-57], this result indicates the presence of very electron deficient Pt clusters on all present oxide carriers. The high strength of the linear Pt-CO bonds is apparent from the only marginal change of the absorption bands upon evacuation of the system. The little shift to lower wavenumbers during this treatment can be ascribed to a small decrease in the CO metal surface coverage. The position of the stretching frequency is not only determined by the electronic state of Pt, but also by the degree of CO coverage [31, 32]. EXAFS and TEM data show the small size and uniformity of the Pt clusters on all alumina containing supports. On the other hand the normalized IR peak area of linearly adsorbed CO varies strongly among the catalysts and decreases with increasing alumina content in the support. Apparently CO adsorption at 0.5 mbar does not lead to fully CO covered Pt clusters and, thus, the position of the stretching frequency can not be directly correlated to the electron deficiency of the clusters as observed in the XANES analysis. Nevertheless it is interesting to note that the Pt catalysts supported on the ASA catalysts lead to CO adsorption at higher wavenumbers compared to neutral Pt/SiO_2 and Pt/Al_2O_3, confirming metal-support interactions that are especially induced by the moderate acidic ASA supports [58].

4.3 Alloy formation in the oxide supported bimetallic Pt-Pd phase

The preparation of oxide supported Pt-Pd catalysts via incipient wetness impregnation with $Pt(NH_3)_4(NO_3)_2$ and $Pd(NO_3)_2 \cdot xH_2O$ yields somewhat bigger noble metal clusters compared to monometallic Pt with average diameters of 1.4-1.8 nm and a relatively large particle size distribution between 0.8 and 3.0 nm. This TEM analysis shows that noble metal clusters with varying size and probably with varying shape and composition are formed.

In the literature many authors suggest Pd segregation on the surface of Pt-Pd alloy particles using experimental and theoretical methods such as EXAFS [34, 35, 59-61], CO adsorption IR spectroscopy [32] and Monte Carlo simulation [60, 62-64]. This is frequently explained by a lower surface energy and a lower enthalpy of sublimation of Pd compared to Pt. Nevertheless also other models can be found suggesting uniform Pt-Pd mixtures [30, 36] or even surface enriched Pt with a Pd metal core [40]. Also in the present work Extended X-ray absorption fine structure analysis was applied to investigate the local structure of Pd and Pt in the oxide supported Pt-Pd catalysts. In contrast to the monometallic Pt with its large Pt-Pt contributions two peaks at around 2.0-2.1 and 2.8-2.9Å are clearly separated in Pt-Pd representing Pt-Pd and Pt-Pt bonds, respectively. The peak at around 2Å appears at a too low R and the contribution at 2.9Å at somewhat too large R in order to be assigned to a metal, as the closest packing of a typical Pt or Pd fcc packing would result in an R of 2.64 Å. Apparently, $Pt^{x\delta+}$ - $xPd^{\delta-}$ ionic bonds are formed leading to coulombic attraction and, thus, to the extraordinary small R value [33, 37]. The repulsion between $Pt^{\delta+}$ - $Pt^{\delta+}$ consequently results in larger R values.

XANES analysis at the Pt L_{III} edge confirmed the electron deficiency of Pt in the $Pt^{x\delta+}$ - $xPd^{\delta-}$ ionic bond as the white line intensity significantly increases when forming a bimetallic Pt-Pd alloy compared to monometallic Pt [40]. The support composition does not influence the white line intensity and, thus, the electronic state of the metal alloys. This can be explained by the superposing effect of the ionic bonds in the Pt-Pd alloy.

A separation of Pd-Pd and Pd-Pt contributions in the Fourier transforms of the EXAFS at the Pd K edge is not that obvious as in the analysis of the Pt L_{III} edge. As the molar ratio of Pd/Pt is 3/1 in the Pt-Pd catalysts, the large peak at R = 2.5-2.7 Å is assigned to metallic Pd-Pd bonds that are statistically much less affected by the $Pt^{x\delta+}$ - $xPd^{\delta-}$ ionic bond formation than the Pt-Pt bonds. Therefore no shift to higher R values is observed here. Nevertheless, also at the Pd K edge, the small contribution at around 2.0 Å originating from the Pd-Pt ionic bonding can be seen [36, 41].

Adsorption of CO on the supported Pt-Pd particles gives insight in the surface properties of the Pt-Pd alloy. In contrast to the monometallic Pt catalyst, a large fraction of CO adsorbs in bridged position, which is assigned to isolated Pd_2-CO species (1883-1914cm^{-1}) and dimeric $[Pd_2\text{-}CO]_2$ complexes (1955-1981cm^{-1}) [30, 32]. The latter species can be only formed when there are at least four neighbouring Pd atoms on the metal alloy surface suggesting a Pd enriched alloy surface, especially on the somewhat bigger Pt-Pd alloy particles of Pt-Pd/ASA (5/95) and Pt-Pd/ASA (20/80). This result does not surprise as the molar ratio of Pd/Pt is 3/1 in all the explored bimetallic catalysts. Nevertheless also Pt atoms must be present on the surface as the evacuation at 10^{-6} mbar for 15 minutes does not lead to a total disappearance of linear CO-metal bonding, which would have been expected on a particle with only Pd atoms on a surface [32]. It has been clearly shown by CO adsorption on oxide supported monometallic Pt that linearly adsorbed CO on Pt hardly desorbs during the evacuation treatment.

In summary, the present ASA and SiO_2 supported Pt-Pd catalysts with a molar Pd/Pt ratio of 3/1 consist of metal alloys with a large size distribution of 0.8 – 3.0 nm. The clusters are surface enriched with Pd, but also Pt atoms must be present on the alloy surface as visualized in Figure 18. Besides metallic Pd-Pd and Pt-Pt bonds ionic $Pt^{x\delta+}$ - $xPd^{\delta-}$ are present, yielding very electron deficient Pt atoms.

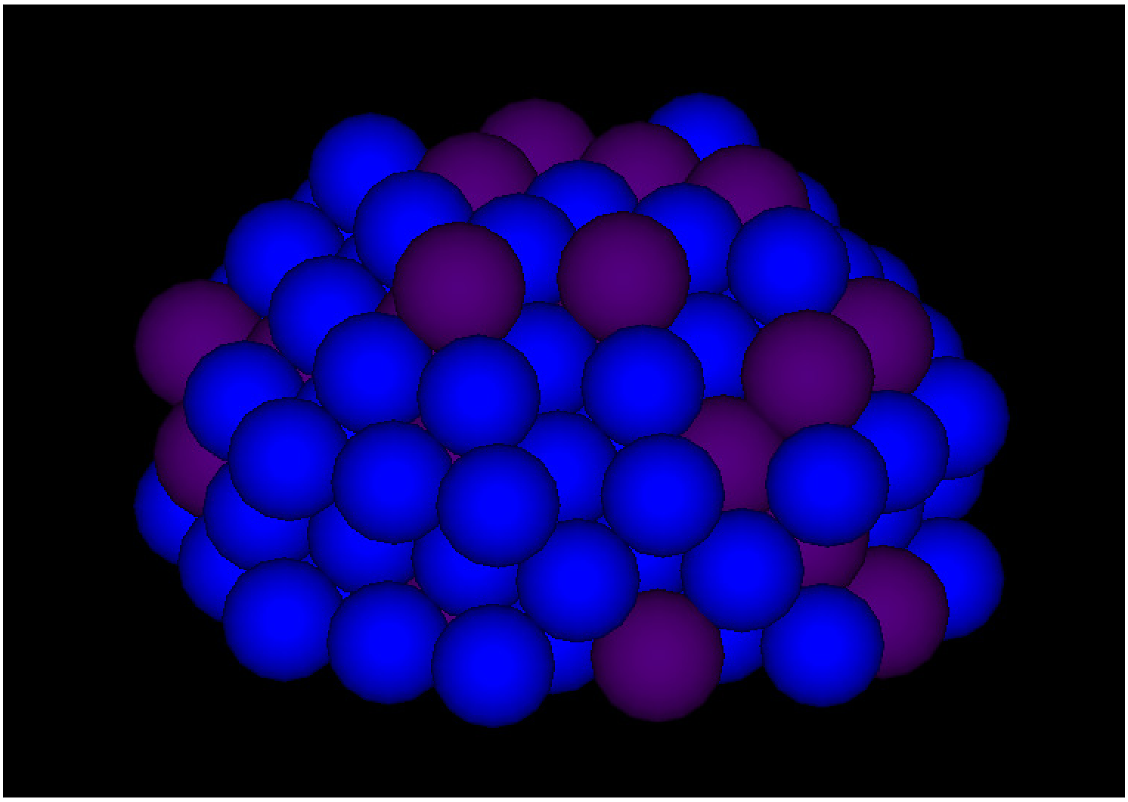

Figure 18. Model of a Pt-Pd cluster (Ø = 1.5 nm) with a Pt (purple spheres) to Pd (blue spheres) ratio of 1/3.

5 Conclusions

Amorphous silica-aluminas as support for a series of Pt and Pt-Pd catalysts were characterized by a variety of experimental techniques, focusing on the presence of different phases and domains in the amorphous material and the various types of acid sites. Moreover the bimetallic Pt-Pd phase was compared with monometallic Pt.

ASA supports can be synthesized with desired concentrations of silica, alumina, and aluminosilicate phases. Every phase contributes with a different type of acidity. Weak and strong Lewis acid sites are originated in the alumina clusters, while Brønsted acid sites are generated in the aluminosilicate phase.

The Pt particles anchored by wet impregnation were small and uniform, i.e., between 0.7 and 0.9 nm on all aluminum containing supports.

The present ASA and SiO_2 supported Pt-Pd catalysts with a molar Pd/Pt ratio of 3/1 consist of metal alloys with a large size distribution of 0.8 – 3.0 nm and mean particle diameters of 1.4 – 1.8 nm. The clusters are surface enriched with Pd, but also Pt atoms must be present on the alloy surface. Besides metallic Pd-Pd and Pt-Pt bonds ionic $Pt^{x\delta+}$ - $xPd^{\delta-}$ are present, yielding very electron deficient Pt atoms.

Acknowledgments

Financial support of S.R.T.C. Amsterdam is gratefully acknowledged. Martin Neukamm and Xaver Hecht are thanked for the AAS and BET measurements, respectively. The XAFS experiments were carried out at the stations C and X1 at HASYLAB, DESY, Hamburg, Germany and supported by the TMR-Contract ERBFMGECT950059 of the European Community.

6 References

1. J. Scherzer and A. J. Gruia, *Hydrocracking Science and Technology, Chapter 12*. 1996, New York. 215.
2. J. Ward, Fuel Process. Technol., 1993. 35 55.
3. W. R. A. M. Robinson, J. A. R. van Veen, V. H. J. de Beer and R. A. van Santen, Fuel Process. Technol., 1999. 61 61.
4. J. A. R. van Veen and S. T. Sie, Fuel Process. Technol., 1999. 61 1.
5. A. P. M. Kentgens, Geoderma, 1997. 80 271.
6. J. Klinowski, Progress in NMR Spectroscopy, 1984. 16 237.
7. D. D. Laws, H. M. L. Bitter and A. Jerschow, Angew. Chem. Int. Ed., 2002. 41 3096.
8. J. P. Amoureux, C. Fernandez and S. Steuernagel, J. Magn. Reson. Ser. A, 1996. 123 116.
9. R. Ernst, G. Bodenhausen and A. Wokaun, *Principles of Nuclear Magnetic Resonance in One and Two Dimensions*. 1987, New York: Oxford University Press.
10. J. A. van Bokhoven, A. L. Roest, D. C. Koningsberger, J. T. Miller, G. H. Nachtegaal and A. P. M. Kentgens, J. Phys. Chem. B, 2000. 104 6743.
11. C. A. Emeis, J. Catal., 1993. 141(2) 347.
12. K. V. Klementiev, *VIPER and XANDA for Windows, freeware*.
13. A. L. Ankudinov, B. Ravel, J. J. Rehr and S. D. Conradson, Phys. Rev. B, 1998. 58 7565.
14. A. L. Ankudinov and J. J. Rehr, Phys. Rev. B, 2000. 62 2437.
15. E. Bourgeat-Lami, P. Massiani, F. Di Renzo, P. Espiau and F. Fajula, Appl. Catal. A-Gen., 1991. 72 139.
16. A. Omegna, J. A. van Bokhoven and R. Prins, J. Phys. Chem. B, 2003. 107 8854.
17. J. A. van Bokhoven, D. C. Koningsberger, P. Kunkeler, H. van Bekkum and A. P. M. Kentgens, J. Am. Chem. Soc., 2000. 122 12842.
18. M. F. Williams, B. Fonfé, C. Sievers, A. Abraham, J. A. van Bokhoven, A. Jentys, J. A. R. van Veen and J. A. Lercher, J. Catal., 2007. 251(2) 485.

19. M. H. Lee, C. F. Cheng, V. Heine, and J. Klinowski, Chem. Phys. Lett., 1997. 265 673.
20. S. M. C. Menezes, V. L. Camorim, Y. L. Lam, R. A. S. San Gil, A. Bailly and J. P. Amoureux, Appl. Catal. A - Gen., 2001. 207 367.
21. M. P. J. Peeters and A. P. M. Kentgens, Solid State Nucl. Magn. Reson., 1997. 9 203.
22. G. Crepeau, V. Montouillout, A. Vimont, L. Mariey, T. Cseri and F. Mauge, J. Phys. Chem. B, 2006. 110 15172.
23. B. M. De Witte, P. J. Grobet and J. B. Uytterhoeven, J. Phys. Chem., 1995. 99 6961.
24. J. P. Gilson, G. C. Edwards, A. W. Peters, K. Rajagopalan, R. F. Wormsbecher, T. G. Roberie and M. P. Shatlock, J. Chem. Soc.-Chem. Commun., 1987 91.
25. G. J. Ray and A. Samoson, Zeolites, 1993. 13 410.
26. H. Koller, E. L. Meijer and R. A. van Santen, Solid State Nucl. Magn. Reson., 1997. 9 165.
27. D. Freude, T. Fröhlich, H. Pfeifer and G. Scheeler. in *Second Workshop on the Adsorption of Hydrocarbons in Microporous Sorbents*. 1982. Eberswalde, GDR.
28. *Cerius 2 program suite*, Accelrys Inc, 2001.
29. C. S. Chen, J. H. Lin, and H. W. Chen, Appl. Catal. A-Gen., 2006. 298 161.
30. C. M. Grill, M. L. McLaughlin, J. M. Stevenson and R. D. Gonzalez, J. Catal., 1981. 69(2) 454.
31. M. Primet, L. C. De Menorval, F. J. and T. Ito, J. Chem. Soc., Faraday Trans. 1, 1985. 81 2867.
32. T. Rades, V. Y. Borovkov, V. B. Kazansky, M. Polisset-Thfoin and J. Fraissard, J. Phys. Chem., 1996. 100(40) 16238.
33. N. Matsubayashi, H. Yasuda, M. Imamura and Y. Yoshimura, Catal. Today, 1998. 45(1-4) 375.
34. T. Matsui, M. Harada, K. K. Bando, M. Toba and Y. Yoshimura, Appl. Catal. A-Gen., 2005. 290(1-2) 73.
35. A. Morlang, U. Neuhausen, K. V. Klementiev, F. W. Schutze, G. Miehe, H. Fuess and E. S. Lox, Appl. Catal. B-Env., 2005. 60(3-4) 191.

36. T. Rades, C. Pak, M. Polisset-Thfoin, R. Ryoo and J. Fraissard, Catal. Lett., 1994 91.
37. T. B. Lin, C. A. Jan and J. R. Chang, Ind. Eng. Chem. Res., 1995. 34 4284.
38. D. Bazin and J. J. Rehr, J. Phys. Chem. B, 2003. 107 12398.
39. N. Ichikuni and Y. Iwasawa, Catal. Letters, 1993. 20 87.
40. S. J. Cho and S. K. Kang, Catal. Today, 2004. 93-95 561.
41. N. Toshima, M. Harada, T. Yonezawa, K. Kushihashi and K. Asakura, J. Phys. Chem., 1991. 95 7448.
42. W. M. H. Sachtler, Catal. Rev. Sci. Eng., 1976. 14(2) 193.
43. Y. Soma-Noto and W. M. H. Sachtler, J. Appl. Phys. Suppl., 1974. 2 241.
44. G. L. Woolery, G. H. Kuehl, H. C. Timken, A. W. Chester and J. C. Vartuli, Zeolites, 1997. 19 288.
45. Y. Kato, K. Shimizu, N. Matsushita, T. Yoshida, H. Yoshida, A. Satsuma and T. Hattori, Phys. Chem. Chem. Phys., 2001. 3 1925.
46. K. Heinemann and F. Soria, Ultramicroscopy, 1986. 20 1.
47. A. L. Ankudinov and J. J. Rehr, J. Chem. Phys., 2001. 116 1911.
48. A. N. Mansour, J. W. Cook, and D. E. Sayers, J. Phys. Chem., 1984. 88 2330.
49. A. Jentys, L. Simon, and J. A. Lercher, J. Phys. Chem B., 2000. 104 9411.
50. T. Kubota, K. Asakura, and Y. Iwasawa, Catal. Lett., 1997. 46 141.
51. M. G. Samant and M. Boudart, J. Phys. Chem., 1991. 95 4070.
52. J. T. Miller, B. L. Mojet, D. E. Ramaker and D. C. Koningsberger, Catal. Today, 2000. 62 101.
53. D. E. Ramaker, B. L. Mojet, M. T. G. Oostenbrink, J. T. Miller and D. C. Koningsberger, Phys. Chem. Chem. Phys., 1999. 1 2293.
54. G. Blyholder, J. Phys. Chem., 1964. 68 2772.
55. J. E. Crowell, E. L. Garfunkel and G. A. Somorjai, 1982. 121 303.
56. L. L. Sheu, Z. Karpinski and W. M. H. Sachtler, J. Phys. Chem., 1989. 93 4890.
57. R. A. Van Santen, J. Chem. Soc., Faraday Trans. 1, 1987. 83 1915.
58. M. F. Williams, B. Fonfé, C. Woltz, A. Jentys, J. A. R. van Veen and J. A. Lercher, J. Catal., 2007. 251(2) 497.

59. T. Fujikawa, K. Tsuji, H. Mizuguchi, H. Godo, K. Idei and K. Usui, Catal. Lett. 1999. 63 27.
60. P. L. Hansen, A. M. Molenbroek and A. V. Ruban, J. Phys. Chem. B, 1997. 101(10) 1861.
61. N. Toshima, M. Harada, T. Yonezawa, K. Kushihashi and K. Asakura, J. Phys. Chem., 1991. 95(19) 7448.
62. H. Deng, W. Hu, X. Shu, L. Zhao and B. Zhang, Surface Science, 2002. 517(1-3) 177.
63. J. L. Rousset, A. J. Renouprez and A. M. Cadrot, Physical Review B, 1998. 58(4) 2150.
64. D. Cheng, S. Huang and W. Wang, Chem. Phys., 2006. 330(3) 423.

Chapter 3

Hydrogenation of tetralin by silica-alumina supported Pt catalysts I - Mechanistic aspects in the presence of sulfur and nitrogen containing poisons

A series of catalysts based on platinum nanoparticles supported on amorphous silica-alumina with varying concentrations of alumina (55, 20, and 5 wt. %) were investigated for tetralin hydrogenation in the presence of either quinoline and/or dibenzothiophene. Quinoline neutralizes the acid sites and competes with tetralin for the adsorption sites on platinum, while dibenzothiophene poisons selectively the metal sites. In both cases, the catalytic activity was significantly reduced, but to a far lower extent as when both poisons are present. The reaction pathways for hydrogenation in the presence of poisons are discussed and sites at the perimeter of the supported metal particles are identified to be crucial for the sustained catalytic activity.

1 Introduction

Stringent environmental and legislation standards for diesel fuels necessitate new catalytic systems and hydrotreating processes in the oil industry [1]. Supported noble metal catalysts such as Pt or Pd are well known for their high hydrogenation activity in deep hydrodearomatisation (HDA). Thus, hydrogenation is one of the best routes to reduce the concentration of aromatics and to supply fuel components with high cetane numbers. The reaction can be carried out at low temperatures and moderate hydrogen pressures. However, noble metals exhibit low resistance towards sulfur and nitrogen poisons usually present in feedstocks [2]. While sulfur poisoning has been widely studied over the last years the insight into the mechanism of nitrogen poisoning of noble metals deposited on acidic carriers under hydrotreating conditions is not well developed. This is especially important, because both poisons usually are found together in the relevant feedstocks and measures to increase the sulfur resistance of noble metal based catalysts have been reported [3].

In order to account for the beneficial effect of the carrier acidity on the catalyst performance it was proposed that the metal – sulfur bond strength is altered due to a support induced electron deficiency of the nanosized metal particles. As a result a significant higher turnover frequency of the hydrogenation reaction could be observed [4-8]. It has also been suggested that the enhanced sulfur poison tolerance is caused by the presence of hydrogenation sites at the metal particle acidic carrier interfacial region that could contribute to the overall rate of aromatic hydrogenation [9-17].

The purpose of this study is to explore the effect of quinoline and dibenzothiophene (DBT), as typical potential poisons, on the activity of a series of amorphous silica-alumina supported platinum catalysts with respect to the hydrogenation of tetralin (1,2,3,4-tetrahydronaphthalene). The synthesis and detailed characterization of these catalysts have been previously reported together with the catalytic activity with respect to tetralin hydrogenation in the absence of poisons [18, 19].

2 Experimental

2.1 Catalytic measurements

All chemicals used in the study were obtained from commercial suppliers and used as provided: Tetralin (Aldrich, > 99 % GC assay), hexadecane (Merck, > 99 % GC assay), n-tetradecane (Aldrich, > 99 % GC assay), *cis*- and *trans*-decalin (Aldrich, > 99 % GC assay) and hydrogen (Air Liquide > 99.999%).

The hydrogenation of tetralin was carried out in a set of 4 parallel trickle-bed reactors in continuous down-flow mode as depicted in Figure 1.

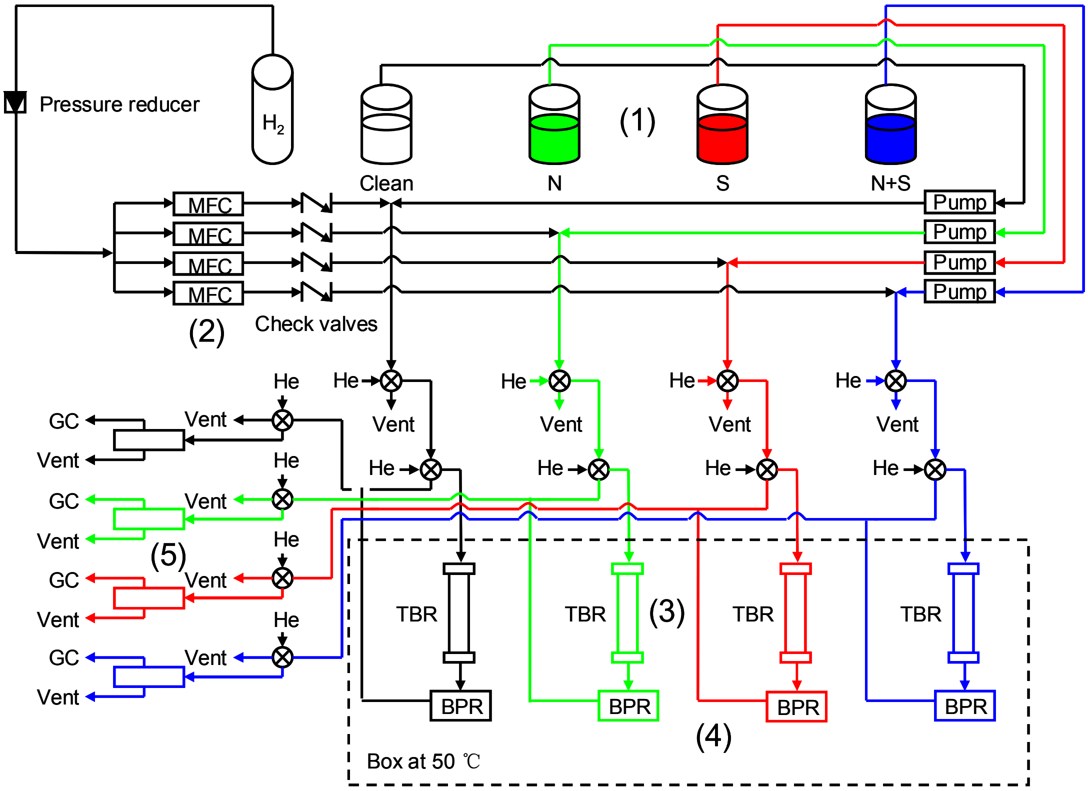

Figure 1. Simplified flow diagram of the continuous hydrogenation testing unit (1) 4 feed tanks (2) 4 mass flow controllers; (3) 4 trickle-bed reactors; (4) 4 back pressure regulators; (5) 4 gas-liquid separators.

The reactor was filled with catalyst (d = 300-600 µm) diluted with SiC (ratio = 0.01 – 0.25 g_{cat}/g_{SiC}) to ensure a homogeneous thermal distribution. To avoid entrance effects two inert layers (i.e., SiC and glass wool) were placed on the top and the bottom of the catalyst bed (Figure 2).

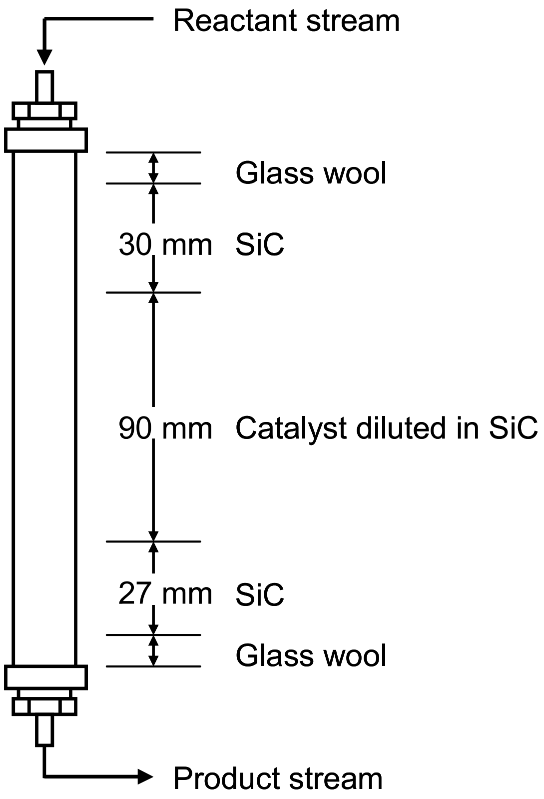

Figure 2. Reactor filling

The liquid feed and hydrogen were dosed by an HPLC pump (Gilson model 5cc) and a Bronkhorst EL-FLOW mass flow controller, respectively.

During the experiment, a number of samples were collected for off-line GC analysis. The analysis was carried out with a Gas Chromatograph (HP 6890) equipped with an Agilent DB-1701 column. N-tetradecane (11.5 wt. % in the feed) was used as the internal standard. Prior to the activity tests, the catalysts were reduced in hydrogen (p = 1 bar, flow rate 30 $cm^3 \cdot min^{-1}$, 2 h at 588 K). In order to preserve the high metal dispersion a very slow heating rate of 0.41 K·min^{-1} was applied to reach the final temperature for the reduction.

A feed of 20 wt. % tetralin in a mixture with n-hexadecane and n-tetradecane was poisoned with quinoline (20 or 400 ppmw N) and/or dibenzothiophene (100 ppmw S). These feeds reflect typical concentrations in diesel fractions. Three parallel supply lines and reactors were used for N (400 ppmw N), S (100 ppmw S) and N+S (20 ppmw N and 100 ppmw S) mixed poison feed. The liquid feeds and hydrogen were mixed before entering the reactors. The experimental conversion values were not altered by varying the amount of catalyst and the total flow rate, maintaining constant the space velocity (i.e., negligible external transport limitations). The catalytic behavior was found to be independent of the particle diameter (i.e., no intraparticle gradients). The performance of the reactors and the accuracy of the analytical method were analyzed by feeding the organic solution to the reactors filled with SiC, operating at 463 K at 50 bar hydrogen pressure. No formation of unexpected products was detected with a recovery percentage of > 99 % tetralin. The chosen solvents hexadecane and n-tetradecane did not react under the applied reaction conditions.

If not noted otherwise the catalyst testing was carried out at 453 K and 50 bar hydrogen pressure with a weight hourly space velocity (WHSV) range comprised between 4.9 and 26.3 h^{-1} for the N-poison feed, and between 1.0 and 21.6 h^{-1} for the S- or N+S-poison feed. A change of the WHSV was achieved by a change in the amount of catalyst and/or the flow rate (a constant molar ratio of H_2 to tetralin of 20.5 was maintained). In order to determine the apparent energy of activation ($Ea_{(exp)}$) and to compare the catalytic activity, the hydrogenation experiments were carried out at 433, 443, 453 and 463 K and at constant WHSV of 26 h^{-1} and 10 h^{-1} for quinoline and DBT feed, respectively ($p(H_2)$ = 50 bar).

A pseudo-first order dependence on the hydrocarbon reactant was found to describe the kinetics of the hydrogenation of tetralin at steady state regardless of the experimental conditions (Equation 1, where X_{tet} is the conversion of tetralin at steady state and k is the product of the surface reaction rate constant and the reactants adsorption constant).

$$-\ln\left(1-X_{tet}\right) = \frac{k}{WHSV} \qquad (1)$$

2.2 Characterization of the spent catalyst samples

After tetralin hydrogenation, the catalyst samples were washed in hexane and subsequently sieved from SiC. The recovered catalysts were characterized by infrared spectroscopy (IR), transmission electron microscopy (TEM), elemental analysis and X-ray absorption spectroscopy (EXAFS and XANES). A Perkin Elmer 2000 spectrometer operating at a 4 cm^{-1} resolution mode was used for measuring the IR spectra. Prior to the IR measurements, the samples were activated in vacuum (p = 10^{-6} mbar) at 423 K for 2 h. Pyridine (Py) and carbon monoxide were used as probe molecules to characterize the acid and metal sites. For pyridine adsorption, the activated catalyst samples were exposed to pyridine vapor (p (Py) = 10^{-2} mbar) at 423 K for 0.5 h. After removing the excess of the adsorbate by outgassing at 423 K for 1 h the spectrum was recorded. The concentration of different Py-species on the surface was determined by a method based on the molar extinction coefficients [20].

For CO adsorption, the catalysts were activated in H_2 at 623K for 1 hour followed by 1 hour at the same temperature in vacuum (p = 10^{-6} mbar) to remove hydrogen. Then, the catalyst was cooled to 313 K. Carbon monoxide was adsorbed at 0.005, 0.05, and 0.5 mbar. At the end of the experiment, the sample was evacuated for 15 minutes at 10^{-6} mbar and the spectrum was recorded.

For the TEM study, a JEM-2010 Jeol transmission electron microscope operating at 120 kV was used. The recovered catalysts were ground, suspended in ethanol, and ultrasonically dispersed. Drops of the dispersions were applied on a copper grid-supported carbon film.

X-ray absorption spectra were collected at the beamlines X1 and C, HASYLAB, DESY, Hamburg, Germany. The storage ring was operated with an electron energy of 4.5 GeV and an average current of 100 mA. The Si (311) double crystal monochromator was detuned to 60 % of the maximum intensity to minimize the intensity of higher harmonics in the X-ray beam. The recovered catalysts were prepared as self supporting wafers and reduced in situ (H_2, T = 588 K for 2 h) followed by He treatment at 588 K for 1 h to remove adsorbed H_2. The X-ray absorption spectra were collected at the Pt L_{III} edge (11564 eV) at 77K (EXAFS) and 588K (XANES). For the EXAFS and XANES analysis, the scattering background was subtracted using a polynomial function and all spectra were normalized to unity. The position of the edge was calibrated using the spectra of a simultaneously measured Pt foil. The VIPER and XANDA software were used for analyzing the datasets [21].

For EXAFS analysis the oscillations were weighted with k^2 and Fourier transformed within the limits $k = 3.5 – 14$ Å $^{-1}$. The local environment of the Pt atoms was determined from the EXAFS using the phase-shift and amplitude function for Pt-Pt, Pt-O, Pt-C, Pt-N and Pt-S calculated assuming multiple scattering processes (FEFF Version 8.30) [22, 23].

3 Results

3.1 Characterization of the supported Pt catalysts

A detailed study of the nature, concentration, strength and origin of different types of acid sites was reported elsewhere [18]. A summary of the catalyst properties is presented in Table 1. It has to be mentioned here that the catalysts used in this chapter originate from other synthesis batches than the catalysts applied in the other chapters of this thesis. Therefore, small differences in composition and catalytic activity can be attributed to coincidental variations during the preparation process and statistical experimental errors in the characterization. One remarkable difference of the Pt/SiO_2 used for the work in this chapter is that it reveals an exceptional small BET surface area of 64 $m^2 \cdot g^{-1}$.

Table 1. Characterization of the oxide supported Pt catalysts: Chemical composition, textural properties and intermediate electronegativity of the support according to Sanderson (S int).

Catalyst	Composition (wt. %)			S_{int}	Acidity ($\mu mol \cdot g^{-1}$)		Pt size (nm)
	Pt	SiO_2	Al_2O_3		BAS	LAS	EXAFS
Pt/Al_2O_3	0.78	0.0	99.2	2.70	0	137	0.6
Pt/ASA (55/45)	0.82	46.2	53.0	2.86	24	128	0.8
Pt/ASA (20/80)	0.81	78.8	20.4	2.98	36	92	0.7
Pt/ASA (5/95)	0.78	94.9	4.3	3.04	26	65	0.8
Pt/SiO_2	1.03	99.0	0.0	3.05	0	0	1.4

All supports used have only meso- and macropores indicating that pore diffusion limitations of the bulky aromatic molecules are not possible. It should be noted that with increasing SiO_2/Al_2O_3 ratio in the catalysts a maximum in the concentration of Brønsted acid sites (Pt/ASA (20/80)) and a decrease in the concentration of Lewis acid sites was observed. The silica supported Pt catalyst was used as a neutral reference material. The intermediate electronegativity of the support (i.e., the Sanderson electronegativity [24]) increases with increasing concentration of silica in the mixed oxides and, thus, the value is used to indicate the overall composition and polarity of the used catalyst supports.

As shown in previous studies, the average metal cluster sizes determined by EXAFS were small and similar for the different catalysts except for Pt/SiO_2 (see Table 1) [18]. The particle size distribution was narrow as confirmed by TEM, which allows investigating the localized effect of the acid sites on the catalytic properties of the Pt nanoclusters without accounting for widely differing metal particle diameters.

3.2 Hydrogenation of tetralin in the presence of quinoline

The main reaction products during tetralin hydrogenation on the presence of quinoline were *cis*- and *trans*-decalin. The carbon mass balance of the liquid products was close to 100 % regardless of the reaction conditions indicating that gaseous reaction products were absent. The rate of hydrogenation normalized by the concentration of accessible Pt (TOF) at 180°C is shown as a function of the Brønsted acid concentration (see Figure 3). In contrast to the reaction with clean feed, the TOF of all catalysts tested was constant. The catalytic activity of tetralin hydrogenation in the presence of N-poisoned feed decreased to 10-20 % compared to the rates previously reported for non-poisoned feed [19]. Using the Arrhenius graph to derive the apparent energy of activation ($Ea_{(exp)}$) a value of 79 ± 2 kJ/mol was found for all catalysts. Note that this contrasts the trend of the $Ea_{(exp)}$ values increasing with increasing concentration of SiO_2 in the mixed oxides. [19].

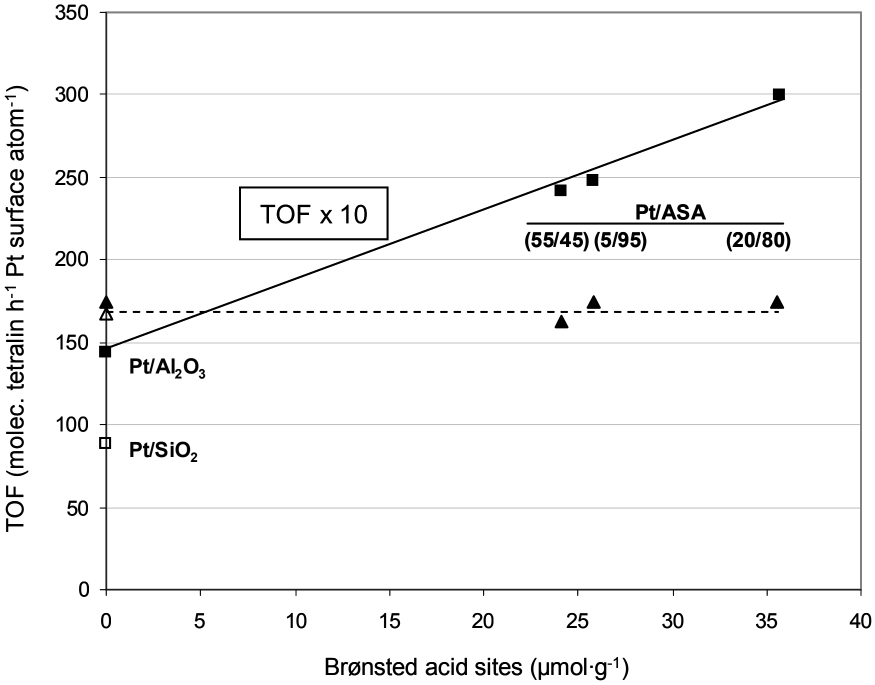

Figure 3. Hydrogenation of tetralin in the presence of quinoline (▲)(WHSV = 26 h^{-1}) and DBT(■)(WHSV = 10 h^{-1}) at 453 K over Pt/Al$_2$O$_3$, Pt/ASA (55/45), Pt/ASA (20/80), Pt/ASA (5/95) and Pt/SiO$_2$.

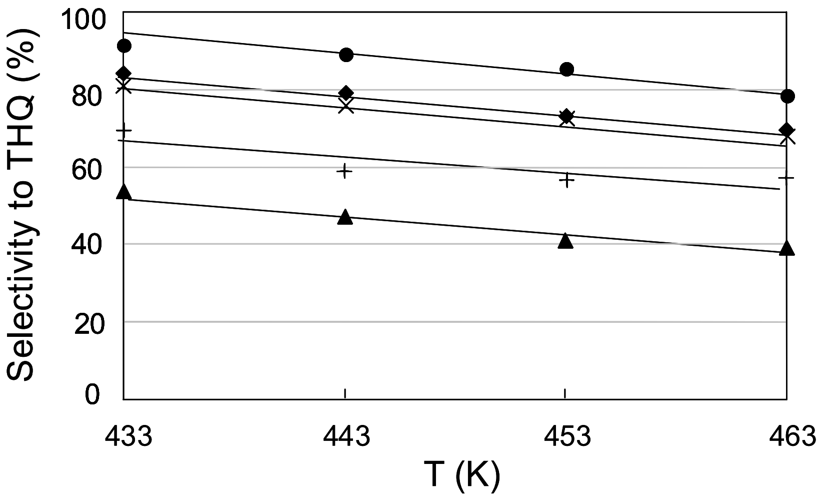

Figure 4. Selectivity to tetrahydroquinoline in the hydrogenation of quinoline over Pt/Al$_2$O$_3$ (♦), Pt/ASA (55/45) (X), Pt/ASA (20/80) (▲), Pt/ASA (5/95) (+), and Pt/SiO$_2$ (•) catalysts, in the temperature range from 433 K to 463 K.

The quinoline present in the feed was partially hydrogenated to tetrahydroquinoline (1, 2, 3, 4 THQ) in the presence of hydrogen over the metal catalyst (see Figure 4). The selectivity to this reaction varied between 40 and 100 % depending on the reaction conditions. At higher temperatures, the hydrogenation of quinoline to tetrahydroquinoline was less significant, but the conversion depended on the particular composition of the catalyst support. This was attributed to a promotion of a secondary reaction pathway over acid sites leading to decahydroquinoline. The secondary reaction pathway was least catalyzed over a neutral support (i.e., silica), while over acidic ASA supports it was strongly promoted. Other reaction pathways of quinoline would lead to hydrogenolysis and scission of the C – N bond. However, other products of the reaction of quinoline were not detected in the liquid phase at 160 – 190°C.

3.3 Hydrogenation of tetralin in the presence of DBT

As with quinoline as a poison, the main reaction products in the presence of DBT were *cis*- and *trans*- decalin. The catalytic activity was very low and a correlation with the intermediate electronegativity of the support was not observed. However, the variations in the TOF over the series of Pt catalysts increased linearly with the concentration of Brønsted acid sites of the support (see Figure 3).

It is interesting to note that the TOF for tetralin hydrogenation with Pt/SiO_2 showed weak, but noticeable activity, while for Pt/Al_2O_3 having accessible Lewis acid sites, a slightly higher catalytic activity was found. The catalyst activity increased with higher concentration of Brønsted acid sites on the ASA supports. The apparent energy of activation for the hydrogenation of tetralin in the presence of DBT over all catalysts was 73±1 $kJ\cdot mol^{-1}$. In order confirm the importance of the Brønsted acid sites in the presence of sulfur a Cs exchanged Pt/ASA catalyst was synthesized leading to a marginal BAS concentration (results not shown here). Indeed, its catalytic performance was only slightly above that of Pt/SiO_2 confirming the remaining metal activity in the absence of Brønsted acid sites and in the presence of sulfur poison.

The isomer ratio of *cis*- to *trans*- decalin was 1.4 for all catalysts investigated, which is significantly lower than the value found for the non-poisoned feed [19]. Dibenzothiophene in the feed was partly converted. The hydrogenation of DBT proceeded at higher reaction rates and led to much higher conversions compared to the hydrogenation of tetralin. A general first order dependence on the DBT concentration was found [25].

The apparent energies of activation were 60±1 kJ/mol for ASA supported Pt and 10 kJ/mol higher for Pt/Al_2O_3 and Pt/SiO_2. Also the rate of DBT hydrogenation increased with increasing concentration of Brønsted acid sites in the supports (see Figure 5). The slightly higher activity with Pt/Al_2O_3 compared to Pt/SiO_2 indicates that the presence of Lewis acid sites is beneficial to convert DBT.

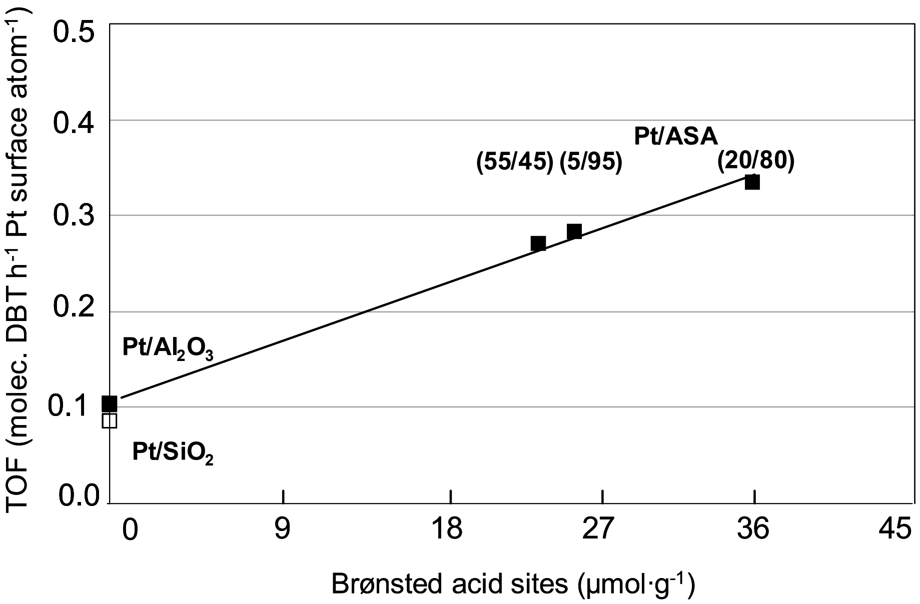

Figure 5. Turnover frequencies of DBT during the catalytic hydrogenation of tetralin at 453 K (WHSV = 10 h^{-1}).

3.4 Hydrogenation of tetralin in the presence of quinoline and DBT

20 ppm N as quinoline was added to the feed containing 100 ppm S as DBT in order to explore the effect of the simultaneous presence of molecules containing sulfur and basic nitrogen. In the temperature range of 433-463 K only a marginal tetralin hydrogenation activity was observed over all Pt catalysts and, thus, higher temperatures were needed for kinetic measurements (see Chapter 4). It is remarkable to note that quinoline could be added in concentration up to 400 ppm N in the absence of S, while maintaining appreciable activity.

3.5 Analysis of the catalyst samples after reaction

The concentration of sorption sites on the support and on the metal particles was probed by IR spectra of adsorbed pyridine and CO, respectively. In addition, the properties of the metal particles were analyzed by X-ray absorption spectroscopy of the used samples.

Pyridine adsorption followed by IR spectroscopy on the used catalyst samples was carried out in order to probe the effect of the nitrogen and sulfur compounds on the supported platinum catalysts during the hydrogenation of tetralin. The IR spectra of pyridine adsorbed on the spent Pt/ASA (55/45) catalysts are presented and compared to the spectrum of adsorbed pyridine on the fresh catalyst in Figure 6.

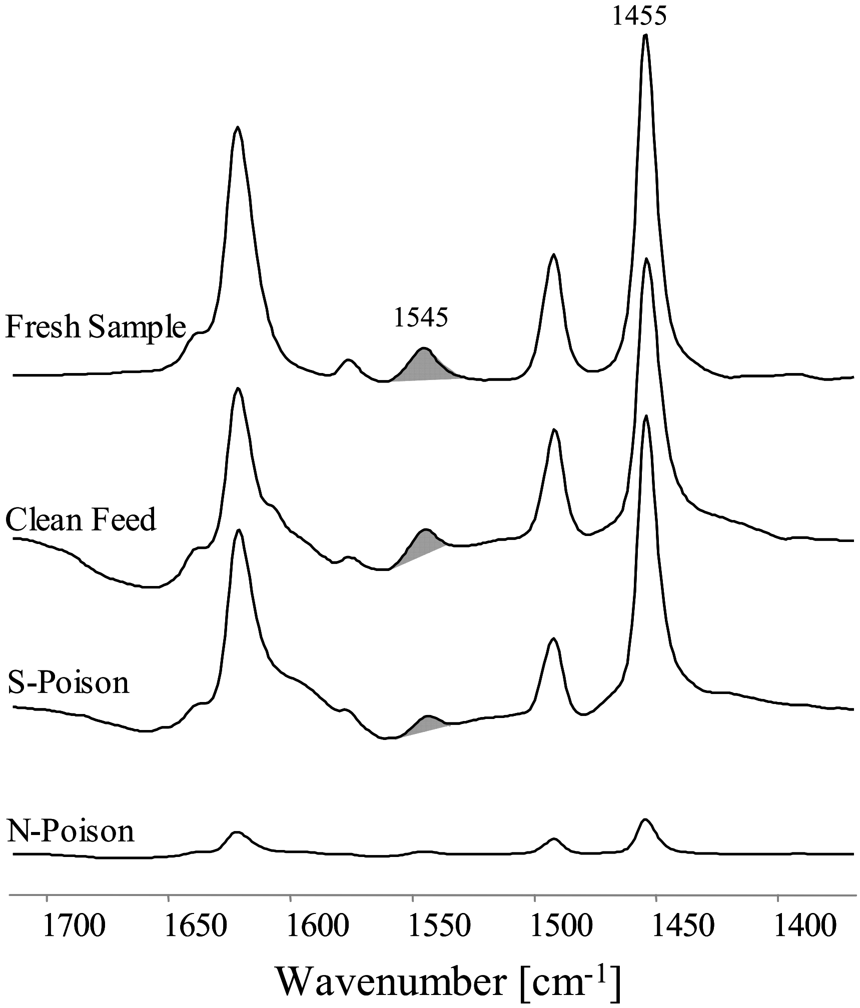

Figure 6. Pyridine adsorption IR study of spent and fresh Pt/ASA (55/45) samples.

After pyridine adsorption on the activated catalysts, bands at 1545 and 1455 cm^{-1} were assigned to pyridinium ions and coordinatively bonded pyridine, respectively [18]. The catalyst sample used for tetralin hydrogenation in the presence of DBT showed a slightly lower intensity of the band at 1545 cm^{-1} (adsorption on BAS) compared to the concentration of pyridine observed on the used catalysts after reaction with clean feed. Thus, DBT did not block the acid sites of ASA (55/45) to a higher extend than the coke formed in tetralin conversion. In contrast, the adsorption of pyridine was strongly reduced after hydrogenation of tetralin in the presence of quinoline. Thus, we conclude that quinoline adsorbs strongly on Brønsted and Lewis acid sites.

It should be noted here that the coverage of acid sites by the presence of quinoline in the feed was accompanied by a higher concentration of carbon deposits on the used catalysts compared to non poisoned and sulfur poisoned Pt/ASA samples. In these used samples also a high concentration of nitrogen was found, indicating the accumulation of N-containing coke. The results of the elemental C, H and N analysis of used Pt/ASA (5/95) are compiled in Table 2.

Table 2. C, H and N analysis of used Pt/ASA (5/95).

Catalyst	C (wt. %)	H (wt. %)	N (wt. %)
Pt/ASA (5/95) No poison	1.5	1.4	-
Pt/ASA (5/95) N-poison	6.5	1.7	0.52
Pt/ASA (5/95) S-poison	1.2	1.6	-
Pt/ASA (5/95) N+S-poison	7.9	1.9	0.35

The IR spectra of fresh and spent Pt/ASA (55/45) after CO adsorption and the adsorption capacities of the used samples are shown in Figure 7 a) and b).

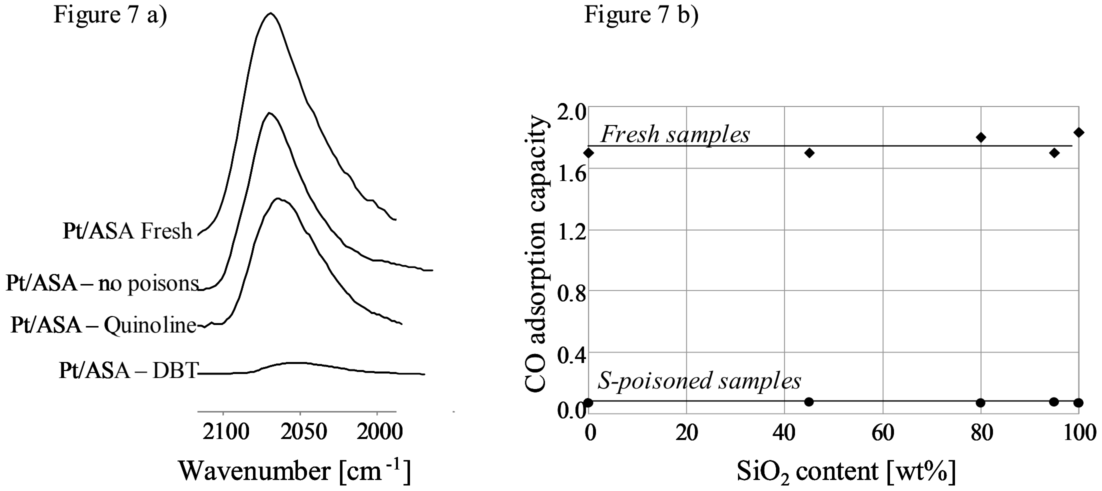
Figure 7 a)

Figure 7 b)

Figure 7. a) CO adsorption on fresh and spent Pt/ASA (55/45) catalyst samples. b) Adsorption capacity of all fresh oxide supported Pt catalysts and the corresponding used samples in the presence of DBT.

The adsorption capacity of linearly adsorbed CO at around 2070 – 2080 cm^{-1} on Pt was drastically reduced by the presence of DBT showing that less than 5 % of the original Pt surface was available for CO adsorption. It should be mentioned here that the level of coverage of the metal depends strongly on the operating conditions. Higher severity and longer time on stream led to substantial coverage of the metal clusters (results not shown). As the nature and concentration of CO adsorbed on Pt was similar regardless of the type of support, it is concluded that the support composition does not affect the metal resistance towards sulfur poisoning. When quinoline was present in the feedstock 60 % of the platinum surface sites were accessible for CO.

In order to explore the role of particle sintering in this process, fresh and used Pt/ASA (5/95) catalysts were analyzed by transmission electron microscopy (see Figure 8).

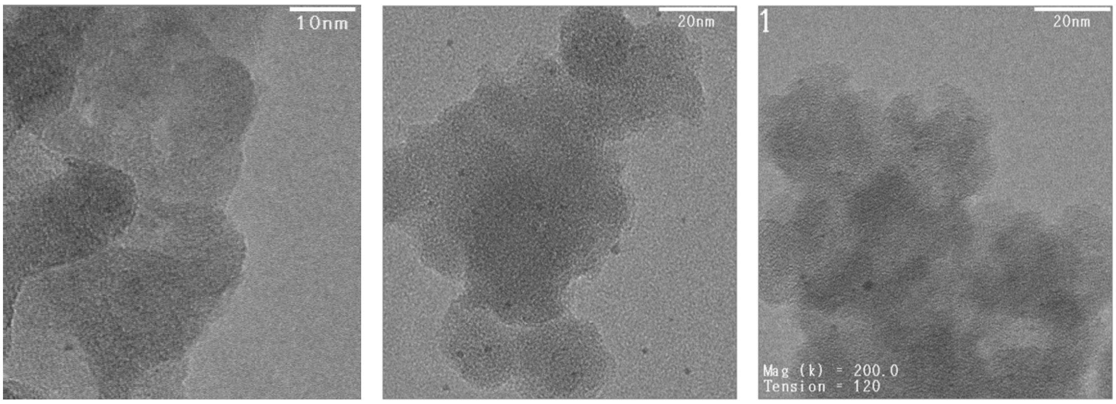

Pt/ASA (5/95) fresh Pt/ASA (5/95) after clean feed Pt/ASA (5/95) after Quinoline and DBT

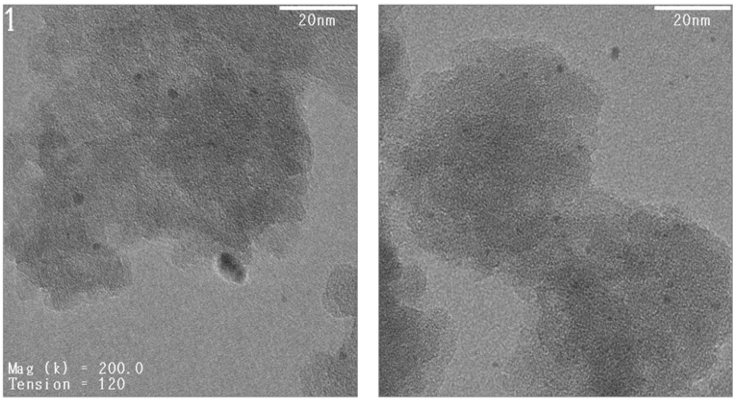

Pt/ASA (5/95) after DBT Pt/ASA (5/95) after Quinoline

Figure 8. TEM micrographs of Pt/ASA (5/95) before and after the hydrogenation of tetralin in the presence and absence of DBT and quinoline.

By counting 300 Pt particles per catalyst, a histogram was generated and the average cluster sizes were calculated. The average platinum particle size increased after tetralin hydrogenation in the absence and presence of DBT and quinoline, from 0.8 nm to 1.3 - 1.6 nm, respectively (see Table 3).

Particle sintering during tetralin hydrogenation was further confirmed by EXAFS analysis of the used catalysts (Figure 9). The average Pt-Pt coordination numbers increased from 6.2 to 7.2-7.7 corresponding to particle diameters ranging between 1.2-1.4 nm (Table 3).

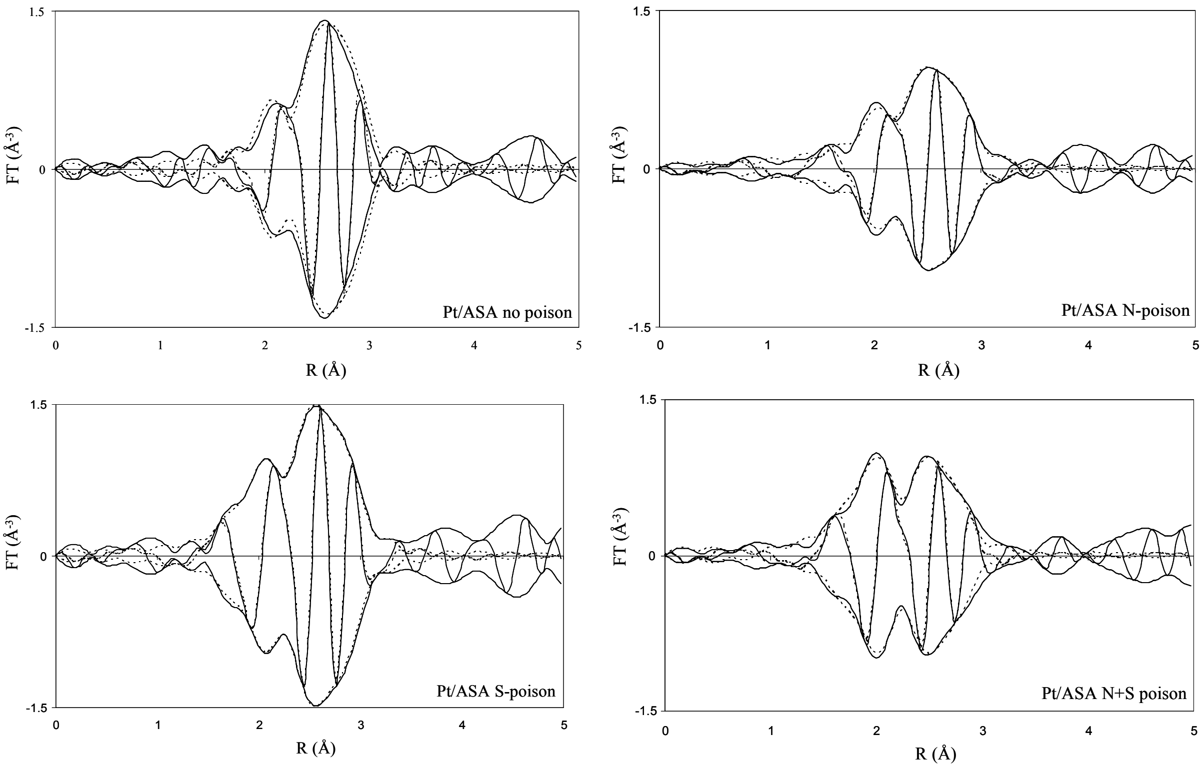

Figure 9. Fourier transforms (k^2 –weighted, Δk 3.5-14 $Å^{-1}$) of used Pt/ASA (5/95) and their Pt-Pt, Pt-C, Pt-N and Pt-S fitted contributions (dotted lines) after in situ H_2 reduction at 588 K.

The EXAFS analysis was also used to evaluate the presence and extent of Pt-C, Pt-N and Pt-S bonds on the particles (Table 3). In the absence of poisons 1.3 C neighbors per Pt atom at 2.11 Å indicate coke deposit formation over the active metal phase during the hydrogenation. When quinoline was present in the feed Pt-C contributions were not detected, but Pt-N contributions at 2.12 Å were observed indicating preferential adsorption of N containing species on Pt. When 100 ppm S was added to the feed one Pt-S bond per Pt atom at ~ 2.32 Å was identified in the presence of 100 ppm S, even when 20 ppm N was added to the DBT containing feed (0.8 Pt-S). S obviously adsorbs very strongly on the metal and, thus, inhibits adsorption of all other species.

Table 3. Results of the EXAFS analysis of used Pt/ASA (5/95).

Catalyst	Mean particle size[1] (nm)	Scatter	N	r (Å)	$10^3 \cdot \Delta\sigma^2$ (Å^2)	ΔE_0 (eV)
Pt/ASA (5/95) No poison	1.3 (1.2)	Pt-Pt	7.2	2.75	5.0	6.5
		Pt-C	1.3	2.11	17.9	20.6
Pt/ASA (5/95) N-poison	1.6 (1.3)	Pt-Pt	7.3	2.71	6.8	6.1
		Pt-N	1.3	2.12	24.1	25.8
Pt/ASA (5/95) S-poison	1.5 (1.3)	Pt-Pt	7.4	2.75	4.0	9.2
		Pt-S	1.0	2.34	8.4	16.2
Pt/ASA (5/95) N-+S-poison	1.4 (1.4)	Pt-Pt	7.7	2.72	8.9	5.2
		Pt-S	0.8	2.32	0.0	15.2
Pt foil	-	Pt-Pt	12.0	2.76	3.4	11.1

[1] determined by TEM and EXAFS particle modeling (in brackets)

The impact on the Pt structure and the presence of different adsorbates depending on the character of the catalyst poison were also visible from the XANES spectra in Figure 10.

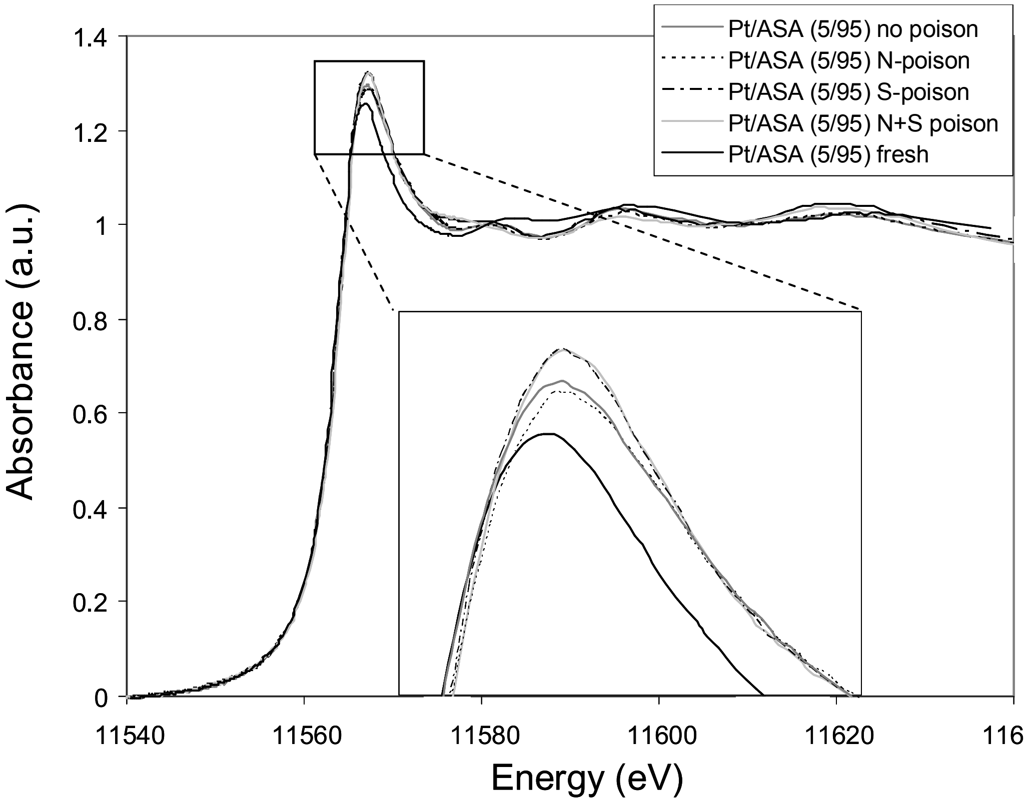

Figure 10. Normalized XANES spectra at the Pt L_{III} edge in He at 588 K of Pt/ASA (5/95) catalysts before and after the hydrogenation of tetralin.

The white line intensity of Pt/ASA (5/95) clearly increased during tetralin hydrogenation when comparing the fresh with the used Pt catalyst, which is tentatively attributed to metal particle sintering. Indeed, EXAFS and TEM showed that sintering occurred to the same extent during tetralin hydrogenation in the absence and presence of poisons. Therefore, a direct comparison of the electronic structure of the used samples by XANES is possible. The presence of S or S+N in the feed led to a higher white line intensity compared to clean feed and the N containing reactant mixture. Apparently, the level of electron density within the Pt cluster was reduced due to the presence of sulfur species adsorbed on the metal surface. This result confirms the EXAFS analysis that suggests a very strong adsorption of S containing compounds on Pt.

The white line height slightly decreased when quinoline was used compared to clean feed showing that the nitrogen adsorbents induce also an electronic modification of the Pt particles, which differs from that induced by solely carbonaceous adsorbents. In conclusion, the decrease of accessible Pt surface can be ascribed to the formation of an inactive phase over the metal surface and to particle sintering. The former can be related to the generation of Pt-S, Pt-N and Pt-C bonds and the formation of coke deposits.

The electronic properties of the platinum particles on the different ASA supports after the hydrogenation of tetralin in the presence of DBT were explored by XANES analysis.

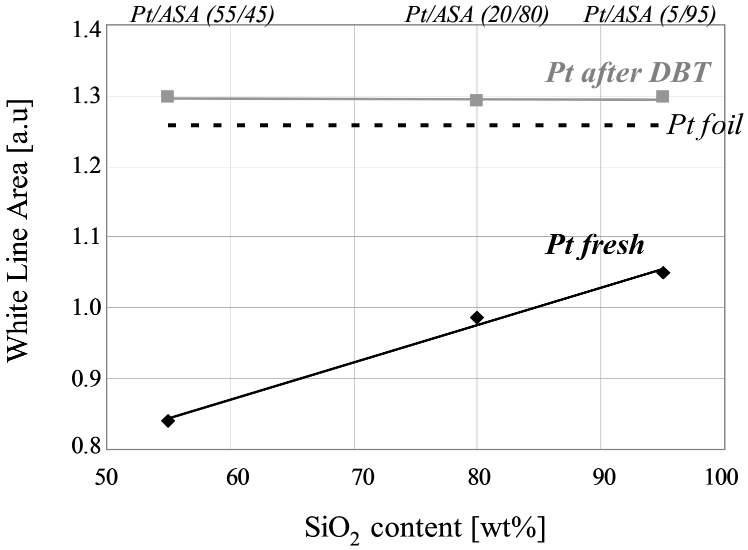

Figure 11. Values of the areas of the peaks above the L_{III} edge of the fresh samples and after the reaction in the presence of DBT as a function of the silica content in the support.

The intensity of the white line in the XANES at the Pt L_{III} edge of the Pt/ASA catalysts is identical for all ASA supports. This suggests that the electron density of platinum after the reaction in the presence of DBT is unrelated to the composition of the support.

4 Discussion

The impact of sulfur containing molecules as well as that of basic nitrogen compounds had a marked effect on the activity of oxide supported Pt catalysts in the hydrogenation of tetralin.

In the presence of quinoline, neither the rate of hydrogenation of tetralin nor the apparent energy of activation varied with the composition of the supports. This is attributed to the equalization of the acidic properties of the support caused by the basic properties of the nitrogen species neutralizing BAS and LAS [26]. The higher level of coke formation and the preferred location of coke on the support indicates that it is generated through the stronger interaction of pyridinic rings with Brønsted acid sites and the subsequent addition of aromatic rings or naphthenic rings to these surface species. Thus, a comparatively high N-induced coke formation was observed by elemental analysis of the used Pt/ASA catalyst. The pyridine adsorption IR spectroscopy analyses of the spent catalysts show that most of the nitrogen containing deposit is likely located on the support. Further, the build-up of the coke on the support likely decreases a possible interaction with the Pt cluster.

The fairly high and uniform values of $Ea_{(exp)}$ for the tetralin hydrogenation in the presence of quinoline, in comparison to the values obtained in its absence [19], can be explained taking into account the competitive adsorption of tetralin with the N-poison. The heat of adsorption of tetralin is included in the energy of activation (i.e., the hydrogenation is first order in tetralin). Apparently quinoline and its hydrogenated products occupy the strong active hydrogenation sites leaving behind weaker adsorption sites for tetralin. Assuming that the true energy of activation of tetralin is always the same, then a decrease in the heat of adsorption of tetralin, originates the observed differences in $Ea_{(exp)}$. According to the EXAFS study, where a significant Pt-N, but no Pt-C contribution was observed, the N-poison adsorbs better on the Pt surface than tetralin as quinoline exhibits a more electron rich aromatic system. Thus, the active sites (i.e., those exhibiting a high enthalpy of adsorption) are covered with N-poison. The residual, less active sites are available for tetralin; however, the lower heat of adsorption associated with these sites is indicated by the increase of $Ea_{(exp)}$. A slightly different scenario could be proposed considering that quinoline donates electrons to the metal surface, reducing its electrophilicity. In consequence a higher electron density on the metal surface will weaken the adsorption of any olefinic intermediate [27-29]. The decreased XANES white line intensity of the used catalyst, which was exposed to quinoline compared to the one when clean feed was used, reveals a higher electron density of platinum in the presence of N-poison.

4.1 Hydrogenation of tetralin in the presence of DBT

The hydrogenation of tetralin in the presence of DBT was drastically reduced, undoubtedly due to the reaction of the S-species with platinum. According to the HSAB principle the soft Lewis acid Pt interacts strongly with S containing soft Lewis bases like DBT. Evaluation of the EXAFS of used Pt/ASA clearly confirmed the presence of sulfur on the platinum surface as a Pt-S coordination number of 1 was found. It is known that the high stability of metal sulfide species is the origin of the rapid deactivation of the metallic function of the catalytic activity even at very low sulfur concentrations in the feed [2, 30]. Under our experimental conditions the hydrogenation of dibenzothiophene was relatively faster than that of tetralin. This illustrates further the high preference for the adsorption of DBT on platinum. Nevertheless, some residual catalytic activity for hydrogenating tetralin was observed (approximately 2 % of the rate recorded with clean feed). A linear correlation was found between the rate of tetralin hydrogenation and the concentration of Brønsted acid sites in the ASA supports. On the other hand, the intermediate electronegativity (i.e. the polarity) of the support did not correlate with the reaction rate. S-species are adsorbed on platinum under the applied experimental conditions and a full decomposition of the S-molecules lead to a sulfur deposit on the Pt-surface. Consequently, electron transfer from the metal to the non-metal occurs, due to the difference in electronegativity between the elements. Therefore, the lower electron density of Pt caused by S adsorption leads to an increased white line intensity of all Pt/ASAs to the same extent, superposing metal-support interactions that were observed in the absence of catalyst poisons [19]. Nevertheless, DBT and tetralin are actually hydrogenated, thus, the activation of the hydrogen molecule is still feasible.

It can be summarized that Brønsted acid sites in the vicinity of Pt serve as active sites where tetralin can be hydrogenated by hydrogen that can be still dissociated on S covered Pt.

4.2 Hydrogenation of tetralin in the presence of quinoline and DBT

Tetralin hydrogenation in the presence of tetralin led to insignificant conversion levels over all oxide supported Pt catalysts even at a very low WHSV of 1.0 h^{-1} and only 20 ppm of N in addition to 100 ppm of S in the temperature range of 433 - 463K. It was observed before that the individual poisons DBT and quinoline inhibit the catalytic function of Pt/ASA in two different manners. Sulfur strongly poisons the metallic function, which already causes a rigorous activity decrease of catalyst activity. In that case only the minor reaction pathway, where tetralin is hydrogenated over Brønsted acid sites at the perimeter of the Pt cluster, is feasible. The strong base quinoline, however, leads to a neutralization of the support acidity, which inhibits the alternative hydrogenation route in addition to a decreased metal activity due to a competitive adsorption of quinoline and tetralin on strong Pt adsorption sites. Consequently, when DBT and quinoline are both present in the feedstock, all catalytic active sites of Pt/ASA for the hydrogenation of tetralin are blocked leading to inactive catalysts.

EXAFS of the used Pt/ASA catalyst revealed a Pt-S coordination number of 0.8 in addition to the Pt-Pt coordination, but no Pt-C and Pt-N contribution was observed. This confirms the stronger metal affinity of sulfur compared to the N-poison and tetralin. Therefore, the white line above the Pt L_{III} edge of Pt/ASA after exposure to S- and N-poison is as intense as the one monitored when Pt is solely poisoned by sulfur.

Elemental analysis of the spent catalyst reveals that quinoline in the feedstock causes an increased build-up of coke similarly to the formation of carbenoceous deposits that is observed when only N-poison is present in the feed.

4.3 Proposed hydrogenation model

It is generally accepted that hydrogenation of aromatics takes place on the noble metal phase when supported on oxide supports. In one of our previous studies we have found that a higher electronegativity of the support leads to more electron deficient Pt nanoclusters that are favorable for a better catalyst hydrogenation and also hydrogenolysis activity [19]. In the presence of S-containing molecules this main hydrogenation pathway is blocked, which was confirmed in the present study by EXAFS, XANES and the catalytic results in the presence of DBT and quinoline. Nevertheless a residual tetralin hydrogenation activity was observed in the presence of DBT that could be correlated with the Brønsted acid site concentration of the support.

In order to account for the above presented results we propose a model for the hydrogenation of tetralin at the perimeter of the S-poisoned Pt cluster. The tetralin molecule, anchored on the Brønsted acid sites, is saturated upon reaction with hydrogen that dissociates on an adjacent Pt-S cluster. The proposed reaction pathways on an active and on a poisoned platinum cluster, respectively, are shown in Figure 12.

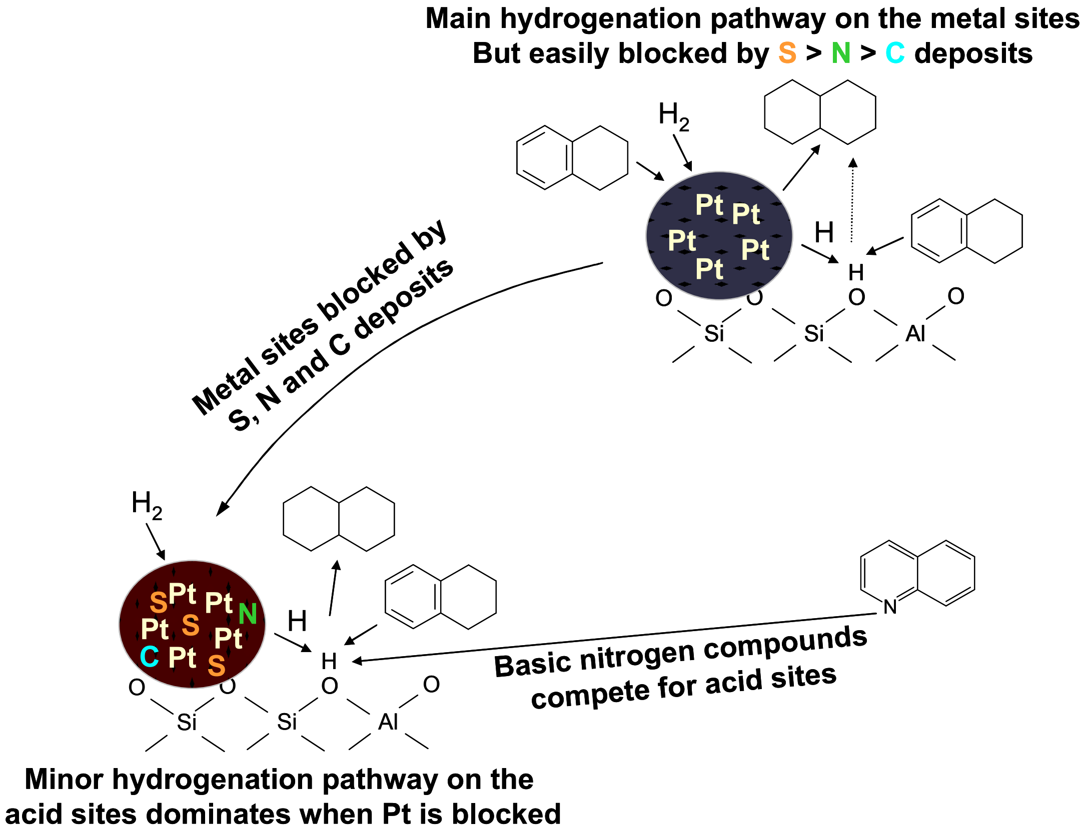

Figure 12. Reaction pathways for the hydrogenation of tetralin in the absence and presence of DBT and quinoline.

5 Conclusions

The catalytic hydrogenation of tetralin over Pt/ASA catalysts has been studied in the presence of quinoline and dibenzothiophene. Two types of active sites for the catalytic hydrogenation were identified: (1) those on the metal particles and (2) those on the perimeter of the metal particles, where an acid site anchors the aromatic molecule to be further hydrogenated by hydrogen activated on platinum. The former pathway generates the high catalytic activity of the supported platinum catalysts in the hydrogenation of aromatics. The metal-support interaction can be used to tune the catalytic activity of nanosized Pt-clusters. However, in the presence of basic N-poisons the acid sites and a fraction of the metal sites are blocked. Furthermore quinoline induces enhanced coke formation. Therefore, the electronic effects are eliminated and the strong competition between tetralin and quinoline for the metal sites leads to an increase of the apparent energy of activation for tetralin hydrogenation. The S-poison molecule first targets the metal sites inhibiting metal-support interactions. The dissociation of hydrogen molecules on the poisoned metal is still possible providing hydrogen atoms for the alternative minor hydrogenation pathway. This hydrogenation route is not significant when Pt is not covered by any poison or coke, but becomes the main pathway to hydrogenate tetralin molecules in the presence of S-poisons. Therefore, an increase in the concentration of anchoring Brønsted acid sites in the vicinity of S-poisoned Pt leads to an increase in the catalytic activity despite the presence of DBT.

Acknowledgments

Financial support of S.R.T.C. Amsterdam is gratefully acknowledged. Andreas Marx, Martin Neukamm and Xaver Hecht showed invaluable support. The XAFS experiments were carried out at station X1 and C at HASYLAB, DESY, Hamburg, Germany and supported by the TMR-Contract ERBFMGECT950059 of the European Community. Fruitful discussions in the framework of IDECAT are gratefully acknowledged.

6 References

1. B. H. Cooper and B. B. L. Donnis, Appl. Catal. A-Gen., 1996. 137(2) 203.
2. J. Barbier, E. Lamy-Pitara, P. Marecot, J. P. Boitiaux, J. Cosyns and F. Verna, Advances in Catalysis, 1990. 37 279.
3. A. Stanislaus and B. H. Cooper, Catal. Rev.-Sci. Eng., 1996. 38(1) 159.
4. F. Figueras, R. Gomez and M. Primet, Advances In Chemistry Series, 1973(121) 480.
5. P. Gallezot, *Catalysis by Zeolites*, ed. B. Imelik, et al. Vol. 5. 1980, Amsterdam: Elsevier Science. 227.
6. T. T. Phuong, J. Massardier and P. Gallezot, J. Catal., 1986. 102(2) 456.
7. R. Szymanski, H. Charcosset, P. Gallezot, J. Massardier and L. Tournayan, J. Catal., 1986. 97(2) 366.
8. M. T. Tri, J. Massardier, P. Gallezot and B. Imelik, *Metal-support and Metal Additives Effects in Catalysis*, ed. B. Imelik, et al. Vol. 11. 1982, Amsterdam: Elsevier. 141.
9. P. Chou and M. A. Vannice, J. Catal., 1987. 107(1) 129.
10. S. D. Lin and M. A. Vannice, J. Catal., 1993. 143(2) 563.
11. M. V. Rahaman and M. A. Vannice, J. Catal., 1991. 127(1) 251.
12. M. V. Rahaman and M. A. Vannice, J. Catal., 1991. 127(1) 267.
13. L. Simon, J. G. van Ommen, A. Jentys and J. A. Lercher, J. Catal., 2001. 201 60.
14. L. Simon, J. G. van Ommen, A. Jentys and J. A. Lercher, Stud. Surf. Sci. Catal., 2001. 135 166.
15. L. Simon, J. G. van Ommen, A. Jentys and J. A. Lercher, J. Catal., 2001. 203 434.
16. L. Simon, J. G. van Ommen, A. Jentys and J. A. Lercher, Catal. Today, 2002. 73 105.
17. L. Simon, J. G. van Ommen, P. J. Kooyman, A. Jentys and J. A. Lercher. *Sulfur tolerance of alkali exchanged zeolites for benzene hydrogenation*. in *Proc. DGMK- Conference on "The Future Role of Aromatics in Refining and Petrochemistry"*. 1999.

18. M. F. Williams, B. Fonfé, C. Sievers, A. Abraham, J. A. van Bokhoven, A. Jentys, J. A. R. van Veen and J. A. Lercher, J. Catal., 2007. 251(2) 485.
19. M. F. Williams, B. Fonfé, C. Woltz, A. Jentys, J. A. R. van Veen and J. A. Lercher, J. Catal., 2007. 251(2) 497.
20. C. A. Emeis, J. Catal., 1993. 141(2) 347.
21. K. V. Klementiev, *VIPER and XANDA for Windows, freeware*.
22. A. L. Ankudinov, B. Ravel, J. J. Rehr and S. D. Conradson, Phys. Rev. B, 1998. 58 7565.
23. A. L. Ankudinov and J. J. Rehr, Phys. Rev. B, 2000. 62 2437.
24. R. T. Sanderson, *Polar Covalence*. 1983: Academic Press.
25. H. R. Reinhoudt, R. Troost, S. van Schalkwijk, A. D. van Langeveld, S. T. Sie, J. A. R. van Veen and J. A. Moulijn, Fuel Processing Technology, 1999. 61(1-2) 117.
26. M. J. Girgis and B. C. Gates, Ind. Eng. Chem. Res., 1991. 30(9) 2021.
27. G. Leitz and J. Volter, *Mechanism of Hydrocarbon reactions*. 1975, Amsterdam: Elsevier. 151.
28. J. J. Rooney, Journal Of Molecular Catalysis, 1985. 31(2) 147.
29. J. J. Rooney and G. Webb, J. Catal., 1964. 3(6) 488.
30. C. H. Bartholomew, P. K. Agrawal and J. R. Katzer, Advances In Catalysis, 1982. 31 135.

Chapter 4

Hydrogenation of tetralin by amorphous silica-alumina supported Pt and Pt-Pd catalysts II – Influence of the metal alloy formation, support composition and reaction temperature on the sulfur and nitrogen poison tolerance

Monometallic Pt and bimetallic Pt-Pd clusters were supported on silica, alumina and amorphous silica-alumina (ASA) with varying acidity. In the present work the function of Brønsted acid sites and Pt-Pd alloy formation were addressed studying the hydrogenation of tetralin in the presence and absence of sulfur as DBT and nitrogen as quinoline in the industrial relevant temperature range between 260 and 320°C. The continuous catalyst deactivation with clean tetralin feed is attributed mainly to metal site blocking by aromatic deposits, whereas fast initial deactivation by DBT is due to strong metal-sulfur bonds. The superior catalytic performance of Pt compared to the Pd surface enriched Pt-alloy is due to the general better hydrogenation performance of Pt leading also to enhanced N-poison removal at higher temperatures. Lower adsorption strength of electrophilic S on very electron deficient ionic $Pt^{x\delta+}$ *-* $xPd^{\delta-}$ *bonds leads to a good S tolerance of Pt-Pd alloys at low hydrogenation temperatures or when the S poison concentration is high (500ppm S as DBT).*

1 Introduction

Environmental legislations worldwide lead to an increasing demand of clean fuel production in refineries. Despite achieving ultra low sulfur levels it is important to produce diesel fuel with low aromatics content as especially polyaromatic compounds are known to be precursors of diesel exhaust particulates.

Noble metals have been extensively studied as catalysts for aromatics saturation as they are very active even at lower temperatures, which is important to overcome the thermodynamic constraints of hydrogenation reactions. Unfortunately, noble metal catalysts are easily poisoned by very small amounts of sulfur and to a lower extent by nitrogen compounds that are also always present in feedstocks.

Many investigations show that the sulfur tolerance of noble metals can be altered by using acidic carriers. In Chapter 3 it was demonstrated that Brønsted acid sites (BAS) in amorphous silica-alumina materials (ASAs) located closely to nano-sized Pt clusters open an alternative pathway for tetralin hydrogenation becoming especially significant when the metal catalyzed route is blocked by strongly adsorbed sulfur compounds. Therefore it is favorable to support small Pt particles on moderate acidic supports with a high concentration of BAS to avoid unwanted cracking reactions and to achieve a high sulfur resistance.

Basic nitrogen compounds in hydrotreating feedstocks can neutralize acidic supports, which is a big drawback of these noble metal carriers. Another strategy to improve the sulfur tolerance is the synthesis of supported bimetallic noble metal catalysts. Especially electronic effects in Pt-Pd alloy systems were found to increase the sulfur resistance in aromatics hydrogenation [1, 2]. This effect is explained by Pt-Pd interactions leading to electron deficient Pt atoms.

The scope of the present work is to investigate the hydrogenation of tetralin by ASA supported Pt and Pt-Pd catalysts at industrial relevant reaction conditions (260 – 320°C, 50 bar). A special focus is pointed on the role of the acidity and metal alloy formation on the catalyst performance in the presence of dibenzothiphene and quinoline, respectively, being representative compounds of S-and N-poisons in diesel feedstocks.

The synthesis and detailed characterization of the Pt and Pt-Pd catalysts have been previously reported in Chapter 2 together with the catalytic activity with respect to tetralin hydrogenation at lower temperatures in Chapter 3 and [3, 4].

2 Experimental

2.1 Preparation and chemical composition of Cs-exchanged Pt/ASA (38/62)

The parent Pt/ASA (38/62) catalyst was prepared by the same preparation method as described for the other Pt/ASA samples in Chapter 2. In order to exchange this catalyst with Cs the sample was first reduced in flowing H_2 (1 bar) at about 400 ºC and then cooled to RT in He. After passivation at RT (1 % O_2 in He) the sample was unloaded and impregnated with an aqueous solution of $CsNO_3$ (30 mg Cs/g catalyst) followed by equilibration on a mini rolling road (1 h). Then the catalyst was predried with a hair drier in a baffled flask in tumbling motion for1 hour and further dried (2 h at 120 ºC) and calcined (2 h at 300 ºC) in a muffle furnace.

2.2 Catalytic measurements

The hydrogenation of tetralin was carried out in a set of 4 parallel trickle-bed reactors in continuous down-flow mode as described in Chapter 3.

In the present study the catalyst testing was carried out at 533 -593 K and 50 bar hydrogen pressure with a weight hourly space velocity (WHSV) of 539.3 h^{-1} for clean feed, 270.6 h^{-1} for N-poison feed, 77.3 h^{-1} for S-poison feed and 32.4 h^{-1} for N+S-poison feed. A change of the WHSV was achieved by a change in the amount of catalyst and/or the flow rate (a constant molar ratio of H_2 to tetralin of 20.5 was maintained).

2.3 Characterization of the used catalysts samples

After tetralin hydrogenation, the catalyst samples were washed in hexane and subsequently sieved from SiC. The recovered catalysts were characterized by infrared spectroscopy (IR) and transmission electron microscopy (TEM).

A Perkin Elmer 2000 and a Bruker ISF88 spectrometer operating at a 4 cm^{-1} resolution mode were used for measuring the IR spectra.

Pyridine (Py) and carbon monoxide were used as probe molecules to characterize the acid and metal sites.

Prior pyridine adsorption, the samples were activated in vacuum ($p = 10^{-6}$ mbar) at 423 K for 2 h. The activated catalyst samples were exposed to pyridine vapor (p (Py) = 10^{-2} mbar) at 423 K for 0.5 h. After removing the excess of the adsorbate by outgassing at 423 K for 1 h the spectrum was recorded. The concentration of different Py-species on the surface was determined by a method based on the molar extinction coefficients [5].

For CO adsorption, the catalysts were activated in H_2 at 623K for 1 hour followed by 1 hour at the same temperature in vacuum ($p = 10^{-6}$ mbar) to remove hydrogen. Then, the catalyst was cooled to 313 K. Carbon monoxide was adsorbed at 0.005, 0.05, and 0.5 mbar. At the end of the experiment, the sample was evacuated for 15 minutes at 10^{-6} mbar and a final spectrum was recorded.

For the TEM study, a JEM-2010 Jeol transmission electron microscope operating at 120 kV was used. The recovered catalysts were ground, suspended in ethanol, and ultrasonically dispersed. Drops of the dispersions were applied on a copper grid-supported carbon film. Transmission electron micrographs were recorded at a magnification of 200,000.

3 Results

3.1 Hydrogenation of tetralin by oxide supported Pt and Pt-Pd catalysts

Tetralin hydrogenation was the predominant reaction (see reaction scheme in Chapter 1) for all catalysts. Secondary reactions on the acid sites (e.g., isomerization, hydrocracking) were hardly observed. Apparently, up to 320°C, the acid sites of the support do not catalyze by-product formation under the applied reaction conditions. It was further observed that the carbon mass balance in the liquid phase was close to 100 %, thus no reaction products were present in the gas phase.

Typical turnover frequency profiles over the oxide supported Pt catalysts in dependence of time on stream (TOS) and temperature are shown in Figure 1.

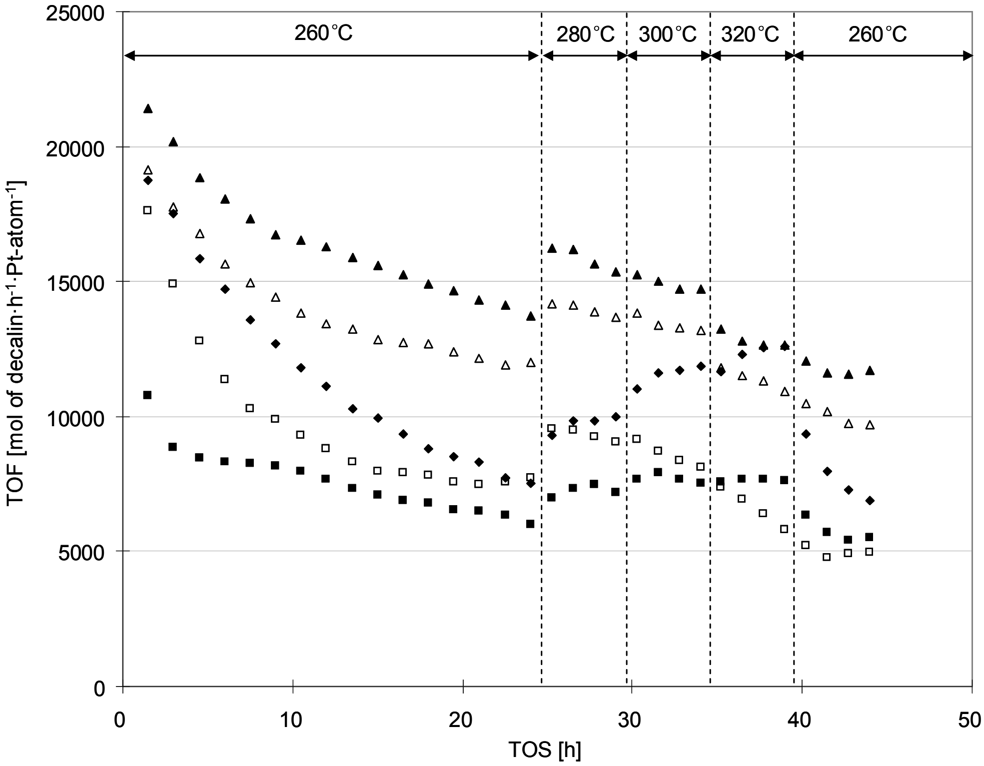

Figure 1. Hydrogenation of tetralin over Pt/Al_2O_3 (♦), Pt/ASA (55/45) (■), Pt/ASA (20/80) (▲), Pt/ASA (5/95) (△), and Pt/SiO_2 (□) in the temperature range from 260 – 320°C (50 bar, WHSV = 539.3 h^{-1}).

The initial conversion of tetralin decreased continuously. The deactivation rate was independent from the hydrogen pressure. This was tested in three equal experiments over Pt/ASA at 40, 50 and 60 bar, respectively. By increasing the temperature from 280 to 300°C only a minor activity increase was observed and by increasing to 320°C tetralin hydrogenation proceeded even at lower reaction rates besides for Pt/Al_2O_3 and Pt/ASA (55/45). Apparently a high alumina fraction in the support prevents further catalyst deactivation at industrial relevant temperatures above 300°C. For the further kinetic analysis the activity at a residence time of 24 h time on stream was used.

A first order dependence of the activity on the hydrocarbon concentration could be used to describe the kinetics of the hydrogenation of tetralin after 24 hours (Equation 1, where X_{tet} is the conversion of tetralin at steady state and k is the product of the surface reaction rate constant and the reactant adsorption constants) [4].

$$-\ln\left(1-X_{tet}\right) = \frac{k}{WHSV} \qquad (1)$$

Unlike to the findings at 160 – 190°C, where the rate of hydrogenation of tetralin increased with increasing Sanderson electronegativity for all catalysts containing alumina [4], the activity of the Pt/ASA catalysts here correlated with the concentration of Brønsted acid sites in the ASA support that were determined in Chapter 2 by pyridine adsorption IR. Notably the activity of Pt/ASA (55/45) was even lower than that of Pt/SiO_2 and Pt/Al_2O_3. The latter two catalysts do not exhibit any Brønsted acidity. An indication towards a stronger bonding of reactants to the Pt nanoparticles is obtained from the *cis*- to *trans*-selectivity of the final hydrogenation product decalin [4]. A weaker adsorption of tetralin on the metal favors the formation of the *trans*-isomer, while a stronger adsorption will lead directly to the formation of *cis*-decalin. Therefore it can be concluded that the low concentration of *cis*-decalin formed over Pt/ASA (55/45) (see Figure 2) originated from a low tetralin adsorption strength leading to the lowest catalytic activity among the tested catalysts. In order to explore the change of the isomer ratio due to the thermodynamically driven shift of the *cis*- to the *trans*-product after secondary re-adsorption of decalin, a blank experiment was performed. In this experiment the temperature range and pressure was similar to the tetralin hydrogenation experiments. Instead of 20 wt% tetralin, 20 wt% of a *cis* - *trans*-decalin mixture (*cis-/trans* ratio = 0.65) was added into the feed. As decalin isomerization started at around 240°C, we can explain the decreasing *cis-/trans* ratios observed at increasing temperatures presented in Figure 2.

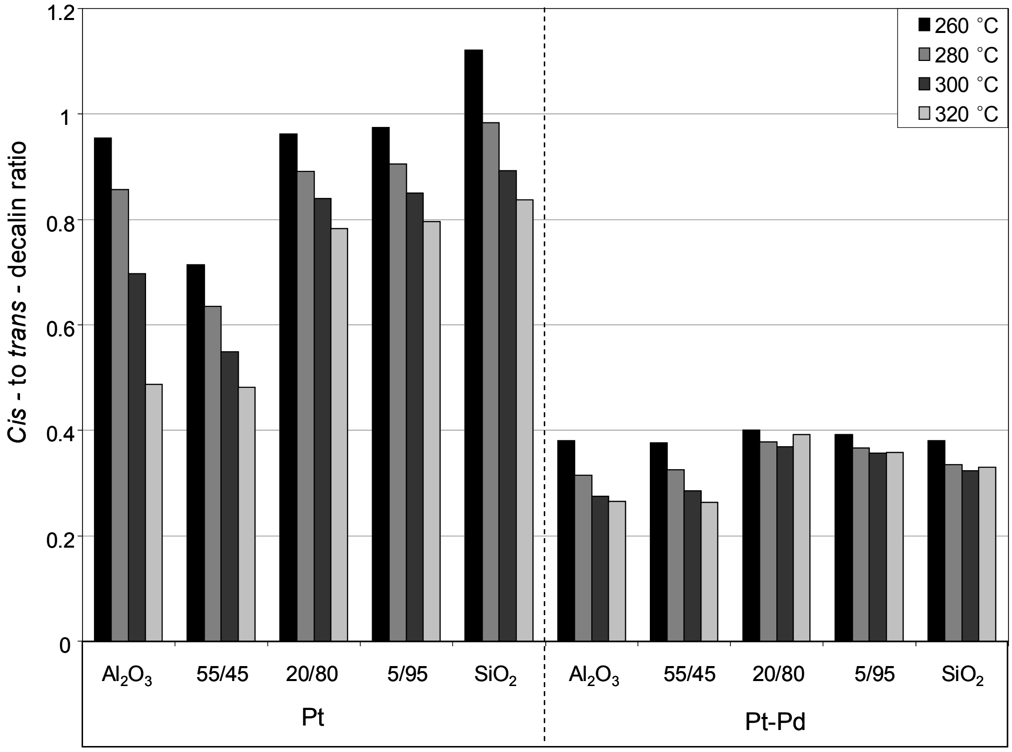

Figure 2. *Cis* - to *trans* – decalin ratios over oxide supported Pt and Pt-Pd catalysts.

The turnover frequency profiles of the supported Pt-Pd catalysts were similar to those of the monometallic Pt catalysts. An initial strong deactivation was followed by a continuous weaker deactivation in the first 24 hours. Also here a temperature increase to 320° C led to a further activity decrease of the catalysts besides Pt-Pd Al_2O_3 as shown in Figure 3.

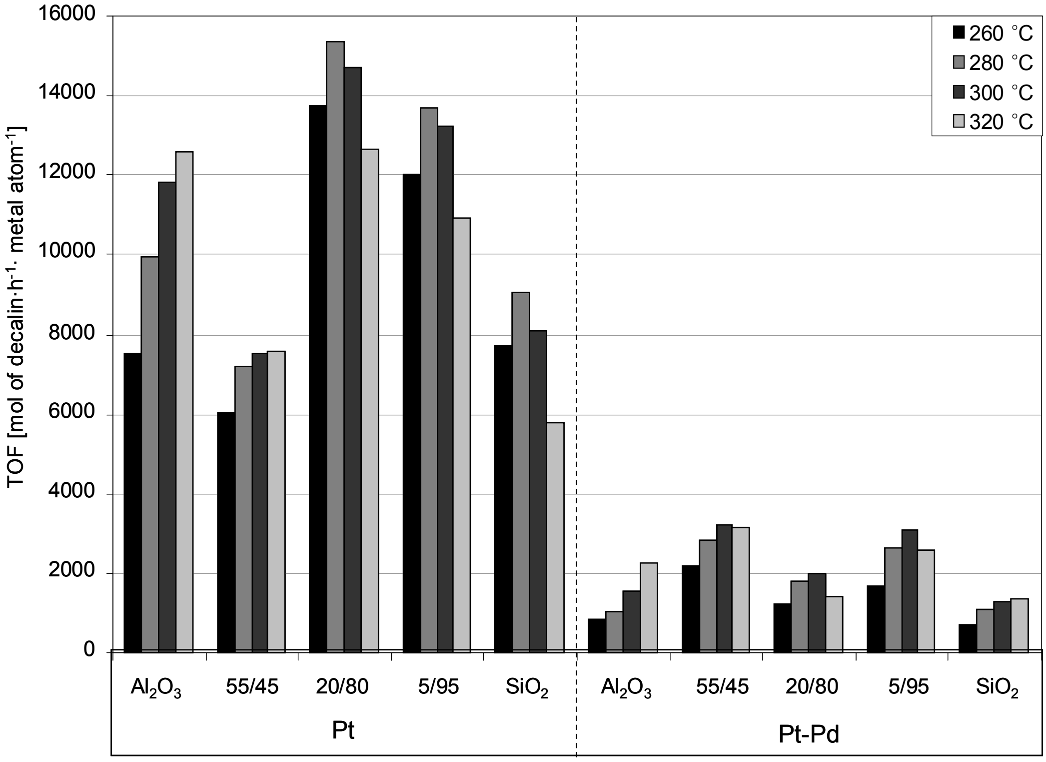

Figure 3. Overview of tetralin hydrogenation by oxide supported Pt and Pt-Pd catalysts.

The catalytic activity at 260°C after 24 hours could not be correlated with an obvious property of the support composition. Nevertheless it is interesting to note that the ASA supported catalysts were more active than Pt-Pd/Al_2O_3 and Pt-Pd/SiO_2 that do not contain Brønsted acid sites and that Pt-Pd/ASA (55/45) was very active. The latter support led to a poor activity when supporting Pt particles. TEM analysis in Chapter 2 showed that Pt-Pd supported on ASA (55/45) led to the smallest alloy clusters with an average particle size of 1.4 nm compared to 1.6 nm for Pt-Pd/ASA (5/95) and 1.8 nm for Pt-Pd/ASA (20/80). Therefore the activity ranking of the Pt-Pd/ASAs can be correlated with the bimetallic cluster dispersion. Moreover, only very small metal clusters are exposed to significant metal-support interactions leading to an improved tetralin hydrogenation performance [4].

All oxide supported bimetallic Pt-Pd catalysts were 3-10 times less active than their monometallic Pt counterparts. Furthermore the observed c*is* - to *trans* – decalin ratios in the product of tetralin hydrogenation by Pt-Pd were much smaller compared to the formed product ratio over Pt. Apparently tetralin adsorbs weaker on the bimetallic metal alloy leading to a lower activity and a promoted formation of the thermodynamically favored *trans* - isomer.

3.2 Hydrogenation of tetralin by oxide supported Pt and Pt-Pd catalysts in the presence of quinoline

The presence of 400 ppm N as quinoline in the feed led to a 3 to 8 times lower activity of the Pt catalysts as compared to tetralin hydrogenation with clean feed after 24 hours at 260°C (Figure 4).

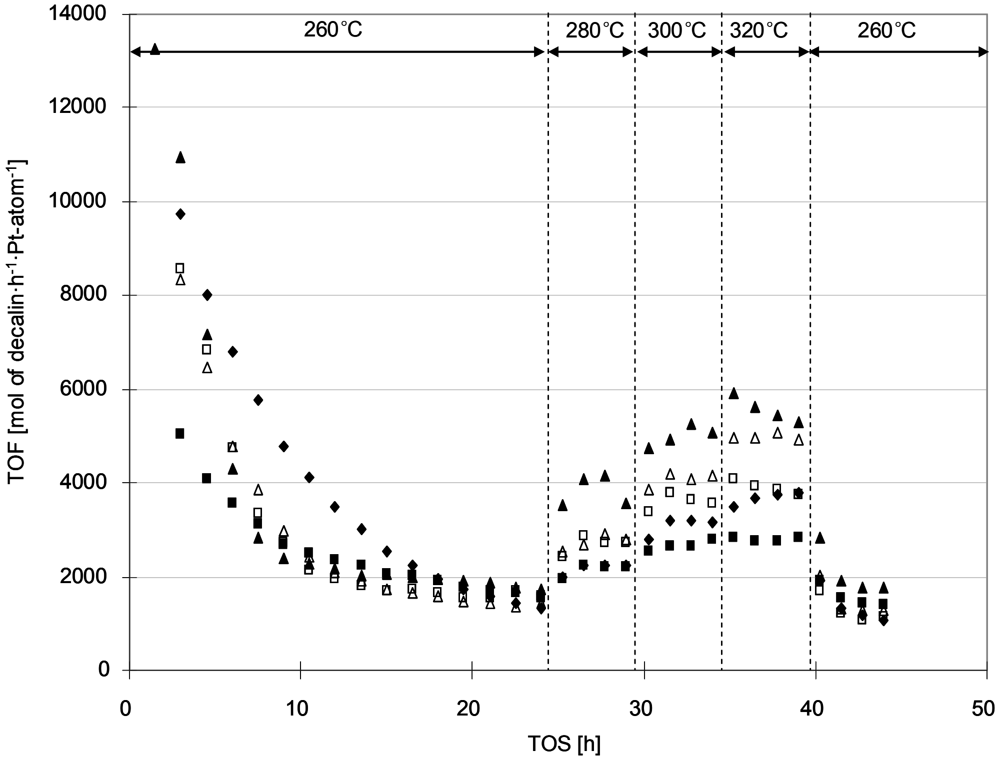

Figure 4. Hydrogenation of tetralin in the presence of quinoline (400 ppm N) over Pt/Al_2O_3 (♦), Pt/ASA (55/45) (■), Pt/ASA (20/80) (▲), Pt/ASA (5/95) (△), and Pt/SiO_2 (□) in the temperature range from 260 – 320°C (50 bar, WHSV = 270.6 h^{-1}).

Neutralization of the support by the basic quinoline inhibiting metal-support interactions as described in Chapter 3 led to an equal activity of all oxide supported Pt catalysts after 24 hours continuous deactivation at 260°C. Also the observed *cis*- to *trans*-decalin ratios were quite uniform among the monometallic Pt catalysts as depicted in Figure 5. By increasing the temperature to 280 – 320°C the catalyst performances drifted apart leading to the same Pt catalyst activity ranking as observed in the absence of catalyst poisons. Satterfield *et al* presented a detailed reaction network for the hydrogenation of quinoline [6]. At the present reaction conditions not only the hydrogenated quinoline product tetrahydroquinoline, but also the saturated consecutive product decahydroquinoline and denitrogenated ring opening products were formed and identified by GC-MS. The production of theses ring opening products from decahydroquinoline was favored by higher temperatures and by Pt catalysts that also showed a better performance in tetralin hydrogenation. Apparently ring opening accompanied by ammonia formation led to less catalyst poisoning resulting consequently to the same sequence of catalyst activity as observed for clean feed tetralin hydrogenation.

In contrast to the absence of quinoline no decrease in the tetralin hydrogenation activity took place with all Pt catalysts when increasing the temperature from 300 to 320°C. It seems that the favored catalyst surface removal of N-poison overlaps the enhanced catalyst deactivation at higher temperatures.

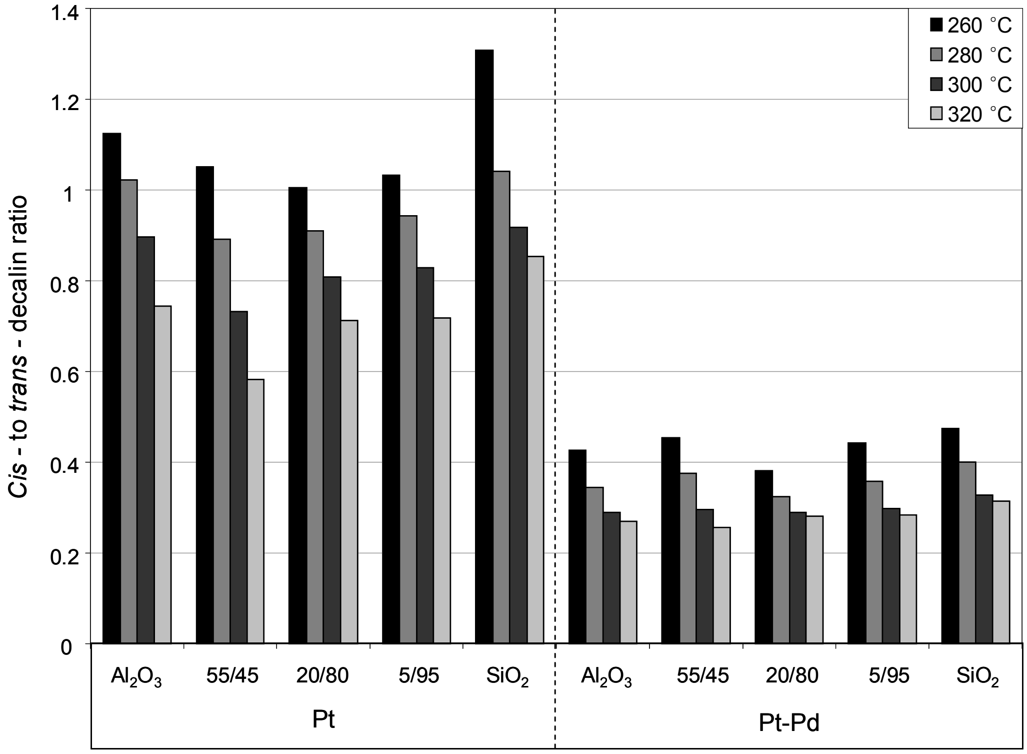

Figure 5. *Cis* - to *trans* – decalin ratios over oxide supported Pt and Pt-Pd catalysts in the presence of quinoline.

All Pt-Pd catalysts were less active than their monometallic Pt counterparts in the presence of N-poison, but did not perform equally at 260°C after 24 hours as shown in Figure 6. Their small activity was again accompanied with low *cis* - to *trans*–decalin ratios of 0.25 - 0.45 between 260 and 320°C proving the low tetralin adsorption strength on the oxide supported bimetal alloys (see Figure 5).

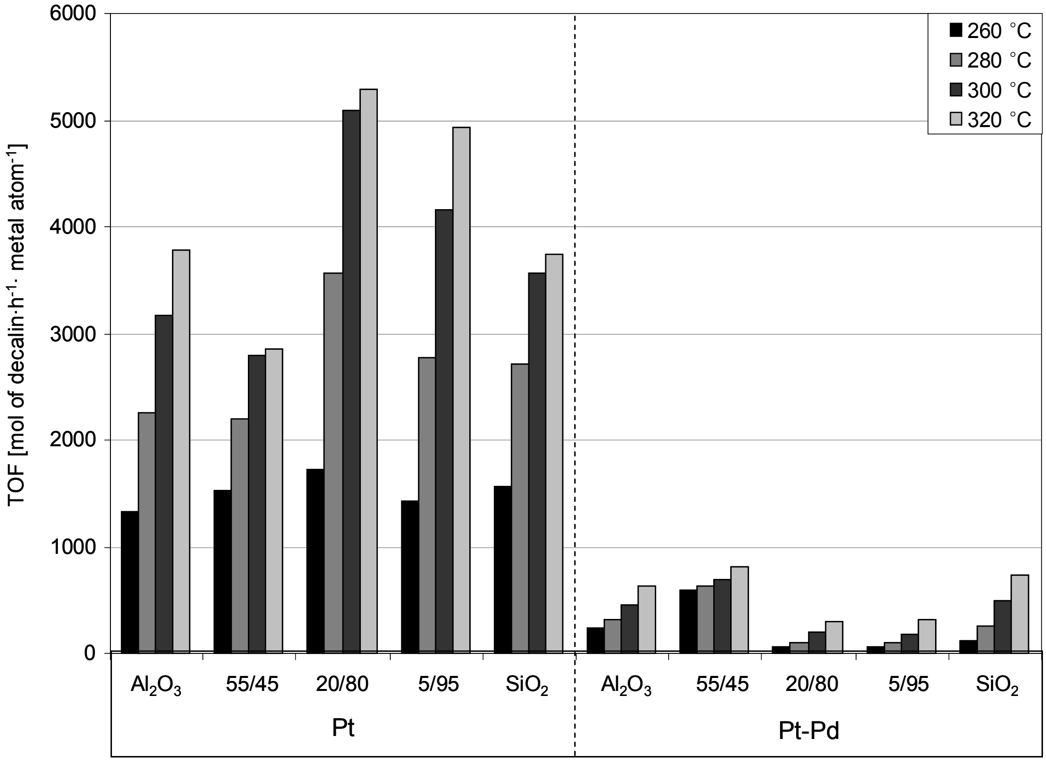

Figure 6. Overview of tetralin hydrogenation in the presence of quinoline by oxide supported Pt and Pt-Pd catalysts.

Pt-Pd/ASA (55/45) was again the catalyst with the highest activity, which probably originated from the best dispersed metal clusters among all present Pt-Pd catalysts and therefore to a larger fraction of accessible catalytic active sites.

3.3 Hydrogenation of tetralin by oxide supported Pt and Pt-Pd catalysts in the presence of dibenzothiophene

The sulfur tolerance of the alumina, ASA and silica supported Pt and Pt-Pd catalyst was studied by adding 100 ppm S as dibenzothiophene (DBT) to the tetralin feedstock. The turnover frequencies vs. time on stream (TOS) over the studies Pt and Pt-Pd catalysts are presented in Figure 7 and Figure 9, respectively.

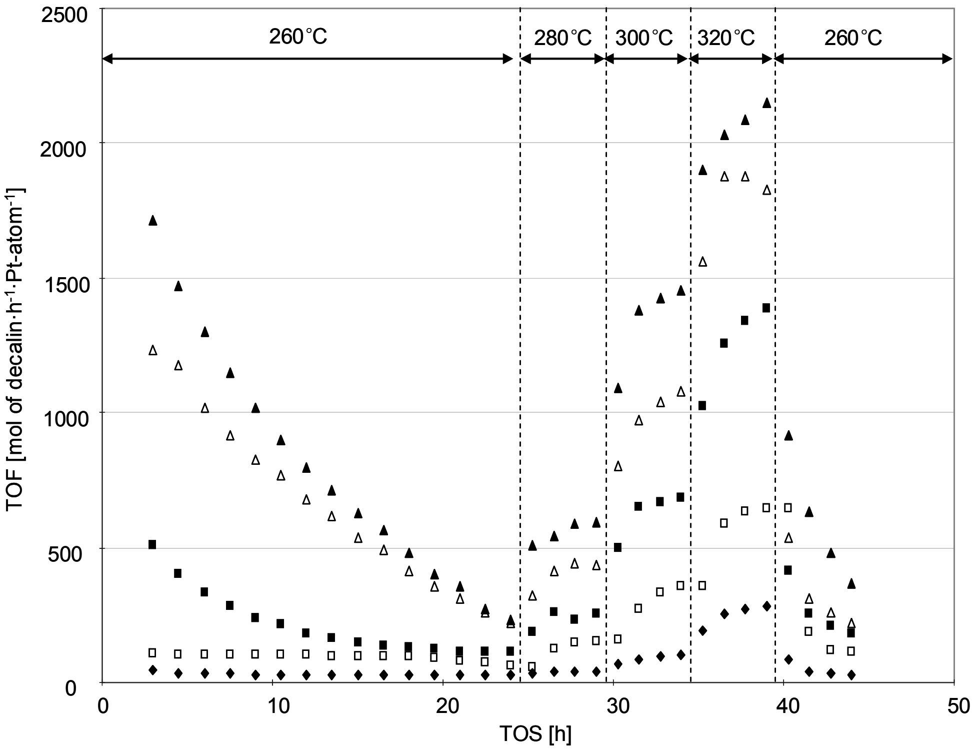

Figure 7. Hydrogenation of tetralin in the presence of dibenzothiophene (100 ppm S) over Pt/Al_2O_3 (♦), Pt/ASA (55/45) (■), Pt/ASA (20/80) (▲), Pt/ASA (5/95) (△), and Pt/SiO_2 (□) in the temperature range from 260 – 320°C (50 bar, WHSV = 77.3 h^{-1}).

The activities in tetralin hydrogenation of the Pt catalysts decreased up to 2 orders of magnitude when S-poison was present in the feed. It is known that sulfur adsorbs strongly on noble metal surfaces hindering the adsorption of aromatic molecules such as tetralin. Hydrogenation on Brønsted acid sites at the perimeter of Pt clusters was proposed in Chapter 3 as an additional minor hydrogenation pathway that becomes significant when the sulfur is blocking highly active metal active sites. The present experiments were conducted at 260 -320°C, which was 100°C higher than the experiments in Chapter 3, but still the catalyst activities could be correlated with the concentration of BAS calculated in Chapter 1. Pt/ASA (20/80) with the highest BAS concentration (42 μmol/g) was the most active catalyst followed by Pt/ASA (5/95) (35 μmol/g), Pt/ASA (55/45) (23 μmol/g), Pt/SiO_2 (0 μmol/g) and Pt/Al_2O_3 (0 μmol/g).

In contrast to tetralin hydrogenation with clean and N-poisoned feed, the activity of all Pt catalysts was clearly enhanced when the temperature was increased in the whole examined temperature range. Upon a temperature step increase of 20K the catalysts even showed a further continuous activity increase for about another 5 hours. This result could be ascribed to a lower sulfur adsorption/desorption equilibrium at higher temperatures leading to weaker metal active site poisoning and continuous removal of strongly metal adsorbed sulfur.

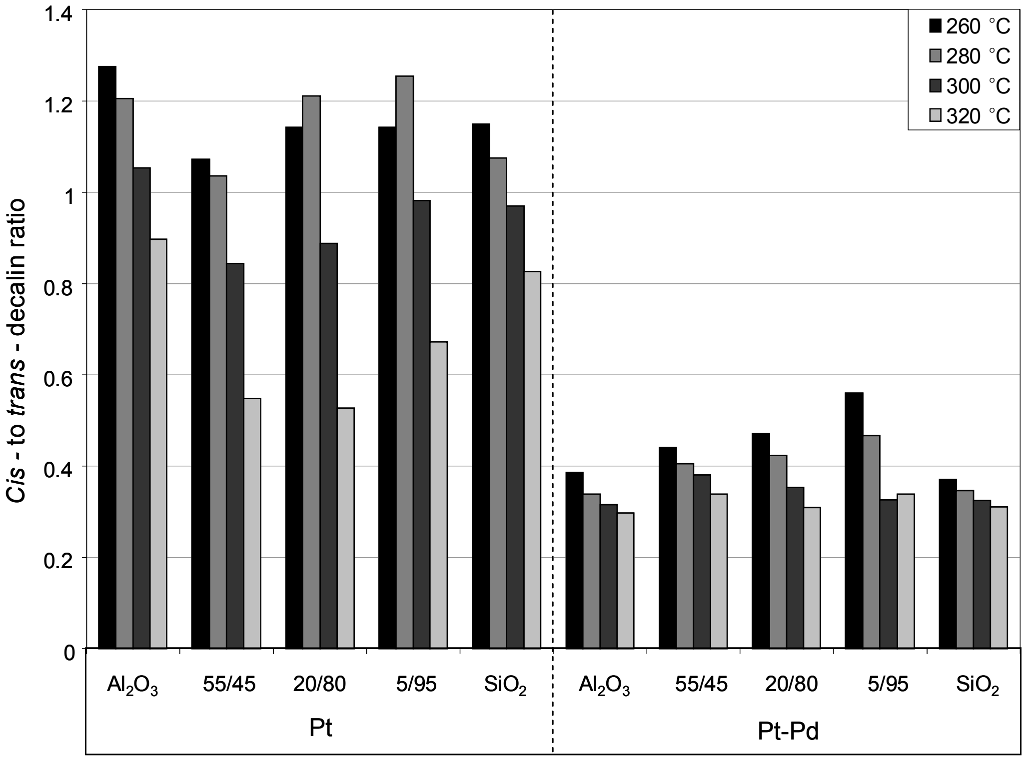

Figure 8. *Cis* - to *trans* – decalin ratios over oxide supported Pt and Pt-Pd catalysts in the presence of dibenzothiophene.

The presence of 100 ppm S as DBT in the feed led also to a low activity of all oxide supported Pt-Pd catalysts, which was again even lower than that observed for the monometallic Pt catalysts accompanied with low *cis*- to *trans*- decalin ratios of 0.3 – 0.6 (Figure 8 and Figure 9). Among the Pt-Pd samples, Pt-Pd/ASA (55/45) exhibiting the smallest Pt-Pd clusters revealed an extraordinary high sulfur tolerance.

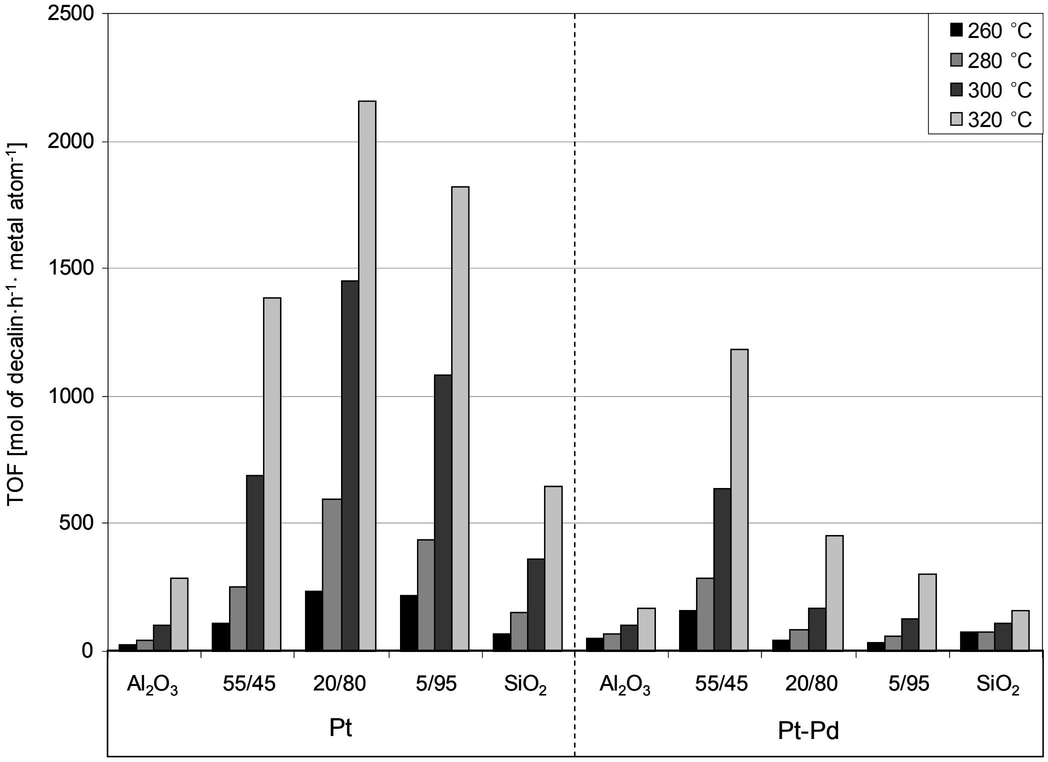

Figure 9. Overview of tetralin hydrogenation in the presence of dibenzothiophene by oxide supported Pt and Pt-Pd catalysts.

3.4 Hydrogenation of tetralin by oxide supported Pt and Pt-Pd catalysts in the presence of quinoline and dibenzothiophene

When both, S- and N-poison was present in the feedstock, fast deactivation of the Pt and Pt-Pd catalysts occurred during the first 6 hours leading to marginal tetralin hydrogenation activities at 260°C (see Figure 10 and Figure 12)

Apparently quinoline is neutralizing the support acid sites whereas sulfur strongly blocks active metal centers.

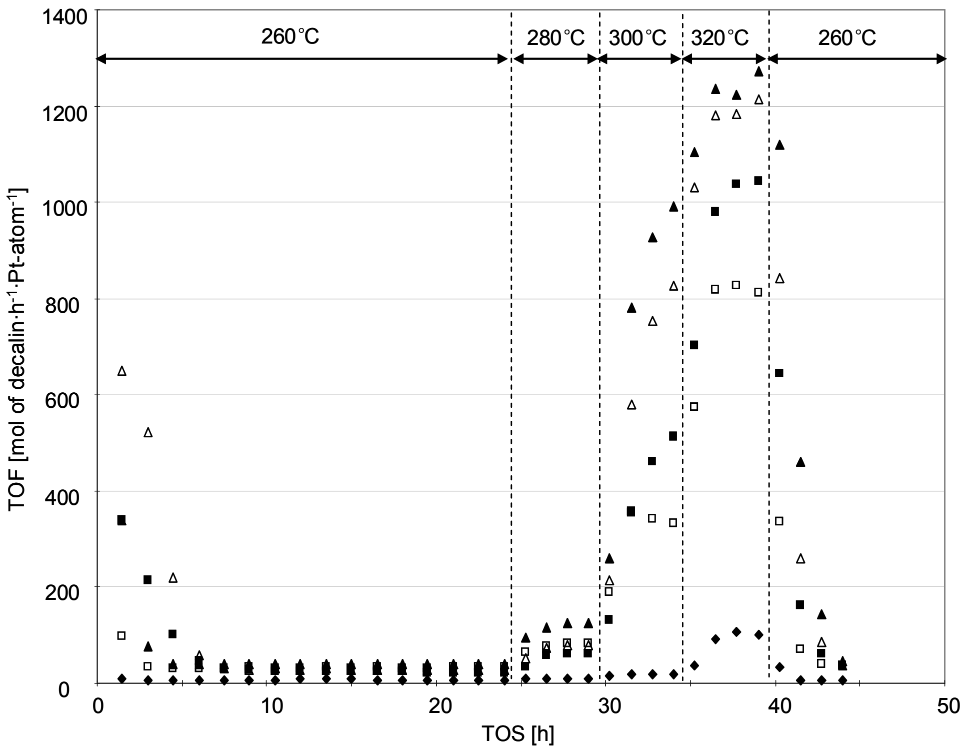

Figure 10. Hydrogenation of tetralin in the presence of dibenzothiophene (100 ppm S) and quinoline (20 ppm N) over Pt/Al_2O_3 (♦), Pt/ASA (55/45) (■), Pt/ASA (20/80) (▲), Pt/ASA (5/95) (△), and Pt/SiO_2 (□) in the temperature range from 260 – 320°C (50 bar, WHSV = 32.4 h^{-1}).

By increasing the temperature in steps of 20K up to 320°C a tremendous tetralin hydrogenation activity increase was observed. Similarly to the experiments with solely N- or S-poison it can be assumed that at higher temperatures quinoline was denitrogenated to ring opening products and ammonia, whereas sulfur adsorbed weakly due to a lower adsorption/desorption equilibrium constant. Again, the activity of the Pt/ASA catalysts could be correlated to their BAS concentrations showing the importance of the minor tetralin hydrogenation pathway as described in detail in Chapter 3.

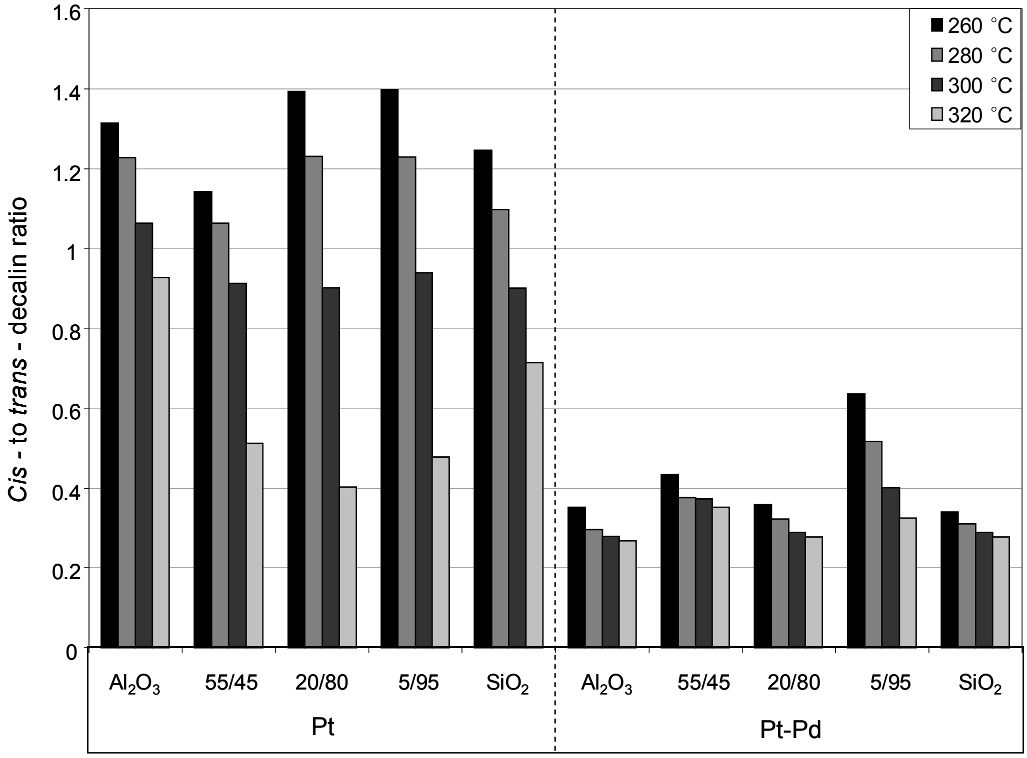

Figure 11. *Cis*- to *trans*–decalin ratios over oxide supported Pt and Pt-Pd catalysts in the presence of dibenzothiophene and quinoline.

Similarly to all previous cases the oxide supported Pt-Pd catalysts showed a poor aromatics hydrogenation performance in addition to small *cis*- to *trans*- decalin ratios compared to monometallic Pt in the presence of mixed poison (100 ppm S and 20 ppm N), which is shown in Figure 11and Figure 12 .

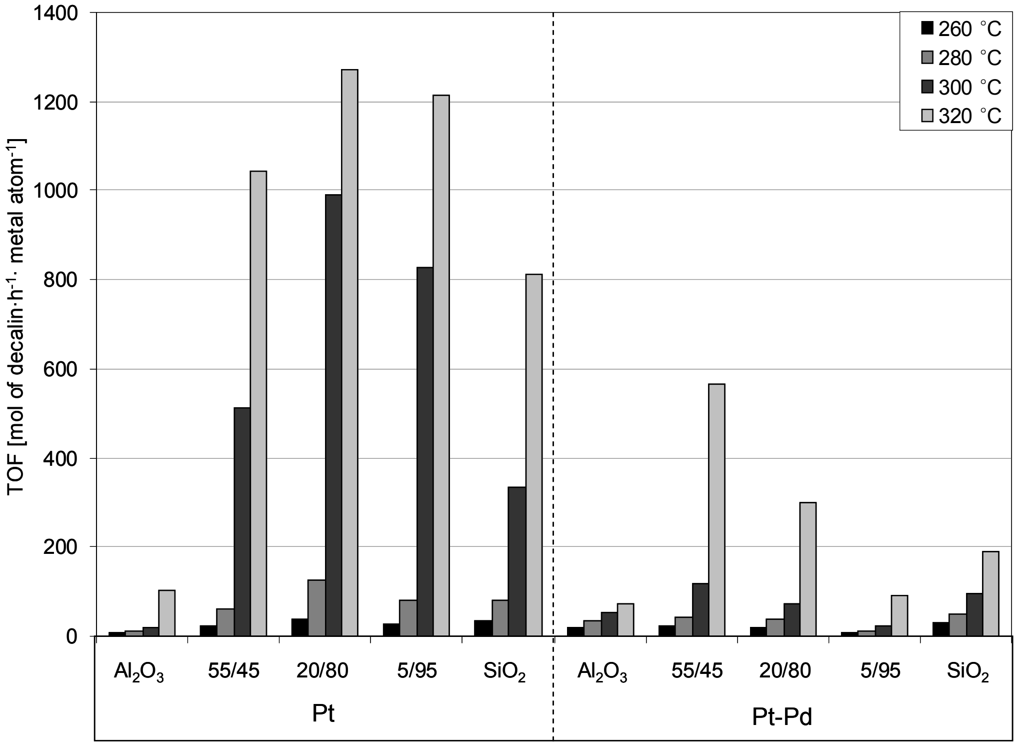

Figure 12. Overview of tetralin hydrogenation in the presence of dibenzothiophene and quinoline by oxide supported Pt and Pt-Pd catalysts.

3.5 Reversibility of Pt and Pt-Pd/ASA poisoning

In order to explore directly the poisoning effect of sulfur and nitrogen compounds on the Pt and Pt-Pd/ASA performance the catalysts were firstly exposed to clean tetralin feed for 24 hours followed by the addition of catalyst poisons (400 ppm N, 100 ppm S or 20 ppm N + 100 ppm S) for 20 hours. The extent of activity regain was further monitored by subsequent clean feed hydrogenation for another 24 hours (Figure 13 and Figure 14).

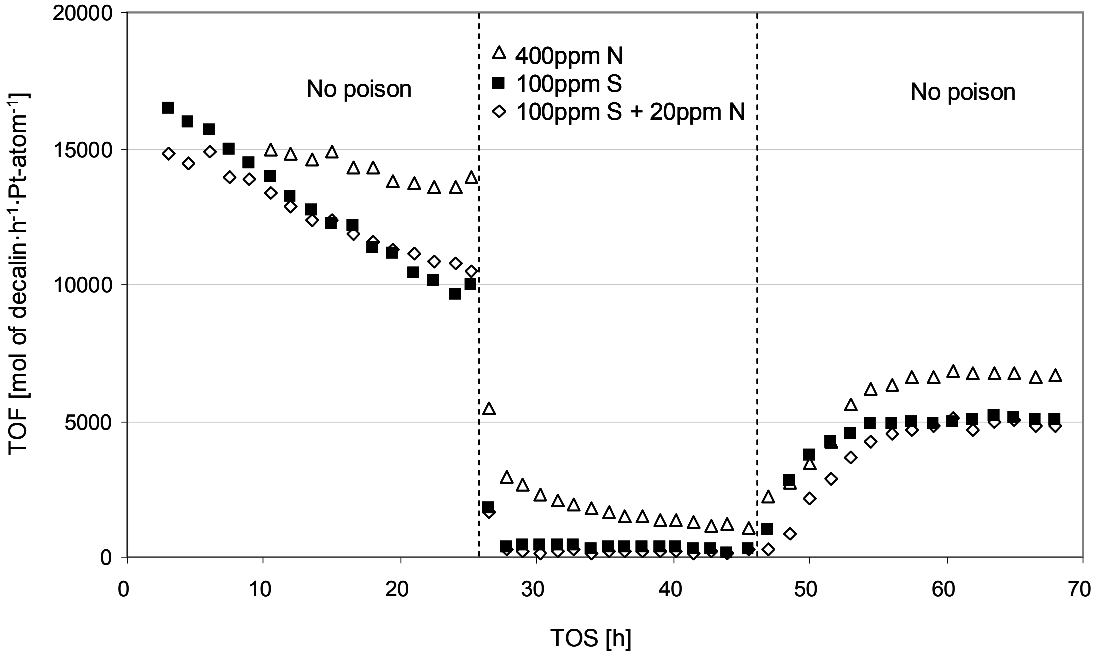

Figure 13. Hydrogenation of tetralin in the absence and presence of quinoline (△), dibenzothiophene (■) and both poisons (◇) over Pt/ASA (20/80) at 260° C (50 bar, WHSV = 404.7 h^{-1}).

Sulfur in the feedstock decreased the hydrogenation activity of Pt/ASA (20/80) drastically. A further addition of 20 ppm N as quinoline led to an almost inactive catalyst, whereas with 400 ppm N without sulfur in the feed Pt/ASA (20/80) could remain a significant fraction of its initial activity.

In the second phase of clean feed tetralin hydrogenation a large part of the catalyst activity could be recovered showing the reversibility of S- and N-poisoning. A stable catalyst activity could be achieved after 8 to 12 hours. The rate of catalyst regeneration was somewhat slower after nitrogen poisoning compared to only sulfur poisoning, which most probably originated from more nitrogen containing carbon deposits initiated by the strong base quinoline.

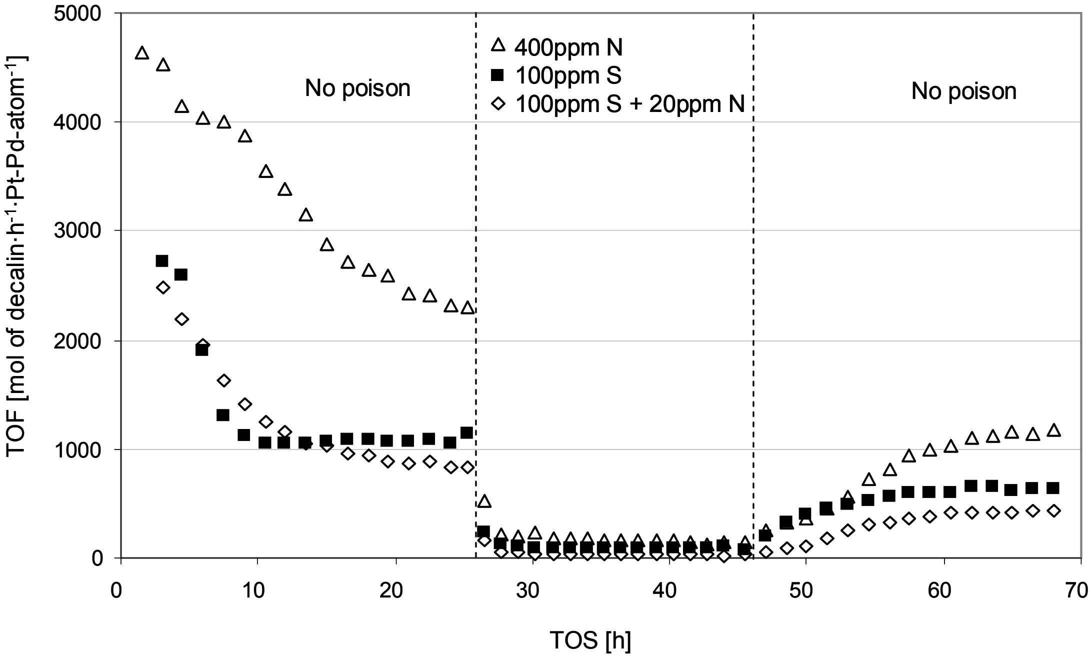

Figure 14. Hydrogenation of tetralin in the absence and presence of quinoline (△), dibenzothiophene (■) and both poisons (◇) over Pt-Pd/ASA (20/80) at 260° C (50 bar, WHSV = 404.7 h^{-1}).

The aromatics hydrogenation activity of Pt-Pd/ASA (20/80) was severely affected by sulfur poisoning similarly to monometallic Pt. The poisoning effect of quinoline on the alloy was even stronger as for monometallic Pt due to the lower ring opening and hydrodenitrogenation ability of Pt-Pd. This also results in a longer catalyst regeneration time after the subsequent clean feed hydrogenation for 24 hours.

3.6 Sulfur tolerance of Pt and Pt-Pd/ASA

The tolerance towards sulfur of Pt and Pt-Pd/ASA(20/80) was studied by adding 100 and 500 ppm sulfur as dibenzothiphene to the feedstock. The catalysts performances in the hydrogenation of tetralin at 260 – 320°C are depicted in Figure 15.

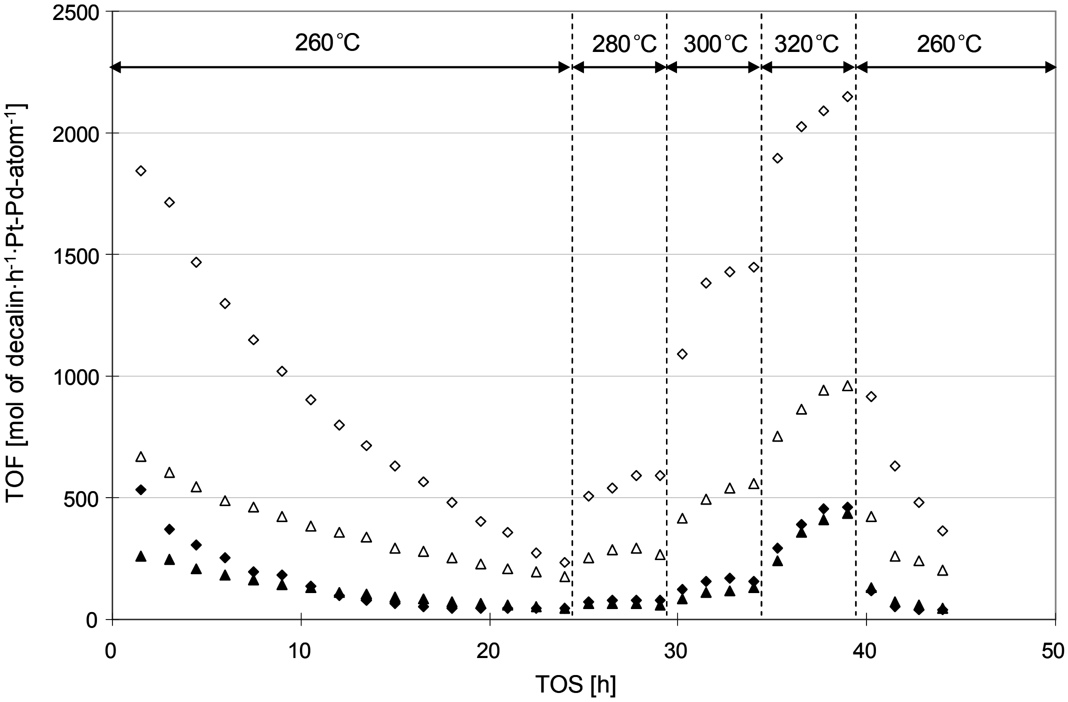

Figure 15. Hydrogenation of tetralin in the presence of dibenzothiophene over Pt/ASA (20/80) (100 (◇) and 500 (△) ppm S) and Pt-Pd/ASA (20/80) (100 (♦) and 500 (▲) ppm S) at 260 - 320° C (50 bar, WHSV = 77.3 h^{-1}).

Pt catalysts showed higher aromatics hydrogenation activity compared to Pt-Pd no matter 100 ppm or 500 ppm S sulfur were present in the feedstock. Nevertheless it is remarkable that an increase to higher sulfur levels did not influence the activity of the bimetallic alloy significantly, but clearly led to further Pt-poisoning.

3.7 Role of the Brønsted acid sites

An additional Pt/ASA (38/62) catalyst was prepared and impregnated with an aqueous solution of $CsNO_3$ (30 mg Cs/g catalyst) in order to explore directly the role of BAS in aromatics hydrogenation.

This procedure hardly affected the catalyst's toluene hydrogenation activity (1 bar H_2/gasphase) as the temperature required for 40% conversion decreased only from 64 (parent Pt/ASA) to 59ºC (Cs-exchanged), while the temperature required for 40% conversion of n-heptane (30 bar H_2/gasphase) to iso-heptanes had to be increased from 353 (parent Pt/ASA) to 419ºC (Cs-exchanged). As the hydrogenation of toluene is an exclusively metal catalyzed reaction and n-heptane isomerization takes place over acid sites it can be concluded that the Pt clusters were hardly affected by the Cs loading process, while the acidity was effectively killed.

The successful catalyst synthesis for our purpose was further confirmed by TEM, CO and pyridine adsorption IR spectroscopy. Cs impregnation of Pt/ASA (38/62) did neither influence the mean Pt cluster diameter of 0.9 nm nor the amount and wavenumber of linearly adsorbed CO at 2075 cm^{-1} upon 15 min evacuation at 10^{-6} mbar. On the other hand pyridine adsorption revealed that the Cs treatment led to a dramatic loss of BAS from 26 to only 3 µmol/g, whereas the LAS concentration of 100 µmol/g remained constant.

Cs-Pt/ASA (38/62) and the parent Pt catalyst were tested in the hydrogenation of tetralin in the absence and presence of quinoline and DBT at the same reaction conditions as for all other oxide supported noble metal catalysts in this study. The activity of Cs-Pt/ASA (38/62) was set into relation with the TOF of Pt/ASA (38/62) and is displayed in Figure 16.

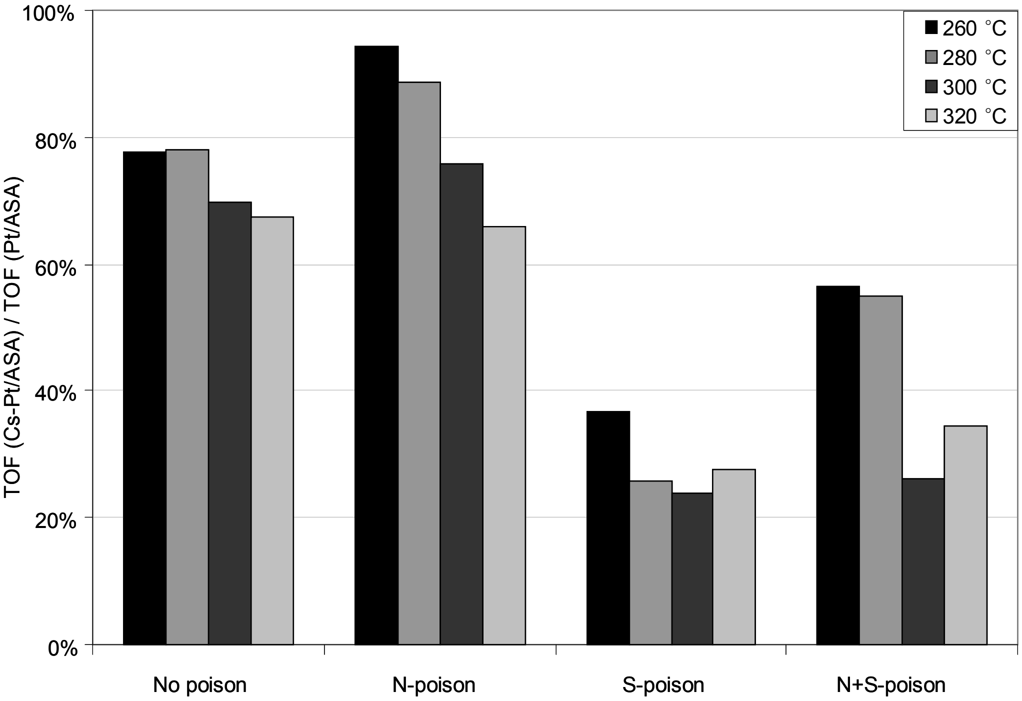

Figure 16. Percentage of the tetralin hydrogenation TOF of Cs-Pt/ASA (38/62) vs. Pt/ASA (38/62) in the presence and absence of dibenzothiophene and quinoline (50 bar, 260 – 320°C).

At 260°C Cs-Pt/ASA reached 78% of the activity of Pt/ASA. Therefore, in that case up to 22% of the aromatics hydrogenation activity can be related to tetralin saturation on BAS in the vicinity of Pt clusters that are still able to dissociate hydrogen molecules. In the presence of basic quinoline the fraction of aromatics that could be hydrogenated via this alternative route was reduced to 5% revealing the neutralization of BAS in Pt/ASA. At higher temperatures this fraction was increased up to 34 % at 320°C, similarly to the clean feed experiment, which confirms BAS freeing by hydrodenitrogenation of decahydroquinoline.

Only 36% of the Pt/ASA performance was achieved when the Pt particles were strongly poisoned by sulfur at 260°C. Here two thirds of tetralin hydrogenation took place on BAS showing the importance of this pathway in the presence of DBT. This fraction was decreased to 44% when BAS were neutralized by 20 ppm N as quinoline. Increasing the temperature from 300 to 320°C, the lack of BAS in Cs exchanged Pt/ASA could be partially superposed, probably due to weaker Pt-S bonding at higher temperatures resulting in a higher fraction of Pt catalyzed hydrogenation.

3.8 Characterization of the used catalysts

The concentration of sorption sites on the support and on the metal particles was probed by IR spectra of adsorbed pyridine and CO, respectively. The metal particles sizes were determined by transmission electron microscopy.

The IR spectra of spent Pt/ASA (5/95) after CO adsorption are shown in Figure 17.

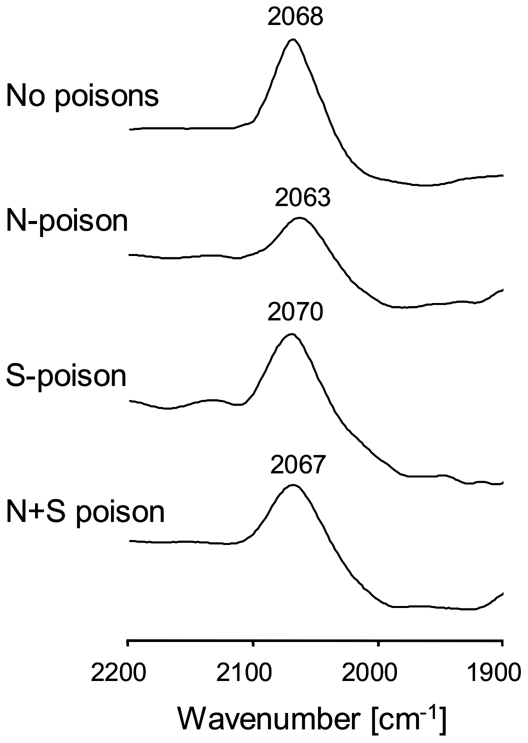

Figure 17. CO adsorption on spent Pt/ASA (5/95).

The adsorption capacity of linearly adsorbed CO at 2063 – 2070 cm^{-1} on Pt was drastically reduced during tetralin hydrogenation in the absence and presence of poisons. Less than 6 % of the original Pt surface was available for CO adsorption. It should be mentioned here that higher WHSV and longer time on stream led to substantial higher coverage of the metal clusters.

In order to explore the role of particle sintering in this process fresh and used Pt and Pt-Pd/ASA (5/95) catalysts were analyzed by transmission electron microscopy. In Figure 18 only representative TEM pictures of used Pt-Pd/ASA (5/95) are shown as the fresh catalysts and the used monometallic Pt catalysts were presented in Chapter 2 and 3, respectively.

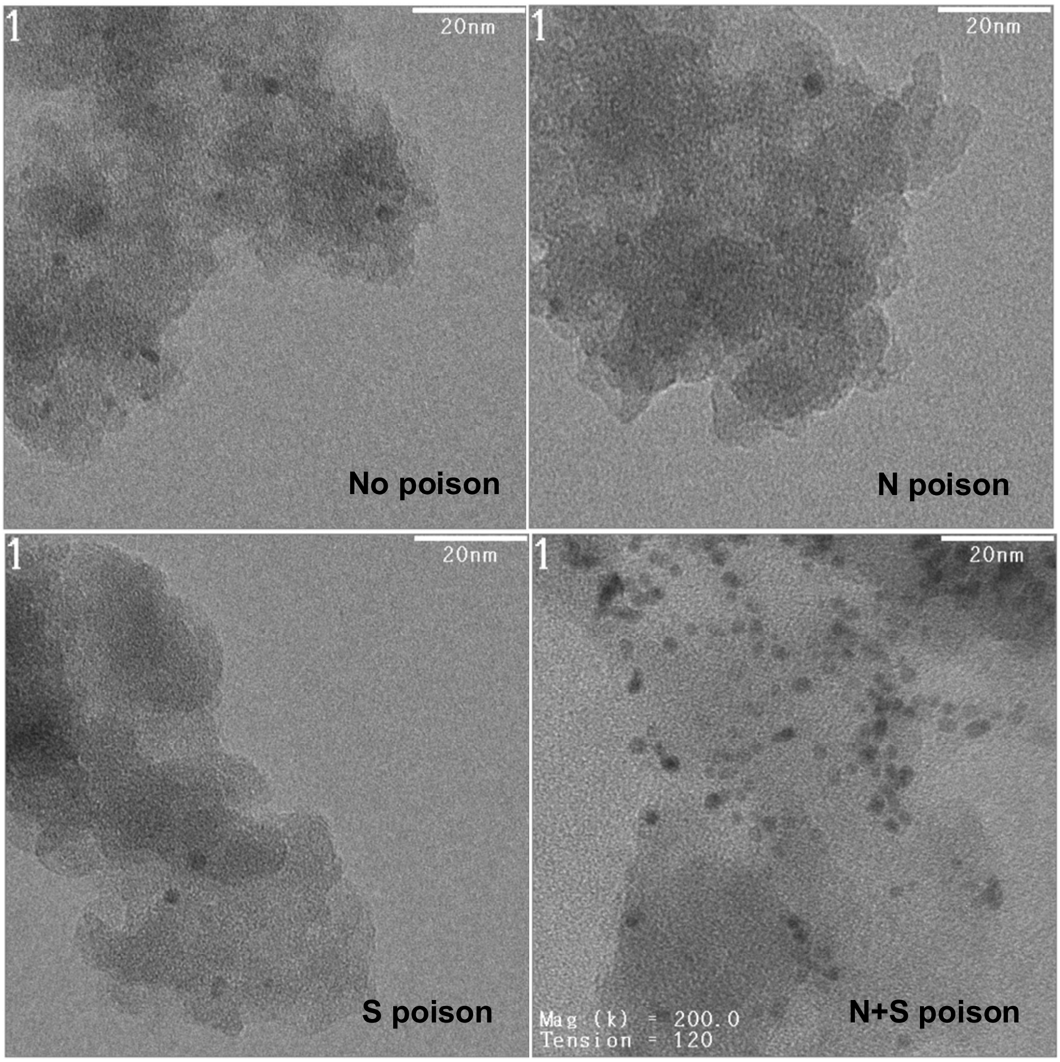

Figure 18. TEM micrographs of Pt-Pd/ASA (5/95) before and after the hydrogenation of tetralin in the presence and absence of DBT and quinoline.

By counting 300 Pt-Pd particles per catalyst, a histogram was generated and the average cluster sizes were calculated. Unlike monometallic Pt the average Pt-Pd particle size did not increase. The alloys in Pt-Pd/ASA (5/95) kept their average particle size of 1.6 nm after tetralin hydrogenation in the absence and presence of DBT and quinoline.

Pyridine adsorption followed by IR spectroscopy on the used catalyst samples was carried out in order to probe the effect of the N- and S-compounds on the supported platinum catalysts during the hydrogenation of tetralin. The IR spectra of pyridine adsorbed on the spent Pt/ASA (5/95) catalysts are presented and compared to the spectrum of adsorbed pyridine on the fresh catalyst in Figure 19.

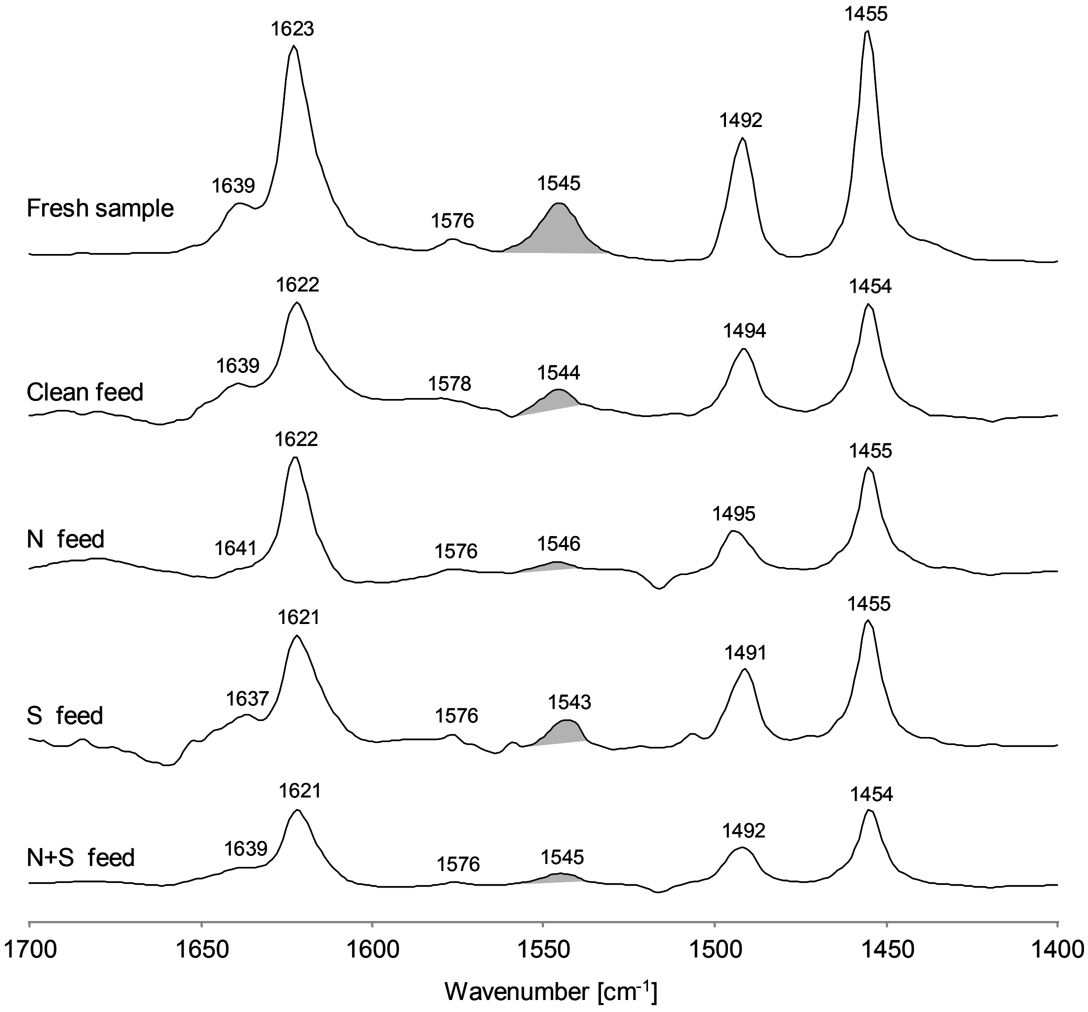

Figure 19. Pyridine adsorption IR study of spent and fresh Pt/ASA (5/95) samples.

Table 1. Summary of the results of pyridine adsorption IR spectroscopy of fresh and used Pt/ASA (5/95)

Catalyst	Acid site concentration (μmol/g)		Remaining acidity (%)	
	BAS	LAS	BAS	LAS
Pt/ASA (5/95)	35	90	-	-
Clean feed	15	46	42.9	51.1
N feed	3	42	8.6	46.7
S feed	15	45	42.9	50.0
N+S feed	6	28	17.1	31.1

After pyridine adsorption on the activated catalysts, bands at 1545 and 1455 cm^{-1} were assigned to pyridinium ions and coordinatively-bonded pyridine, respectively [3]. The catalyst sample used for tetralin hydrogenation in the presence of DBT showed no lower intensity of the band at 1545 cm^{-1} (adsorption on BAS) compared to the concentration of pyridine observed on the used catalysts after reaction with clean feed. Thus, DBT did not block the acid sites of ASA (5/95) to a higher extend than coke formed in tetralin conversion. In contrast, the adsorption of pyridine was strongly reduced after hydrogenation of tetralin in the presence of quinoline. Thus, we conclude that quinoline adsorbs strongly on Brønsted and Lewis acid sites.

4 Discussion

4.1 Catalyst deactivation of Pt and Pt-Pd catalysts

Deactivation of the catalyst activity as a function of time on stream is a phenomenon that is always found when tetralin or naphthalene hydrogenation is studied [2, 7-11].

Rautanen et al. assumed coke formation to be the main reason for the deactivation of Ni/Al_2O_3, whereas the deactivation rate was independent of the hydrogen pressure [8]. Carboneceous deposits were confirmed to be the main reason for the deactivation of Au-Pt-Pd/ASA, Pt-Pd/ASA and Pt-Pd/MWNT by TGA analysis limiting the availability of hydrogen on metal sites [9].

Furthermore, it has been found that a high Pt electron deficiency leads to strong adsorption of aromatics, which can inhibit hydrogen dissociation resulting in decreasing hydrogenation activities [12, 13]. Especially naphthalene, which is always present as a trace in tetralin feeds and that is always produced by dehydrogenation of tetralin at high temperatures, was found to be a strong inhibitor for aromatics hydrogenation over Pt/TiO_2 [13]. Consequently, the sudden decrease of all silica containing Pt catalysts activities, when increasing the reaction temperature from 300 to 320°C, is speculated to be a result of the observed enhanced naphthalene formation in the present work. Recently, Infantes-Molina et al. also found that high reaction temperatures above 300°C lead do a lower tetralin hydrogenation activity combined with an increased naphthalene formation [14].

Hydrogenation is known to be a structure insensitive reaction [15, 16] and, thus, the activity of hydrogenation metal catalysts is generally favored by high metal dispersions. In the present study all Pt and Pt-Pd catalysts exhibit an initial strong deactivation followed by a continuous lower deactivation with TOS. TEM and EXAXS reveal that Pt clusters supported on ASA (5/95) experience particle growth from 0.8 to 1.2-1.6 nm during tetralin hydrogenation in the absence and presence of quinoline whereas the mean noble metal cluster size of 1.6 nm in bimetallic Pt-Pd/ASA (5/95) stays constant during the reaction. Costa Augusto et al. also found that the addition of Pd to Pt supported on Y zeolites prevents alloy sintering in tetralin hydrogenation [17]. Consequently the main reason for the catalysts deactivation in our study does not originate from noble metal particle sintering as proposed in other publications [14, 18], but from the formation of carbonaceous deposits on the supports and even more significant from metal particle blocking by S, N and also C containing compounds. The high coverage of the Pt particles supported on ASA (5/95) is demonstrated by CO adsorption IR spectroscopy showing that less than 6% of the metal surface is accessible for CO after tetralin hydrogenation. Moreover, the detailed EXAFS analysis of used Pt/ASA (5/95) in Chapter 3 clearly shows the presence of Pt-C, Pt-N and strong Pt-S bonds.

The 38 atoms Pt cluster model shown in Figure 20 with a diameter of 1.2 nm covered by 6 benzene rings shows that it is realistic that in average 1 Pt atom has 1 C neighbor and only a small part of the Pt free surface is available for further adsorption. This model describes very well the findings of TEM, EXAFS and CO adsorption IR of used Pt/ASA (5/95) after tetralin hydrogenation.

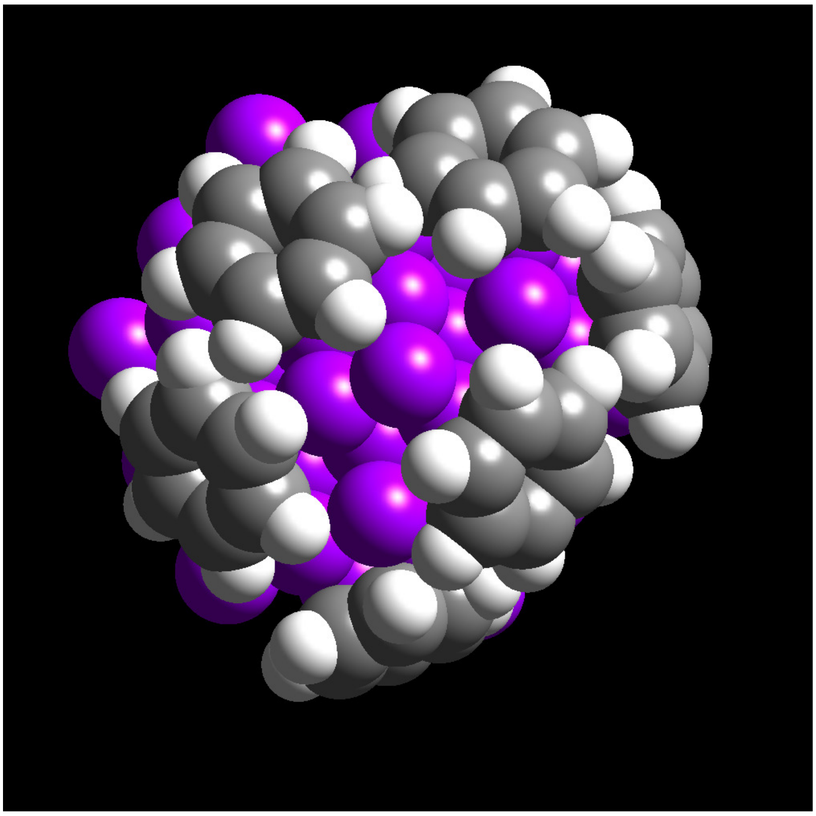

Figure 20. Model of benzene adsorbed on a Pt cluster.

It was already shown in Chapter 3 with Pt/ASA (55/45) that tetralin hydrogenation leads to a significant decrease of Brønsted and Lewis acid sites that is substantially larger when basic quinoline is present in the feedstock. Here similar results are obtained by pyridine adsorption IR for Pt/ASA (5/95). The declined acidity of the ASA supported metal catalysts that leads to more neutral carriers reducing metal-support interactions is proposed to be another, but less important reason for the present catalyst deactivation. It should be noted that also neutral Pt/SiO_2 shows substantial deactivation during the hydrogenation reaction with time on stream.

4.2 Role of bimetallic Pt-Pd formation

It has been widely reported that Pt is more active in the hydrogenation of aromatics [19] and specifically in the hydrogenation of tetralin and naphthalene [2, 20, 21] compared to Pd accompanied by higher *cis*- to *trans*- decalin ratios [22]. It has been concluded from the characterization results by CO adsorption IR and XANES in Chapter 2 and also found in other publications [12] that Pt-Pd particles are Pd surface enriched leading to similar *cis*- to *trans*- decalin ratios as observed for monometallic Pd catalysts [2]. Very likely the low *cis*- to *trans*- decalin ratios over Pt-Pd compared to Pt can be attributed to the low tetralin adsorption strength on Pd. According to the reaction model of Weitkamp [23] the consecutive desorption and re-adsorption of the partially hydrogenated intermediate, $\Delta^{1,9}$ – octalin is facilitated in that case.

Moreover, the interaction of hydrogen on platinum and palladium surfaces differs significantly despite their similar structure and proximity in the periodic table. According to density functional theory calculations, stable H_2 coordination occurs on Pt 1-fold atop sites and hollow sites, whereas H-Pd 1-fold atop site bonds were calculated to be very weak compared to hydrogen coordination on very stable Pd 3-fold hollow sites [24, 25]. Consequently more adsorbed hydrogen is available for reaction when Pt is used as a catalyst.

4.3 Tetralin hydrogenation in the presence of dibenzothiophene and quinoline

The resistance to catalyst poisons such as quinoline and dibenzothiophene during the hydrogenation of tetralin depends mainly on the nature of the support and the type, electronic state and size of the noble metal clusters. In Chapter 3 the catalytic hydrogenation of tetralin over Pt/ASA catalysts in the presence of N- and S-poisons has been explored at relatively low temperatures (160 – 190°C). Two types of active sites for the catalytic hydrogenation were identified: (1) those on the metal particles and (2) those on the perimeter of the metal particles, where an acid site anchors the aromatic molecule to be further hydrogenated by hydrogen activated on platinum. The former pathway generates the high catalytic activity of the supported platinum catalysts in the hydrogenation of aromatics and is furthermore positively influenced by small electron deficient Pt clusters that can be generated via metal-support interactions using more electronegative carriers [3, 4]. In the presence of basic N-poisons the acid sites and a fraction of the metal sites are blocked, whereas the S-poison molecule first targets the metal sites inhibiting metal adsorption of other compounds.

The present work concentrates on the validation of the above described model in an industrially more relevant temperature range of 260 – 320°C and the sulfur and nitrogen tolerance of oxide supported bimetallic Pt-Pd in comparison to monometallic Pt.

Clean feed tetralin hydrogenation here leads to a continuous deactivation of the metal function and is even increased by the high WHSV. The Pt/ASA activities can be correlated with the concentration of BAS and not with the intermediate support electronegativity as reported for tetralin hydrogenation at lower temperatures [4]. CO adsorption IR results reveal that at higher temperatures and higher reactant flows the metal function is more severely blocked and therefore the reaction pathway via tetralin adsorbing on BAS in the vicinity of the Pt cluster plays a more important role. Pt/ASA (20/80) exhibiting the highest BAS concentration among the tested Pt catalysts shows in consequence the best tetralin hydrogenation performance. Moreover, Cs exchanged Pt/ASA without BAS is significantly less active than its parent Pt/ASA catalyst confirming the positive effect of BAS. Enhanced carbon metal surface coverage on more electron deficient metals in Pt/ASA induced by metal-support interactions can explain the comparably high activity of neutral Pt/SiO_2 and Pt/Al_2O_3 that do not contain BAS.

All Pt-Pd catalysts are less active compared to their monometallic counterparts due to lower reactant adsorption strength on the Pd enriched alloy surface as discussed above. Besides the support composition, also the degree of alloy formation, Pt-Pd interactions and the uniformity of the noble metal particles influence the catalytic activity. It has been presented in Chapter 2 that the present Pt-Pd clusters differ in average particle size and exhibit a wide particle size distribution. Due to these additional parameters it is not possible to correlate support properties with the catalytic Pt-Pd performances in tetralin hydrogenation, but it is interesting to note that Pt-Pd/ASA (55/45) exhibiting the smallest Pt-Pd clusters with an average diameter of 1.4 nm reveals the highest catalytic activity among all tested Pt-Pd catalysts.

The presence of the strong base quinoline in the feedstock at 260°C leads to a balanced equalization of all carriers resulting in equal Pt catalyst tetralin hydrogenation activities combined with similar *cis*- to *trans*-decalin ratios. This result is consistent with the findings at lower temperatures reported in Chapter 3, but when altering the temperature to 280-320°C the same catalyst ranking as for the clean tetralin feed experiments is observed. In this temperature range a significant fraction of denitrogenated ring opening product can be detected by GC originating from decahydroquinoline, which is produced by the hydrogenation of quinoline and subsequent second ring saturation of 1,2,3,4-tetrahydroquinoline [6]. The amount of the formed ring opening product is a measure of N-poison removal and can be directly correlated with the tetralin hydrogenation activity of all Pt catalysts. When Pt-Pd catalysts are used, not only the tetralin hydrogenation activity is significantly reduced, but also N-poison removal via hydrodenitrogenation. This results in the low quinoline tolerance of the Pt-Pd alloys in this temperature range. On the other hand it should be noted here that at lower temperatures (160 -190°C, results not shown in the present work) the N- and S-poison resistance of Pt is lower compared to Pt-Pd due to a higher adsorption/desorption equilibrium constant of tetralin and subsequently also of the catalyst poisons. The higher adsorption strength on Pt compared to Pt-Pd is indirectly proven by the much higher *cis*- to *trans*-decalin ratios.

DBT as a representative for sulfur containing heterocyclic compounds yields to stronger noble metal catalyst poisoning compared to quinoline. Nevertheless, sulfur and also nitrogen poisoning under the present reaction conditions is reversible to a large extent on both, Pt and Pt-Pd/ASA. The recovery of N- and S- poisoned catalysts is faster with Pt/ASA, probably due to a higher H_2 surface availability [24, 25]. Interestingly, the presence of quinoline leads to a slower catalyst regeneration as with only DBT, which is speculated to origin from the large amount of nitrogen induced coke formation as found by elemental analysis (see Chapter 3).

Among the oxide supported Pt catalysts the hydrogenation activity can be clearly correlated with their BAS concentration. This is consistent with the findings at lower temperatures (see Chapter 3) and shows the importance of the alternative hydrogenation pathway on BAS in the vicinity of sulfur poisoned Pt sites. This reaction model is furthermore supported by the fact that Cs exchanged Pt/ASA shows only about 50% of the parent Pt/ASA activity. These two catalysts only differ in the concentrations of BAS that are 3 and 24 μmol for Cs-Pt/ASA and Pt/ASA, respectively, but exhibit the same state of the Pt clusters as confirmed by CO adsorption IR.

It is quite surprising that Pt catalysts in the presence of 100 ppm S are still more active than the bimetallic alloy, as Pt-Pd has been frequently reported to be a very sulfur tolerant catalyst [10, 26]. In Chapter 2 we have concluded that ionic $Pt^{x\delta+}$ - $xPd^{\delta-}$ bonds are formed in Pt-Pd leading to very electron deficient Pt atoms decreasing the adsorption strength of electrophilic sulfur. Due to the Pd/Pt ratio of 3/1 the alloy surface is Pd enriched and, therefore, available very active and sulfur resistant Pt atoms are very limited on the metal cluster surface. Consequently, monometallic Pt catalysts can still outperform the Pt-Pd catalysts in the hydrogenation of tetralin with 100 ppm S as DBT in the feedstock, although the difference is becoming smaller. On the other hand, when S is adsorbed more strongly on the metal surface due to a lower reaction temperature (160 – 190°C, results not shown here), Pt-Pd shows a better S resistance resulting in a higher tetralin hydrogenation activity compared to Pt. Moreover, when S poisoning is more severe (500 ppm S), Pt-Pd/ASA does not lose further activity compared to 100 ppm S in the feed, whereas Pt/ASA reveals only about 50% of the former performance when increasing the sulfur content from 100 to 500 ppm S. This result shows the ability of Pt-

Pd to maintain significant aromatics saturation activity even under strong sulfur poisoning conditions.

In Chapter 3 it was described that the addition of only 20 ppm N as quinoline to the 100 ppm sulfur containing tetralin results in inactive oxide supported Pt catalysts due to poisoning of both, the acid and metal site function. Similarly, in the present work Pt and Pt-Pd catalysts also deactivate very fast to very low remaining activities at 260°C. When increasing the temperature to 300°C the activity of the Pt catalysts increases with time on stream, which can be explained mainly by continuous N-poison removal from BAS at higher temperatures. The same catalyst ranking as for only S-poisoned feed and the higher activity of Pt/ASA compared to Cs-Pt/ASA are the logical consequences. Free BAS close to Pt clusters can again be utilized for tetralin adsorption that is subsequently saturated by Pt dissociated hydrogen atoms.

Pt catalysts perform better than Pt-Pd in the presence of mixed S- and N-poison especially at temperatures >280°C as Pt is more active in hydrodenitrogenation resulting in more effective liberation of blocked BAS.

5 Conclusions

Tetralin hydrogen in the absence of catalyst poisons at 260 – 320°C showed that oxide supported small Pt nanocluster are more active than Pt-Pd alloy particles, due to a lower H_2 surface availability and lower aromatics adsorption strength on Pd surface enriched Pt-Pd. Carboneceous deposits on the active metal sites are the main reason for the observed continuous catalyst deactivation. Brønsted acid sites provide additional adsorption centers for tetralin, which are especially important when the active metal sites are blocked by coke formation or even more drastically by strong, but partially reversible sulfur poisoning. Neutralization of acidic supports by basic quinoline leads to an equal activity of all tested Pt catalysts at temperatures up to 260°C. Hydrodenitrogenation over Pt catalysts is responsible for the higher quinoline tolerance of the monometal compared to the Pt-Pd alloy. A lower adsorption strength of electrophilic S on very electron deficient ionic $Pt^{x\delta+}$ - $xPd^{\delta-}$ bonds leads to a good S tolerance of Pt-Pd alloys at low hydrogenation temperatures or when the S poison concentration is high (500ppm S as DBT).

Acknowledgments

Financial support of S.R.T.C. Amsterdam is gratefully acknowledged.

6 References

1. S. Albertazzi, G. Busca, E. Finocchio, R. Glockler and A. Vaccari, J. Catal., 2004. 223 372.
2. Y. Yoshimura, M. Toba, T. Matsui, M. Harada, Y. Ichihashi, K. K. Bando, H. Yasuda, H. Ishihara, Y. Morita and T. Kameoka, Appl. Catal. A-Gen., 2007. 322 152.
3. M. F. Williams, B. Fonfé, C. Sievers, A. Abraham, J. A. van Bokhoven, A. Jentys, J. A. R. van Veen and J. A. Lercher, J. Catal., 2007. 251(2) 485.
4. M. F. Williams, B. Fonfé, C. Woltz, A. Jentys, J. A. R. van Veen and J. A. Lercher, J. Catal., 2007. 251(2) 497.
5. C. A. Emeis, J. Catal., 1993. 141(2) 347.
6. C. N. Satterfield and S. H. Yang., Ind. Eng. Chem. Process Des. Dev., 1984. 23 11.
7. S. J. Ardakani, X. Liu and K. J. Smith, Appl. Catal. A-Gen., 2007. 324 9.
8. P. A. Rautanen, J. R. Aittamaa and A. O. I. Krause, Chemical Engineering Science, 2001. 56(4) 1247.
9. B. Pawelec, V. La Parola, S. Thomas and J. L. G. Fierro, Journal of Molecular Catalysis A: Chemical, 2006. 253(1-2) 30.
10. S. Jongpatiwat, Z. R. Li, D. E. Resasco, W. E. Alvarez, E. L. Sughrue, and G. W. Dodwell, Appl. Catal. A-Gen., 2004. 262(2) 241.
11. E. Rodriguez-Castellon, J. Merida-Robles, L. Diaz, P. Maireles-Torres, D. J. Jones, J. Roziere, and A. Jimenez-Lopez, Appl. Catal. A-Gen., 2004. 260(1) 9.
12. E. Guillon, J. Lynch, D. Uzio and B. Didillon, Catalysis Today, 2001. 65(2-4) 201.
13. K. Ito, Y. Kogasaka, H. Kurokawa, M. Ohshima, K. Sugiyama and H. Miura, Fuel Processing Technology, 2002. 79(1) 77.
14. A. Infantes-Molina, J. Merida-Robles, E. Rodriguez-Castellon, J. L. G. Fierro and A. Jimenez-Lopez, Appl. Catal. B-Env., 2007. 73(1-2) 180.
15. P. Biloen, F. M. Dautzenberg and W. M. H. Sachtler, J. Catal., 1977. 50(1) 77.

16. M. Boudart, D.D. Eley, H. Pines and P.B. Weisz *Catalysis by Supported Metals*, in *Advances in Catalysis*. 1969, Academic Press. p. 153.
17. Costa Augusto C.C., Zotin J.L. and Da Costa Faro A., Catal. Lett., 2001. 75 1.
18. T. Fujikawa, K. Idei, K. Ohki, H. Mizuguchi and K. Usui, Appl. Catal. A-Gen., 2001. 205(1-2) 71.
19. M. V. Rahaman and M. A. Vannice, J. Catal., 1991. 127(1) 251.
20. S. Albertazzi, R. Ganzerla, C. Gobbi, M. Lenarda, M. Mandreoli, E. Salatelli, P. Savini, L. Storaro, and A. Vaccari, Journal of Molecular Catalysis A: Chemical, 2003. 200(1-2) 261.
21. S. Dokjampa, T. Rirksomboon, S. Osuwan, S. Jongpatiwut and D. E. Resasco, Catal. Today, 2007. 123(1-4) 218.
22. A. D. Schmitz, G. Bowers and C. Song, Catal. Today, 1996. 31 45.
23. A. W. Weitkamp, Adv. Catal., 1968. 18 1.
24. G. W. Watson, R. P. K. Wells, D. J. Willock and G. J. Hutchings, J. Phys. Chem. B, 2001. 105(21) 4889.
25. G. W. Watson, R. P. K. Wells, D. J. Willock, and G. J. Hutchings, Chem. Commun., 2000 705.
26. R. M. Navarro, B. Pawelec, J. M. Trejo, R. Mariscal, and J. L. G. Fierro, J. Catal., 2000. 189(1) 184.

Chapter 5

Summary

1 Summary

The improvement of the diesel fuel quality by lowering the concentration of aromatic and sulfur compounds enhances the efficiency of modern motor and pipe exhaust gas cleaning systems and thus strongly decreases diesel exhaust emissions such as particulate matter. Ultra clean diesel fuel meeting the strict requirements of international legislations is produced by catalytic hydrotreating processes in modern refineries. For the hydrogenation of aromatics noble metal catalysts possess excellent activity, but they are unfortunately swiftly poisoned by small amounts of sulfur and nitrogen containing molecules. Supporting noble metals such as Pt on acidic carriers and the formation of a Pt-Pd alloy are frequently reported possibilities to increase the sulfur tolerance in aromatics hydrogenation. However, so far no reaction mechanism has been proposed explaining the function of Brønsted acid sites and their optimal concentration in the hydrogenation of tetralin in the presence of S-poisons. Moreover, the reaction has not been sufficiently studied in the presence of basic N-compounds that are always present in feedstocks. Finally, there is still no consistency in the literature addressing the role of the Pt-Pd alloy morphology on the aromatics hydrogenation activity and catalyst poison resistance. The purpose of the present thesis was the clarification of some of these questions.

Therefore, a series of well-defined catalysts based on platinum and bimetallic platinum-palladium nanoparticles supported on amorphous silica-alumina (ASA) with varying composition (0, 5, 20, 55 and 100% Al_2O_3) was prepared by incipient wetness impregnation. The concentration of Lewis and Brønsted acid sites (LAS and BAS) determined by pyridine adsorption was adjusted by varying the amount of aluminosilicate domains, which were quantitavely characterized by ^{27}Al (MQ) MAS NMR. A maximum BAS concentration of 42 μmol/g was achieved with ASA (20/80), whereas the LAS concentration increased with increasing Al/Si ratio. The preparation method led to small and uniform Pt (0.7 - 0.9 nm) and Pt-Pd (1.4-1.8 nm) particles on all aluminum containing supports. X-ray Absorption Spectroscopy (EXAFS) confirmed the particle

sizes determined by Transmission Electron Microscopy (TEM) and clearly showed that Pt-Pd alloys were formed. Pt in the bimetallic Pt-Pd alloy is much more electron deficient compared to monometallic Pt according to X-ray absorption near-edge structure (XANES). It is suggested from EXAFS that ionic $Pt^{x\delta+}$ - $xPd^{\delta-}$ bonds are formed leading to Pt-Pd bond shortening. CO adsorption was monitored by infrared spectroscopy (IR). From that a structural model for the Pt-Pd alloys is proposed with both Pt and mainly Pd at the surface of the nanoparticles.

The catalytic hydrogenation of tetralin over Pt/ASA catalysts was studied in the presence of nitrogen and sulfur poisons at 160 -190°C in Chapter 3. When the base quinoline was added to the feed, the catalysts activity decreased significantly to an equal level for all Pt samples, which was attributed to the neutralization of acidic supports inhibiting metal-support interactions and to competitive adsorption of tetralin and N-poison on active Pt sites. Therefore, nitrogen containing deposits on the used catalysts strongly inhibited pyridine support adsorption monitored by IR spectroscopy and Pt-N bonds were observed in the EXAFS Fourier transformations.

Strong sulfur poisoning of the Pt cluster surface by DBT led to extremely low catalyst activities that though could be enhanced by higher BAS concentrations in the carrier. The high affinity of DBT adsorption on Pt was proven by CO adsorption IR and EXAFS showing that the majority of Pt surface sites were covered by sulfur. Two types of active sites for the catalytic hydrogenation were proposed to explain the observations: (1) those on the metal particles and (2) those on the perimeter of the metal particles, where an acid site anchors the aromatic molecule to be further hydrogenated by hydrogen activated on platinum. The former pathway generates the high catalytic activity of the supported platinum catalysts in the hydrogenation of aromatics, whereas the latter alternative route becomes crucial when the noble metals sites are blocked by sulfur compounds. In consequence the addition of DBT and quinoline to the tetralin feed led to the blockage of both reaction routes resulting in inactive oxide supported Pt catalysts.

In Chapter 4 the function of Brønsted acid sites and Pt-Pd alloy formation were addressed studying the hydrogenation of tetralin in the presence and absence of sulfur as DBT and nitrogen as quinoline in the industrial relevant temperature range between 260 and 320°C.

The always observed continuous noble catalyst deactivation with tetralin feed was attributed mainly to metal site blocking by aromatic deposits as, according to CO adsorption IR, only about 5 % of the initially active Pt surface sites remained available after 44 hours time on stream at the present reaction conditions. Similarly to the findings in Chapter 3 Brønsted acid sites provided additional adsorption centers for tetralin, which are especially beneficial when the active metal sites are blocked by coke formation or even more drastically by strong, but partially reversible sulfur poisoning. This was shown by the lower hydrogenation activity of Cs exchanged Pt/ASA that does not provide BAS for tetralin adsorption in contrast to its parent Pt/ASA catalysts. Moreover, again Pt/ASA (20/80) exhibiting the highest BAS concentration was the most active catalyst in the absence and presence of sulfur. The neutralization of the acidic support by basic quinoline as shown by pyridine adsorption IR led to an equal activity of all tested Pt catalysts at temperatures lower than 260°C. The superior catalytic performance of Pt compared to the Pd surface enriched Pt-Pd alloy was due to the general better hydrogenation performance of Pt, which is the consequence of stronger tetralin adsorption on electron deficient Pt clusters. This resulted in much higher *cis*- to *trans*-decalin ratios over Pt compared to Pt-Pd, known to be a proof for stronger tetralin adsorption. The better hydrogenation performance of oxide supported Pt also led to a better quinoline tolerance compared to the Pt-Pd alloys as shown by an enhanced nitrogen poison removal by hydrodenitrogenation of decahydroquinoline especially at higher temperatures. In addition to the lower sulfur poison adsorption strength at higher temperatures, N-poison removal is the main reason for the good aromatics hydrogenation performance of noble metal catalysts at temperatures higher than 280°C in the presence of mixed S+N poison. Finally, the lower adsorption strength of electrophilic S on very electron deficient Pt formed in ionic $Pt^{x\delta+}$ - $xPd^{\delta-}$ bonds resulted in a good S tolerance of Pt-Pd alloys at low hydrogenation temperatures or when the S poison concentration is high (500ppm S as DBT).

2 Zusammenfassung

Eine Verbesserung der Dieselkraftstoffqualität durch die Reduzierung der Aromaten- und Schwefelverbindungskonzentrationen steigert die Effizienz moderner Motor- und Abgasnachbehandlungssysteme und erniedrigt folglich Dieselabgasemissionen wie zum Beispiel Feinstaub. Extrem saubere Dieselkraftstoffe, die die strengen Kriterien internationaler Gesetzgebung erfüllen, werden in katalytischen Hydrierprozessen in modernen Raffinerien produziert. In der Aromatenhydrierung weisen Edelmetallkatalysatoren eine exzellente Aktivität auf, doch werden diese leider durch kleine Mengen von Schwefel- und Stickstoffverbindungen vergiftet. Das Aufbringen von Edelmetallen wie Pt auf sauren Trägern und die Bildung von Pt-Pd Legierungen sind häufig berichtete Möglichkeiten zur Erhöhung der Schwefeltoleranz in der Hydrierung von Aromaten. Es wurde jedoch bisher kein Reaktionsmechanismus aufgestellt, der die Funktion von Brønsted sauren Zentren und ihre optimale Konzentration in der Hydrierung von Tetralin in der Anwesenheit von Schwefelgift erfasst. Auch wurde die Reaktion nicht ausreichend im Beisein von basischen Stickstoffverbindungen untersucht, obwohl sich diese immer in der Ausgangsmischung befinden. Schließlich wurde auch die Rolle der Pt-Pd Legierungsmorphologie in der Aromatenhydrierung nicht widerspruchsfrei in der Fachliteratur erklärt. Das Ziel dieser Doktorarbeit war es einigen dieser Fragen auf den Grund zu gehen.

Zunächst wurde eine Reihe von Katalysatoren auf der Basis von Platin und Platin-Palladium, geträgert auf amorphen Aluminosilikaten (ASA) mit verschiedener Zusammensetzung (0, 5, 20, 55 and 100% Al_2O_3), synthetisiert. Die Konzentration von Lewis und Brønsted sauren Zentren (LAS and BAS) wurde durch die Veränderung des Aluminosilikatanteils variiert und durch die Adsorption von Pyridin quantifiziert. Die aluminiumhaltigen Phasen wurden durch ^{27}Al (MQ) MAS NMR charakterisiert. Eine maximale BAS Konzentration von 42 µmol/g wurde in ASA (20/80) erreicht, während die LAS Konzentration mit steigendem Al/Si Verhältnis anstieg. Die Nassimprägnierung führte zu einheitlich kleinen Pt (0,7 – 0,9 nm) und Pt-Pd (1,4 – 1,8 nm) Partikeln auf allen aluminiumhaltigen Trägern. Die mittels Transmissionselektronenmikroskopie (TEM) bestimmten Pt und Pt-Pd Partikelgrößen wurden durch Röntgenabsorptionsspektroskopie (EXAFS) bestätigt und auch die Bildung einer Pt-Pd Legierungsphase konnte durch EXAFS gezeigt werden. Ein XANES „White line" Vergleich offenbarte, dass Pt Atome in der Pt-Pd Legierung elektronenärmer als in monometallischen Pt Partikeln sind. Die EXAFS Fourier-Transformationen weisen außerdem auf eine Bildung von verkürzten ionischen $Pt^{x\delta+}$ - $xPd^{\delta-}$ Bindungen hin. Die Edelmetalladsorption von CO wurde mit Infrarotspektroskopie beobachtet. Daraus konnte ein Pt-Pd Strukturmodell mit Pt, doch überwiegend Pd an der Partikeloberfläche aufgestellt werden.

In Kapitel 3 wurde die katalytische Hydrierung von Tetralin über Pt/ASA in der Gegenwart von Stickstoff- und Schwefelverbindungen bei 160-190°C untersucht. Die Zugabe von basischem Chinolin zum Eduktgemisch reduzierte die katalytische Aktivität deutlich auf ein für alle Pt Proben äqivalentes Niveau. Dies wurde einer Neutralisierung der sauren Träger, was eine Verhinderung jeglicher Metall-Träger-Wechselwirkung zur Folge hatte, und der kompetitiven Adsorption zwischen Tetralin und Chinolin zugeschrieben. Folglich konnte aufgrund stickstoffhaltiger Trägerablagerungen kaum noch Pyridin auf den verbrauchten Katalysierten adsorbiert werden. Desweiteren wurden Pt-N Bindungen in den EXAFS Fourier-Transformationen identifiziert.

Eine starke Schwefelvergiftung der Pt Clusteroberfläche durch Dibenzothiophen (DBT) führte zu sehr niedrigen Katalysatoraktivitäten, doch konnten diese mit steigenden BAS Konzentrationen im Träger erhöht werden. Die hohe Affinität von DBT auf Pt zu adsorbieren konnte mit CO Adsorption IR und EXAFS bewiesen werden, da diese Charakterisierungstechniken zeigten, dass die große Mehrheit der Pt Oberflächenzentren durch Schwefel bedeckt wurden. Zwei verschiedene Arten von aktiven Zentren für die katalytische Hydrierung, die die erhaltenen Ergebnisse beschreiben können, wurden identifiziert: (1) Metallpartikeloberflächenatome und (2) Brønsted saure Zentren im unmittelbaren Umkreis der Pt Cluster, wo Tetralin adsorbieren kann und in der Folge durch am Metallpartikel aktivierten Wasserstoff hydriert wird. Der erste Reaktionsweg ist verantwortlich für die hohe Aktivität der geträgerten Platinkatalysatoren in der Aromatenhydrierung, wohingegen die zweite Route entscheidend wird wenn die Edelmetallzentren, besonders durch Schwefel, geblockt werden. Folglich führte die

Zugabe von DBT und Chinolin zum Ausgangsgemisch zu einer Blockierung beider Reaktionswege und somit zu inaktiven oxidgeträgerten Pt Katalysatoren.

In Kapitel 4 wurde die Rolle der Brønsted sauren Zentren und der Pt-Pd Legierungsbildung hinsichtlich ihrer Bedeutung in der Hydrierung von Tetralin in Beisein und Abwesenheit von DBT und Chinolin im industriell relevanten Temperaturbereich zwischen 260 und 320°C untersucht. Die stets beobachtete kontinuierliche Katalysatordeaktivierung während der Hydrierung von Tetralin wurde hauptsächlich der Blockierung von Metallzentren durch aromatische Ablagerungen zugeschrieben, da die CO IR Spektroskopie zeigte, dass nur ca. 5% der ursprünglich verfügbaren Pt Oberflächenzentren nach 44 Stunden Reaktionszeit zugänglich blieben. Ähnlich zu den Erkenntnissen in Kapitel 3 dienten Brønsted saure Zentren als zusätzliche Adsorptionszentren für Tetralin. Diese sind besonders nutzbringend wenn die aktiven Metallzentren durch Kohlenstoffablagerungen oder durch starke Schwefelvergiftung blockiert sind. Das wurde durch die niedrigere Hydrieraktivität von Cs getauschtem Pt/ASA, welcher kaum noch BAS zur Tetralinadsorption im Vergleich zum Ausgangs-Pt/ASA Katalysator bereitstellt, gezeigt. Außerdem war wiederum Pt/ASA (20/80), der Katalysator mit der höchsten BAS Konzentration, der aktivste Katalysator sowohl in der Abwesenheit als auch im Beisein von Schwefel. Die Neutralisierung der sauren Zentren durch basisches Chinolin wurde durch Pyridinadsorption bestätigt und führte zu einer äquivalenten Aktivität aller getesteten Pt Katalysatoren bei Temperaturen bis zu 260°C. Die bessere katalytische Leistung von Pt im Vergleich zu den mit Pd oberflächenangereichertem Pt-Pd Legierungen läßt sich mit der allgemein besseren Hydrierfähigkeit von Platin erklären. Dies ist die Folge einer stärkeren Tetralinadsorption auf Pt verglichen zu Pt-Pd, was sich sich in viel höheren *Cis*- zu *Trans*-Dekalin Verhältnissen im Reaktionsprodukt niederschlug. Die bessere Hydrierfähigkeit von oxidgeträgertem Pt schlug sich auch in einer besseren Chinolintoleranz nieder, was die Folge von Stickstoffgiftentfernung durch Dehydronitrogenierung besonders bei höheren Temperaturen war. Diese Reaktion trat in weitaus geringerem Maße über den getesteten Pt-Pd Katalysatoren auf. Außer einer Abnahme der Schwefeladsorptionsstärke bei höheren Temperaturen, ist die Stickstoffgiftentfernung der Hauptgrund für die gute

Aromatenhydrieraktivität aller Edelmetallkatalysatoren bei Temperaturen größer als 280°C in der Präsenz von gemischtem S+N Verbindungen. Schließlich führte die niedrigere Adsorptionsstärke von elektrophilem Schwefel auf sehr elektronarmen Platin in ionischen $Pt^{x\delta+}$ - $xPd^{\delta-}$ Bindungen zu einer guten Schwefeltoleranz der Pt-Pd Legierungen besonders bei niedrigen Temperaturen und bei einer erhöhten Schwefelkonzentration im Eduktgemisch (500 ppm S als DBT).